CRACKLE NOISE FROM HIGH-SPEED FREE-SHEAR-FLOW TURBULENCE

BY

DAVID ALEXANDER BUCHTA

DISSERTATION

Submitted in partial fulfillment of the requirements
for the degree of Doctor of Philosophy in Theoretical and Applied Mechanics
in the Graduate College of the
University of Illinois at Urbana–Champaign, 2016

Urbana, Illinois

Doctoral Committee:

Professor Jonathan B. Freund, Chair, Director of Research
Associate Professor Carlos A. Pantano-Rubino
Associate Professor Daniel J. Bodony
Professor Sascha Hilgenfeldt

Abstract

The sound from high-speed jets, such as on military aircraft, is distinctly different than that from lower-speed jets, such as on commercial airliners. Atop the already loud noise, a higher speed adds an intense, fricative, and intermittent character. The corresponding pressure fluctuations also have a peculiar shape with strong, steep compressions and weaker, rounded expansions, which is thought to be responsible, at least in some part, for their distinct perception. A complete explanation of this distinct and important aspect of jet noise is lacking, and in particular, the root turbulence mechanisms that give rise to the skewed acoustic signal are unknown.

Direct numerical simulations (DNS) of high-speed free-shear-flow turbulence are used to assess the underlying mechanisms and quantify near-field nonlinearity as potential sources of the radiated wave field, especially the pressure skewness. Though the DNS is restricted to a modest Reynolds-number range, the simulated turbulence is shown to have a broad range of scales and reproduce the energy spectra of realistic turbulence. This configuration is presented as a near-nozzle 'piece' of a relatively high-Reynolds-number jet. At high speeds, with Mach number $M \gtrsim 2.5$, the simulated near-field pressure signals reproduce the distinct crackle-like features observed with relatively flat shock-like waves, with sharp, steep compressions followed by weaker, rounded expansions. Their corresponding pressure skewness for $M \gtrsim 2.5$ exceeds the level $S_k(p') \gtrsim 0.4$ associated with perception of jet crackle.

Detailed assessments of the factors leading to $S_k(p')$ show that the skewed pressure waves occur immediately adjacent to the turbulence source, at the edge of the rotational region. Also, direct observation of the near-acoustic field indicates that the pressure waves have complex three-dimensional structures and nonlinearly merge as they propagate. Where these waves intersect above the mixing layers, the pressure compressions are stronger than their corresponding expansions. We investigate the near-field wave development and provide a complete statistical assessment of the factors transporting the pressure skewness. For $M \gtrsim 2.5$, nonlinear interactions above the mixing layers, which add to S_k, are balanced by damping molecular effects, which subtract from it. Thus, the 'footprint' of crackle with $S_k \gtrsim 0.4$ is generated essentially at the turbulence source.

Invoking the stability characteristics of high-speed free-shear flows, which are known to change character at high speed, we assess the sensitivity of skewness to changes in the turbulent structure, which we adjust using a novel forcing approach. Pressure skewness is shown insensitive to the three-dimensional structure and to the strength of the structures in its source. Using a larger, higher-Reynolds-number simulation, we likewise show that S_k is Reynolds number insensitive.

Finally, we develop a reduced gas dynamics description that neglects the turbulence dynamics *per se* and present a description of a mechanism that leads to $S_k(p') > 0.4$. The model flows reproduce the essential skewness characteristics observed in the DNS. At its core, this mechanism shows simply that nonlinear compressive effects lead directly to stronger compressions than expansions and thus $S_k(p') > 0$.

Acknowledgments

Foremost, this research would not be possible without my advisor, Professor Freund. His valuable guidance has led me to consider problems in new and different ways with consistent advice to always be thinking about 'What's next?' and 'What's important?'. The time spent working with Prof. Freund has been a true privilege and rewarding experience.

Many thanks are also due to my defense committee: Professors Daniel J. Bodony, Carlos Pantano-Rubino, Sascha Hilgenfeldt, and Taraneh Sayadi for providing their valuable time and careful, critical review of this work.

I would also like to acknowledge the Air Force of Scientific Research for research funding and the computational resources provided by the Department of Defense High Performance Computing Modernization Program. A portion of the simulations were also performed with a Blue Waters Exploratory Award at the University of Illinois in Urbana–Champaign.

The lab members, past and present, of Prof. Freund's group have provided invaluable interactions and extensive discussions which brought new ideas and helped me troubleshoot research-related issues: Drs. Ramanathan Vishnampet, Joel Krehbiel, and Jesse Capecelatro as well as Natalie Beams, Spencer Bryngelson, Esteban Cisneros Garibay, Seung Whan Chung, and Jonathan Wang.

The unwavering support and love from my wife, Casey, focused me profoundly throughout this work. She is the most amazing partner in life, sacrificing so much more, so that I could attend to this research. Last, our dachshund, Layne, gave me a grounded perspective on life and relaxing downtime during the inevitably stressful periods of this work.

Dedicated to my family.

Table of Contents

List of Tables

List of Figures

Chapter 1

Introduction

1.1 Background

Military jets and other aircraft operating with high-specific thrust engines have been observed to radiate a particularly intense and distinct sound that has become known as 'crackle'. Crackle has been described as a 'startling staccato of cracks and bangs' (Ffowcs Williams *et al.*, 1975) and, although a very annoying aspect of jet noise, this distinct sound can cause aural injury for personnel working in close proximity. Reducing or eliminating crackle from the overall jet noise would reduce annoyance, improve environmental noise levels near airbases, and decrease the potential for injury.

Crackle was first reported as a distinct phenomenon by Ffowcs Williams *et al.* (1975) for supersonic full-scale engines and lab-scale jets. Although crackle is extremely intense, it has been proposed that it is the intermittency of crackle that makes it particularly annoying (Ffowcs Williams *et al.*, 1975). For the full-scale Olympus 593 jet engine, with diameter $D_j = 3.9$ ft and exit velocities $V_j > 1145$ ft/s, crackle was observed to last between 0.1 and 1 seconds over 1 to 2 second intervals at seemingly random times (Ffowcs Williams *et al.*, 1975). During this period, strong shock-wave-like compressions are observed at a typical period of $\approx 10^{-2}$ seconds. The time trace of acoustic pressure during a crackle event reveals a peculiar feature: strong, steepened compressions (lasting 1 millisecond) followed by longer weaker expansions (lasting 2 to 3 milliseconds) with the rarefaction amplitude approximately $\frac{1}{4}$ the preceding compression peak. A typical skewed pressure trace is shown from a lab-scale jet in figure 1.1 (a).

Ffowcs Williams *et al.* (1975) invoked the statistical skewness of acoustic pressure to quantify the distribution of the amplitude asymmetry between the sharp, intense pressure peaks and the relatively rounded, weaker low-pressure valleys in the sound signal. It was determined that sound with

$$S_k(p') \equiv \frac{\overline{(p')^3}}{\overline{(p')^2}^{3/2}} \gtrsim 0.4, \tag{1.1}$$

would be perceived by a typical listener as crackling. Though not a rigorous definition, statistical skewness

does provide a convenient metric to the likely perception of crackle (Ffowcs Williams *et al.*, 1975; Krothapalli *et al.*, 2000; Petitjean & McLaughlin, 2003; Petitjean *et al.*, 2005), though this is the subject of ongoing consideration since skewness does not *directly* quantify perception. It also obviously does not represent other qualitative features of crackling pressure signals, most notably the abrupt compression and slower expansions of p' (McInerny, 1996; Gee *et al.*, 2007; Baars & Tinney, 2014; Gee *et al.*, 2016). Gee *et al.* (2007) suggests that the skewness of the time derivative of pressure might therefore be a better metric for quantifying sharp changes in the pressure signal, which are also observed to correspond with jet noise with $S_k(p') \gtrsim 0.4$. Regardless of whether or not $S_k(p')$ *per se* is the *best* indicator for the perception of crackle, it is a peculiar and relatively poorly explained aspect of this kind of jet noise.

1.2 Key motivating observations

Pressure skewness is observed to depend on jet operating conditions. $S_k(p')$ is known to increase with increasing flow velocity (Ffowcs Williams *et al.*, 1975; Szewczyk, 1978; Krothapalli *et al.*, 2000; Petitjean & McLaughlin, 2003; Petitjean *et al.*, 2005; Gee *et al.*, 2013*a*), and crackle is apparent when the jet velocity is high enough that turbulent eddies in the shear layer move supersonically relative to the ambient free stream (Krothapalli *et al.*, 2003*a*). Though initial studies suggested that crackle was insensitive to jet temperature (Ffowcs Williams *et al.*, 1975; Szewczyk, 1978), based upon the temperature range tested, S_k increases with higher jet temperature conditions (Krothapalli *et al.*, 2000; Petitjean & McLaughlin, 2003; Mora *et al.*, 2012). These trends are also seen in rectangular nozzles jets (Heeb *et al.*, 2013). Crackle does not appear to be correlated with the presence of shock-cells from imperfect expansion (Ffowcs Williams *et al.*, 1975; Szewczyk, 1978; Krothapalli *et al.*, 2000) nor to combustion processes in full-scale engine tests (Ffowcs Williams *et al.*, 1975).

High skewness are measured at angles near the expected Mach angle for these flow conditions (Ffowcs Williams *et al.*, 1975; Laufer *et al.*, 1976; Szewczyk, 1978; Krothapalli *et al.*, 2000; Petitjean & McLaughlin, 2003; Petitjean *et al.*, 2005; Gee *et al.*, 2013*a*; Baars *et al.*, 2014; Nichols *et al.*, 2013; De Cacqueray & Bogey, 2014) suggesting a link between crackle and the Mach-wave-radiation mechanism known to occur in supersonic free-shear-flow turbulence. Krothapalli *et al.* (2000) confirmed that strong, sharp pressure compressions associated with crackle correlated to the location of intense shock-wave-like waves seen in schlieren images near the turbulence shown in figure 1.1 (b). For a $M = 2$ ideally expanded jet, as the temperature was increased, the number of the strong waves near the jet also increased (Krothapalli *et al.*, 2000). Schlieren images indicated that lower temperature jets had less intense Mach waves and corresponding pressure signals that

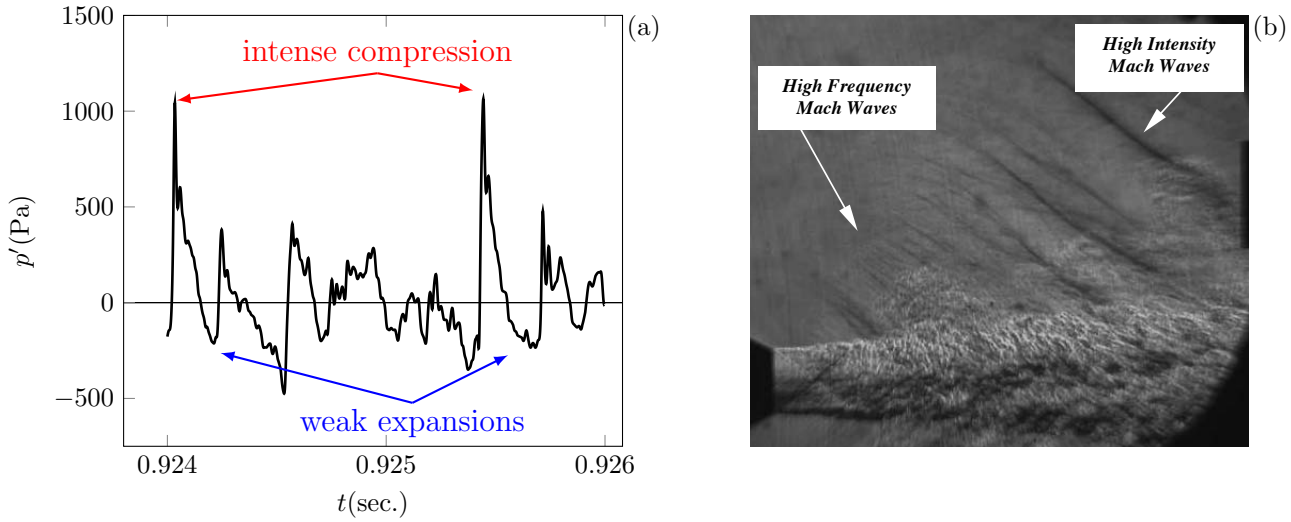

Figure 1.1: (a) Typical skewed pressure trace reproduced from figure 7 in Krothapalli *et al.* (2003*a*). (b) Schlieren of $M = 2$ heated jet (Krothapalli *et al.*, 2002).

lacked the high skewness. It was only for jet temperatures (T_j) larger than the ambient temperature (T_∞), $T_j/T_\infty = 1.23$, for $M \gtrsim 2.0$ that the Mach-wave radiation also had the peculiar, skewed pressure statistics (Krothapalli *et al.*, 2003*a*). Steepened, directional Mach waves were also observed in the DNS simulation of a $M = 1.92$ round jet (Freund *et al.*, 2000*b*) and more recent simulations of jets and other free shear flows (Nichols *et al.*, 2013; Anderson & Freund, 2012; Buchta *et al.*, 2014; De Cacqueray & Bogey, 2014), confirming the appearance of apparently nonlinearly steepened Mach-waves near the turbulence suggesting a S_k source.

Pressure spectra appears to be insensitive to noise signatures containing crackle (Ffowcs Williams *et al.*, 1975), in part, because of its intermittency: crackle events (shock-like features with asymmetrical high and low pressure peaks) occur in only about 5% of the acoustic signal (Laufer *et al.*, 1976; Krothapalli *et al.*, 2000).

1.2.1 Crackle and sound suppression

Control strategies that reduce peak noise in supersonic jets also reduce skewness, suggesting a link. It has been supposed that both sound levels and skewness are reduced for the same reasons: formation of large-scale structures is inhibited, the convection speed of eddies is reduced, the turbulence levels are diminished, or some mix of these effects. Despite this *sense* of the underlying mechanisms, it is unknown why S_k is reduced. Ffowcs Williams *et al.* (1975) observed that skewness is reduced by silencers and notched nozzle geometries, which are thought to reduce the coherence of the large-scale eddies. Adding a co-flow to the

primary jet, which is expected to reduce the relative convection speed of eddies, reduces noise along the primary radiation direction and also pressure skewness (Papamoschou & Debiasi, 2001; Papamoschou *et al.*, 2014, 2016). Microjets positioned to interact with the near-nozzle shear layer decrease skewness in the near field (Krothapalli *et al.*, 2003*b*, 2005). Air and aqueous micro-jets are shown to reduce turbulent intensities and Reynolds stresses within the shear layer. Chevrons that penetrate the near-nozzle shear layer reduce noise and skewness levels along the nominal Mach-wave direction (Martens *et al.*, 2011; Mora *et al.*, 2013*a*). Schlieren imaging showed a faster jet spreading rate due to chevrons, and particle image velocimetry (PIV) also confirmed that chevrons reduced the turbulent kinetic levels, which correlated to a reduction of sound levels and skewness (Mora *et al.*, 2015). Other nozzle geometries designed to reduce peak noise levels have been observed to impact the near-field Mach-wave angles with the expectation that the relative source speed of large-scale structures is reduced (Murray & Lyons, 2016). However, no pressure measurements were made making it impossible to connect wave kinematics and crackle phenomenology. Despite the relative success of these control strategies to reduce skewness along with noise levels, a specific understanding of $S_k(p')$ is lacking. Still, these reductions point to a mechanism or a combination of mechanisms that appear to be linked to the presence of skewed radiated pressure waves.

1.3 Questions regarding crackle

It appears that crackle is correlated to signals with intermittent periods of steepened shock-like waves followed by weaker, longer, rounded rarefaction regions, though it remains unclear as to whether crackle originates at the turbulent source, arises from nonlinear propagation effects, or is a mixture of both. Ffowcs Williams *et al.* (1975) suggested that crackle originates at or near the source by demonstrating that crackle was independent of jet scale and propagation distance. This result suggests that cumulative nonlinear propagation effects do not effect the skewness.

Contrary to these observations, $S_k(p')$ has been shown to increase with propagation distance (Szewczyk, 1978; Petitjean & McLaughlin, 2003; Petitjean *et al.*, 2005), though the mechanism is unclear. For an initially non-skewed signal, Szewczyk (1978) found S_k to rise to $S_k \gtrsim 0.8$ between $5\,D_j$ and $60\,D_j$ from the jet turbulence. Petitjean & McLaughlin (2003) observed a more modest increase of S_k. Their measurements were acquired much farther initially at $r = 50D_j$ from the source, which suggests that the more intense perturbations near the jet undergo stronger nonlinear propagation effects than the weaker waves at a larger distance.

There is the expectation that waves will steepen which contribute energy to high frequencies (Lighthill,

1956) and the possibility that wave merging due to nonlinearity will increase low-frequency energy content (Crighton, 1986; Lighthill, 1993). In heated jets, Petitjean & McLaughlin (2003) noticed a shift in the spectral peak from $St_{D_j} = 0.15$ to 0.05 between $r/D_j = 15$ to 100 which suggests wave merging. Also, the slope in the high-frequency range between $St_{D_j} = 0.15$ to 2 shallows with distance suggesting the waveforms are also steepening, increasing the energy in the high-frequency components, though these nonlinearities have not been firmly connected with S_k.

Recent high-resolution space-time pressure data near jets suggests that distinct waves do merge (Fiévet *et al.*, 2015) though again the connection to crackle and its S_k is unclear. These authors remarked that wave merging of this kind can 'artificially escalate' nonlinear metrics like the skewness of pressure time derivative and also 'mislead one into believing that cumulative nonlinear distortions are occurring along the propagation path' (Fiévet *et al.*, 2015). Whether or not this effect is considered as a cumulative propagation effect *per se*, observations of wave merging confirm nonlinear acoustics. The DNS reported here also show that waves merge and statistical assessments confirm that the average number of distinct waves decreases beyond the turbulence (Buchta *et al.*, 2014). Details of these wave statistics are provided in chapter 4.

Over the propagation distances on the lab-scale, nonlinear acoustics appear to affect skewness, but they do not explain its root cause; also, it is not clear these effects are important for sustaining S_k beyond the turbulence. Visualizations of steepened waves near the jet shear layer support the possibility of a near-source effect (Krothapalli *et al.*, 2000; Freund *et al.*, 2000*b*; Darke & Freund, 2001; Nichols *et al.*, 2013), but the connection between a steepened wavefront essentially seen at the source to the skewed near-field signal is unknown leaving nonlinear acoustic effects a potentially important effect.

In the perspective of the current DNS, figure 1.2 shows a typical crackle signal taken above a mixing layer showing the possible mechanisms that were discussed in its generation. In summary, the underlying mechanism of the peculiar 'footprint' of crackle with $S_k(p') \gtrsim 0.4$ is unknown and the following questions remain:

- Is crackle best viewed as a source effect or propagation effect (or both)? That is, does crackle originate right at the turbulence source?
  - Is crackle tied to the generation of the apparently steepened Mach-like waves?
  - Do nonlinear interactions in the irrotational near field affect crackle?

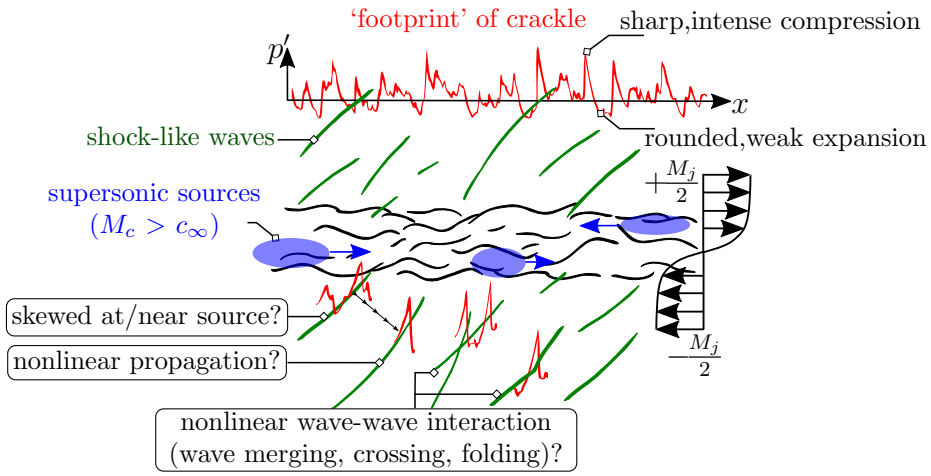

Figure 1.2: Schematic of Mach-like wave radiation from supersonic, free-shear flow turbulence with possible skewness mechanisms circled.

1.4 Flow features of high-speed jet noise

Early evidence shows that the near-field of high-speed turbulent jets is distinct in character from that at low speeds (Laufer, 1961; Eggers, 1966; Lowson & Ollerhead, 1968; Westley & Woolley, 1968; Dosanjh & Yu, 1968; Salant *et al.*, 1971). It can be anticipated that the character of acoustic radiation should indeed change when the flow is sufficiently fast that the turbulence structures advect at supersonic speeds, which provides them a wavenumber-frequency make-up that directly couples to propagating solutions of a scalar wave equation, with the implication that they might then constitute particularly efficient acoustic sources (Ffowcs Williams, 1963; Crighton, 1975). In contrast, at lower speeds, it is the more subtle changes to the dominant eddies that couple with propagating waves (Lighthill, 1952; Crighton, 1975). Phillips (1960) recognized the potential importance of this, suggesting the generation of 'eddy Mach waves' because the wave front angles are near the Mach angle that would be anticipated for supersonically advecting turbulence structures. In the framework of Lighthill's acoustic analogy, Ffowcs Williams & Maidanik (1965) considered the Mach-like-wave field radiating from high-speed sheared flows and predicted within about 3 dB the noise levels from boundary layer experiments of Laufer (1961). Though the basic mechanism of Mach-wave radiation is relatively well-understood, the explanation of steepened and notably skewed waves of crackling jets remains unclear. The source of its S_k in particular is unclear

1.4.1 Kinematics of Mach-like waves

For a source speed (U_s) exceeding the sound speed (c_∞), the corresponding potential flow wave angle is

$$\theta = \sin^{-1}\left(\frac{c_\infty}{U_s}\right), \tag{1.2}$$

which is the direction that infinitesimal disturbances propagate along Mach lines. Figure 1.3 shows the potential link between the wave orientation above turbulence and its corresponding source speed using (1.2). This relation has been used extensively to correlate the observed wave angles to the expected source speeds in high-speed shear flows. Oertel (1979) found angles corresponding to three seemingly distinct wave speeds. Tam & Hu (1989) linked these to three families of instability modes supported by high-speed free-shear flows. Similar instabilities are also supported by parallel temporally-developing shear layers (Sandham & Reynolds, 1990, 1991).

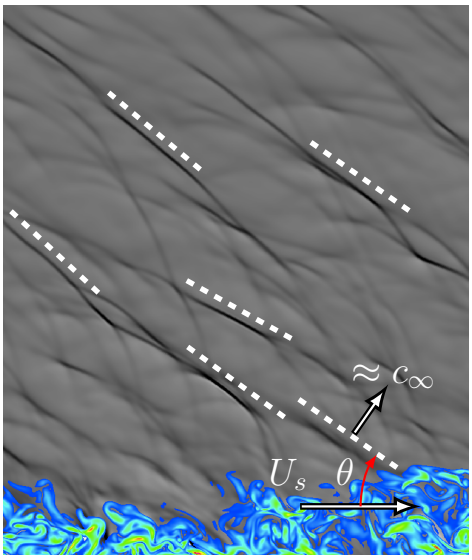

Figure 1.3: Wave angle of the compressive fronts radiated by high-speed free-shear-flow turbulence.

Though linear stability can predict the convective speed of large-scale instability modes, turbulent flows exhibit a broad range of length and time scales. In their experiments, Murray & Lyons (2016) quantified the distribution of wave orientations radiated from jet turbulence and inferred the corresponding distribution of source speeds with (1.2). Similarly, DNS of shear layers exhibited a distribution of wave orientations from strong compression waves near the turbulence (Buchta *et al.*, 2014). The distribution of wave angles (and wave velocities) in figure 1.3 can lead to nonlinear interactions as these waves propagate along their course. Waves can merge, reducing the number of distinct waves, and also cross with other waves (see figure 1.4) generating local peaked pressures.

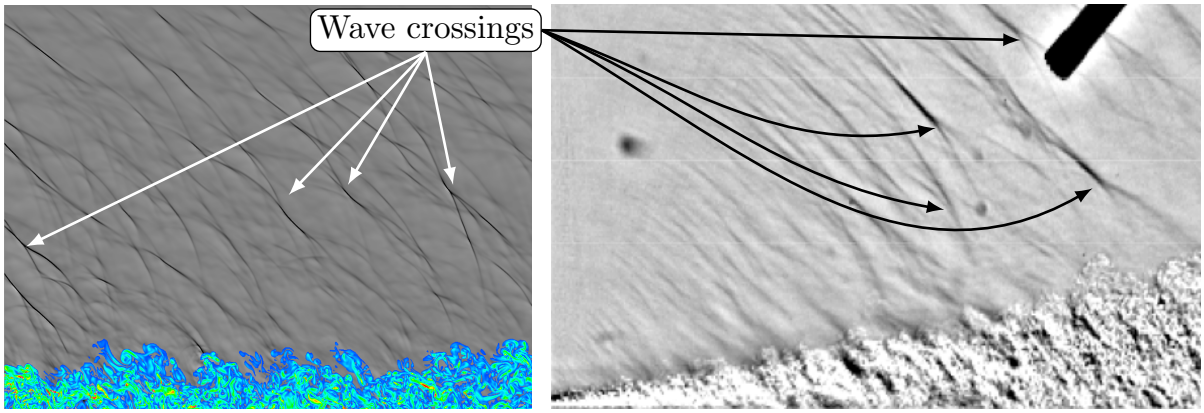

.

Figure 1.4: (a) Simulated turbulence and near-field shock-like waves. (b) Visualization of the near-field wave features from $M = 1.5$ jet from Papamoschou (2000)

1.4.2 Propagation of disturbances

The radiated pressure waves are anticipated to steepen and form shocks, but so weak of shocks that Newtonian fluid viscosity is anticipated to describe their structure quantitatively (Lighthill, 1956). Nonlinearity, which will be relatively weak in this case, will still facilitate wave–wave interactions, models for which propagation (including fitting of weak shocks) are summarized by Whitham (1974). For the one-dimensional propagation of broadband sound, weak-shock theory predicts a spatial waveform of N-waves (Pestorius & Blackstock, 1974; Lighthill, 1993). For any frequency component, the corresponding compressive portions of the wave steepens, whereas the expansive part shallows. The steep parts, or shocks as they occur, merge. The long-distance behavior is a series of N-waves, which continues to evolve with strong shocks catching up to weaker shocks. However, there is a notable difference with the observations of crackle waves, which we need to highlight here: there is no expectation that such a mechanism will lead to a skewed signal. Instead, $S_k = 0$ suggests that pressure skewness arises from some other factor than one-dimensional, weak-shock propagation. Crighton (1986) has showed the possibility that linear dispersion and attenuation coupled with nonlinear mechanisms in the course of one-dimensional propagation increases S_k with distance.

1.4.3 Wavepacket modeling

Wavepackets, motivated by the growing-decaying character of instability waves, have been suggested to provide a plausible representation of turbulence noise sources (Mollo–Christensen, 1967; Crighton & Huerre, 1990; Jordan & Colonius, 2013). The sound from wave packets that convect supersonically in a weakly nonlinear, stationary flow reproduce similar Mach-wave-like radiation along with spatial skewness distribu-

tions similar to those observed in jet crackle (Avital *et al.*, 2013). For any of the wavepacket structures (i.e. Gaussian or algebraic), like those described in Crighton & Huerre (1990) and Avital & Sandham (1997), high skewness, exceeding $S_k > 0.4$, was found predominately along the Mach wave direction(Avital *et al.*, 2013). Including the weak nonlinearity yields crackle-like features (Avital *et al.*, 2013), but it still remains unclear whether or not crackle is best described as a source effect or propagation effect.

1.4.4 Linear stability analysis

Linear instabilities are well understood to provide a model for free-shear-flow turbulence structures(Lessen *et al.*, 1965; Tam & Burton, 1984*a*,*b*; Jackson & Grosch, 1989; Sandham & Reynolds, 1990). However, this description is fundamentally limited in regard to predicting the hallmark features of high-speed-jet noise: shocks with skewed pressure signals. Wu (2005) has expanded the theory of Tam & Burton (1984*a*,*b*) to include weakly nonlinear effects associated with the growth and decay of these instabilities. The initial pressure wave at the source includes the nonlinear growth of the modes and their near-field average sound intensity agrees well with those measured by Troutt & Mclaughlin (1982). The analysis of Wu (2005) has not yet been applied to estimating near-field pressure skewness, and it is also unclear if the pressure waves from these mode dynamics are linked to turbulence.

1.5 Overview of dissertation

1.5.1 Approach and basic justification

Much of the analysis presented is grounded in direct numerical simulations, which are designed to provide an accurate and detailed description of the turbulence mechanisms and near acoustic field, including any near-field nonlinearity that leads to pressure fluctuations of the kind associated with the perception of crackle. The simulations resolve all the energetic scales with no modeling approximations, which would potentially affect important features of the flow field, such as the sharp shock-like compressions in the near acoustic field. Their resolution is thoroughly assessed in sections 3.2 and 3.3. Though the shock thickness is set by the viscosity for the parameters considered, there is a small, but finite numerical dissipation in the simulations, which is expected to modestly thicken shocks. In chapter 4 we show that S_k is insensitive to this dissipation. Based on the length, δ_{99}, where the velocity is $0.99(\Delta U/2)$, the majority of the simulations we report have a relatively high Reynolds number

$$Re_{\delta_{99}} = \frac{\rho_\infty \delta_{99} \Delta U}{\mu_\infty} = 9200, \tag{1.3}$$

with ρ_∞ the density, ΔU the shear layer velocity difference and μ_∞ the viscosity. Thus, we simulate a relatively broad range of turbulence scales. Still, they are limited by the well-known resolution challenges of any DNS, so we report an extra-large simulation at $Re_{\delta_{99}} = 18500$ to confirm insensitivity.

While jet noise is the most engineering relevant configuration, we chose to study a temporally-developing planar shear layer because it provides a clearer perspective of the root mechanisms of this sound generation. Though the equations are frame invariant, it is important to recognize at the outset the similarities and differences between the present temporally developing flow and a corresponding spatially developing flow, such as the near-nozzle shear layer of a jet. We switch from the supersonic advection generating Mach-like waves in a frame attached to a nozzle to the corresponding phenomenon in a time-developing flow, where transient approximately stationary (on average) turbulence features are adjacent to a supersonic stream. This configuration can be considered a model for the near-nozzle region of a high-Reynolds-number jet (see figure 1.5), where the turbulence is concentrated in a weakly curved (for a typical round jet) shear layer between the high-speed potential core flow and the surrounding co-flow. Because the simulations focus on this small region, it does allow us to explicitly resolve a broader range of local turbulence scales than could be represented in a full jet simulation. In essence, it provides a Reynolds-number realistic representation of a small near-nozzle 'piece' of a jet, and it therefore allows us to probe the sound generation mechanisms of high-Reynolds-number turbulence. Lab-scale measurements of the near-nozzle shear layer show that the momentum thickness is $\delta_m^o \sim 10^{-3} D_j$, suggesting that a low-$Re_{\delta_m^o}$ DNS with $Re_{\delta_m^o} \sim 10^2$ to 10^3 would

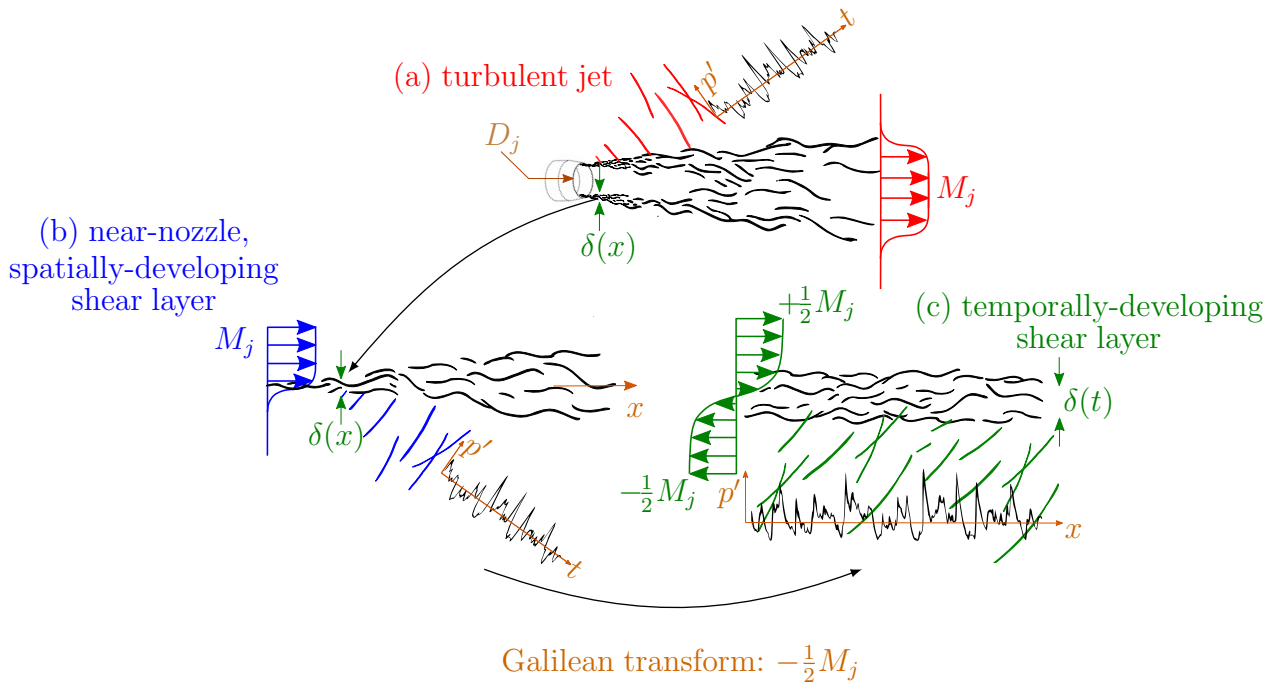

Figure 1.5: Relation of the present temporally-developing flow to the round jet and its near-nozzle (approximately planar) spatially developing shear layer.

represent a piece of a moderately high $Re_{D_j} \sim 10^5$ to 10^6 flow by

$$Re_{D_j} \equiv \frac{\rho_\infty U_j D_j}{\mu} = Re_{\delta_m^o} \times \frac{D_j}{\delta_m^o}. \tag{1.4}$$

It can be anticipated the acoustic far-field will not include the geometric propagation effect associated with a round jet, though this will not be a large effect for studying the very near field.

An unfortunate disadvantage of this flow configuration is that it is not well-suited for making point-to-point comparisons with lab measurements because there is no direct experimental counterpart to temporally developing shear layers. Considering that the computational domain sizes of DNS are typically $L \sim 10^2\,\delta_m^o$ to $10^3\,\delta_m^o$ then the simulated near field is up to a jet diameter D_j or slightly less relative to the full-scale jet. We do expect that lab measurements would 'see' a steepened, skewed footprint of a weakly nonlinear signal. The nearly linear signal would continue to propagate with its peculiar, asymmetric character and undergo slow, cumulative nonlinear changes associated with propagation of this type. Near-field acoustic measurements support this (Petitjean & McLaughlin, 2003; Petitjean *et al.*, 2005; Baars & Tinney, 2014; Fiévet *et al.*, 2015), and at a minimum, semi-quantitative comparison to experimental observation can be made, keeping in mind the points of difference. The details of the simulation configurations and numerical methods are provided in chapter 2, and we confirm that the turbulence develops to be broadbanded and

show that the statistics reproduce experimental observation in chapter 3.

We shall see in chapter 4 that near the turbulence, the pressure fluctuations do exhibit the hallmarks of crackle: $S_k(p') > 0.4$, with steep compressions in the sound field. Analysis of our database will show the key features of the near-field acoustics that lead to these characteristics. We report turbulence statistics, and the evolution of the Mach-like wavefield leading to the pressure disturbances correlated to crackle. Though DNS is restricted to modest Reynolds number due to finite computational resources, we simulate a $2 \times Re_{\delta_m^\circ}$ Reynolds number of the nominally crackling $M = 2.5$ configuration in chapter 4. This higher-Reynolds-number case confirms S_k-insensitivity to Reynolds number. In chapter 5, we compute terms governing pressure skewness transport and find that high-order nonlinear interactions are countered by molecular effects in the near-field leading to an approximately constant S_k with distance from the mixing layer.

Chapter 6 examines these hallmarks of crackle from a gas dynamics mechanism, with the turbulence providing a generic velocity-field forcing. This starts with a review of some basic mechanisms of weakly nonlinear gas dynamics. It then considers a wavy-wall model flow. The trends of skewness with Mach number compare well with observations from free-shear-flow turbulence. We find that skewness is insensitive to the details, in particular the small-scale structures and the correlation lengths associated with the input velocities.

In chapter 7, we assess the sensitivity of S_k to the source structure from a different perspective: we modulate the turbulence in the DNS with weak inhomogeneous source terms that target the three-dimensional modes whose appearance at increasing M corresponds to the appearance of crackle features. The goal is to assess whether or not it is the particular three-dimensional structure of the turbulence at higher Mach numbers that is responsible for the observed crackle sound patterns. Thus, the forcing modifies the high-M, more three-dimensional turbulence to share the relatively two-dimensional low-M structure. The source removes energy from the three-dimensional modes, in question, excites the two-dimensional modes. An obvious change in the turbulence and near-field sound, making it more two-dimensional with spanwise correlation, is observed. However, the S_k is relatively unchanged, which is consistent with the robustness of S_k to the source changes in chapter 6. We end the dissertation in chapter 8 with a summary of conclusions and discussion of future work.

1.5.2 Summary of findings

The key findings of this dissertation are

- DNS of subsonic to supersonic free-shear-flow turbulence for $0.9 \leq M \leq 3.5$ confirms that $S_k(p') \gtrsim 0.4$ for $M \geq 2.5$ (chapter 4).
- Pressure fluctuations are skewed, with $S_k(p') \gtrsim 0.4$, very near the turbulence at $y/\delta_m(t) \approx \delta_{99}$ (chapter 4).
- The sound propagates with approximately constant S_k between $y \approx \delta_{99}$ and the domain boundary (chapter 4); budgets of S_k indicate a balance of strengthening nonlinear interactions and damping molecular effects (chapter 5).
- Direct observation of wave-merging phenomenon with detailed wave statistics quantifies near-field nonlinearity, particularly the reduction of distinct waves with distance (chapter 4).
- S_k is insensitive to Reynolds number for those simulated (chapter 4), supporting that its generation is shared by the large-scale dynamics in the turbulence, and confirming insensitivity of the propagating waves to viscous effects.
- A family of gas dynamics configurations suggest that weakly nonlinear gas dynamics provides a mechanism for the observed S_k (chapter 6).
- S_k depends only weakly on the three-dimensional turbulence structure (chapter 7).

Chapter 2

Simulation details

This chapter discusses the configuration simulated to study turbulence interactions and near-field pressure fluctuations observed near free-shear-flow turbulence.

2.1 Simulation configuration

The three-dimensional compressible flow equations, formulated in Cartesian coordinates, were solved for the temporally developing shear layer shown in figure 2.1. The nondimensional independent variables of space and time are

$$x = \frac{x^*}{l^*},\ y = \frac{y^*}{l^*},\ z = \frac{z^*}{l^*},\ t = \frac{t^* c^*_\infty}{l^*}, \tag{2.1}$$

and the flow variables have been nondimensionalized as

$$\rho = \frac{\rho^*}{\rho^*_\infty},\ u_i = \frac{u^*_i}{c^*_\infty},\ T = \frac{T^* c^*_p}{(c^*_\infty)^2},\ p = \frac{p^*}{\rho^*_\infty (c^*_\infty)^2}. \tag{2.2}$$

The $()^*$ quantities represent dimensional variables and the free stream values of density, pressure, and speed of sound are denoted by ρ_∞, p_∞, and c_∞, respectively. The specific heat at constant pressure is c^*_p. With the nondimensionalization defined above, the compressible-fluid flow equations of mass, momentum, and energy are

$$\frac{\partial \rho}{\partial t} + \frac{\partial (\rho u_i)}{\partial x_i} = 0, \tag{2.3}$$

$$\frac{\partial (\rho u_i)}{\partial t} + \frac{\partial}{\partial x_j}(\rho u_i u_j) = -\frac{\partial p}{\partial x_i} + \frac{\partial \tau_{ij}}{\partial x_j}, \tag{2.4}$$

$$\frac{\partial e}{\partial t} + \frac{\partial}{\partial x_i}\left[u_i (e + p)\right] = -\frac{\gamma}{RePr(\gamma - 1)} \frac{\partial^2}{\partial x_i^2}\left(\frac{p}{\rho}\right) + \frac{\partial}{\partial x_i}(\tau_{ij} u_j), \tag{2.5}$$

respectively. The viscous stress tensor, assuming a Newtonian fluid and neglecting any bulk viscosity, is

$$\tau_{ij} = \frac{1}{Re}\left(\frac{\partial u_i}{\partial x_j} + \frac{\partial u_j}{\partial x_i} - \frac{2}{3}\frac{\partial u_k}{\partial x_k}\delta_{ij}\right). \tag{2.6}$$

The nondimensional ideal gas law

$$p = \frac{\gamma - 1}{\gamma} \rho T \tag{2.7}$$

provides the total energy

$$e = \frac{p}{\gamma - 1} + \frac{1}{2} \rho u_i u_i. \tag{2.8}$$

The flow equations (2.3), (2.4) and (2.5) have parameters that are the ratio of specific heats

$$\gamma \equiv \frac{c_p^*}{c_v^*} = 1.4, \tag{2.9}$$

the Reynolds number

$$Re = \frac{\rho_\infty^* c_\infty^* l^*}{\mu^*}, \tag{2.10}$$

and the Prandtl number

$$Pr \equiv \frac{c_p^* \mu^*}{\kappa^*} = 0.7. \tag{2.11}$$

The dynamic viscosity (μ^*) and thermal conductivity (κ^*) are assumed constant. The Reynolds number (2.10) based on speed of sound is useful for nondimensionalizing the flow equation. However, the Reynolds number that reflects a more useful comparison between flows of different speed for a free-shear layer configuration is based on the fluid velocity difference,

$$Re_{\delta_m} = \frac{\rho_\infty \Delta U^* \delta_m^*(t)}{\mu^*}. \tag{2.12}$$

The Reynolds number and momentum thickness Reynolds number are related by

$$Re_{\delta_m} = ReM \delta_m^*(t)/l^*, \tag{2.13}$$

where the flow Mach number is

$$M = \frac{\Delta U^*}{c_\infty^*}. \tag{2.14}$$

In figure 2.1, the flow domain dimensions are $(L_x \times L_y \times L_z) = (1536 \times 1600 \times 512)\, \delta_m^o$, where $\delta_m^o = \delta_m(0)$ is the momentum thickness which is defined at any time as

$$\delta_m(t) = \frac{1}{\rho_\infty \Delta U^2} \int_{-L_y/2}^{L_y/2} \bar{\rho} (\tfrac{1}{2}\Delta U - \tilde{u})(\tfrac{1}{2}\Delta U + \tilde{u})\, dy. \tag{2.15}$$

In (2.15), $\bar{()}$ and $\tilde{()}$ indicate Reynolds and Favre averages, respectively.

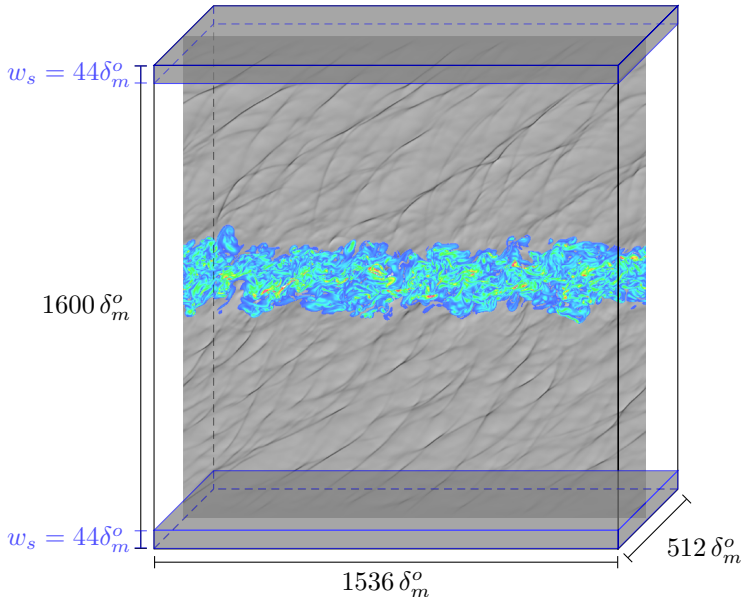

Figure 2.1: Simulation domain schematic. The shaded regions represent the extent of the sponge in (2.20).

For most of the simulations as shown in table 2.1, the Reynolds number in (2.12) was $Re_{\delta_m} = 60$, initially, and reached 2100 when $\delta_m(t)/\delta_m^o = 35$. A supplementary $M = 2.5$ flow at $Re_{\delta_m^o} = 120$ was simulated until $Re_{\delta_m} = 4200$ to assess Reynolds number sensitivity. To assist transition to turbulence, the planar shear layers were initialized with velocity perturbations using the approach of Kleinman & Freund (2008), which were added to a streamwise velocity profile

$$\bar{u}(y) = \frac{\Delta U}{2} \tanh\left(5\frac{y}{\delta_m^o}\right). \tag{2.16}$$

No additional disturbances were added to the initial density or pressure fields. Four flow speeds—$M = 0.9$, 1.5, 2.5, and 3.5—were simulated until the time when $\delta_m(t) = 35\,\delta_m^o$. The current simulations, though with a relatively small initial $Re_{\delta_m^o}$ are simulated in a large domain to attain converged S_k statistics, assess the propagation effects of crackle, and grow the shear layers to $35\,\delta_m^o$, which results in a relatively large final Reynolds number based on δ_{99},

$$Re_{\delta_{99}} = \frac{\rho_\infty \Delta U \delta_{99}}{\mu}, \tag{2.17}$$

as summarized in table 2.1.

M	$Re_{\delta_m^o}$	Re_{δ_m}	$Re_{\delta_{99}}$	$\Delta x/\delta_m^o$	$\Delta y/\delta_m^o$	$\Delta z/\delta_m^o$
0.9	60	2100	7980	1	1	1
1.5	60	2100	8190	1	1	1
2.5	60	2100	9240	1	1	1
2.5	120	4200	18480	0.5	0.5	0.5
2.5	120	4200	18480	1	1	1
3.5	60	2100	10920	1	1	1

Table 2.1: Grid resolution and final Reynolds number. The final Reynolds number for Re_{δ_m} and $Re_{\delta_{99}}$ are taken when $\delta_m(t)/\delta_m^o = 35$.

The choice of initial Reynolds number with corresponding grid resolution was chosen in part based on previous studies listed in table 2.2.

Reference	M	$Re_{\delta_m^o}$	Re_{δ_m}	$\Delta x/\delta_m^o$	$\Delta y_{\min}/\delta_m^o$	$\Delta z/\delta_m^o$
Pantano & Sarkar (2002)	0.6	160	1526	0.672	0.672	0.672
Pantano & Sarkar (2002)	1.4	160	1303	0.672	0.672	0.672
Pantano & Sarkar (2002)	2.2	160	1776	0.675	0.675	0.677
Kleinman & Freund (2008)	0.9	35	233	5.9	4.68	9.03
Kleinman & Freund (2008)	0.9	69	485	2.94	2.34	4.49
Kleinman & Freund (2008)	0.9	207	1442	0.976	0.79	1.47
Kleinman & Freund (2008)	0.9	414	2848	0.976	0.79	1.47
Zhou *et al.* (2012)	0.7	92	1680	0.673	0.775	0.631

Table 2.2: Grid resolution and final Reynolds number of previous compressible mixing layer simulations.

2.2 Numerical methods

The domain in figure 2.1 was uniformly discretized with $N_x \times N_y \times N_z = 1536 \times 1601 \times 512$ mesh points. The resolution of the larger Reynolds number simulation ($Re_{\delta_m^o} = 120$) for $M = 2.5$ was increased by a factor of two. The interior derivatives in each coordinate direction are computed with fourth-order, 13-point, resolution-optimized finite-differences. Near-boundary grid points in the y-direction use reduced-order central differences and one-sided differences at the domain extent. These are not expected to degrade the solution since they are far from the turbulence and inside absorbing sponge zones whose effect will be discussed later. The second-order, mixed derivatives for the viscous terms on the right side of (2.4) and (2.5) were approximated by repeated first-order finite-differences. Fourier analysis of the finite-difference approximations provides an approximate dispersion relation to compare to the exact relation. Figure 2.2 (a) and (b) shows the resolution properties of the first- and second-order interior derivatives, respectively. Details of the finite-difference stencil coefficients for the schemes of the simulations are provided in appendix A.

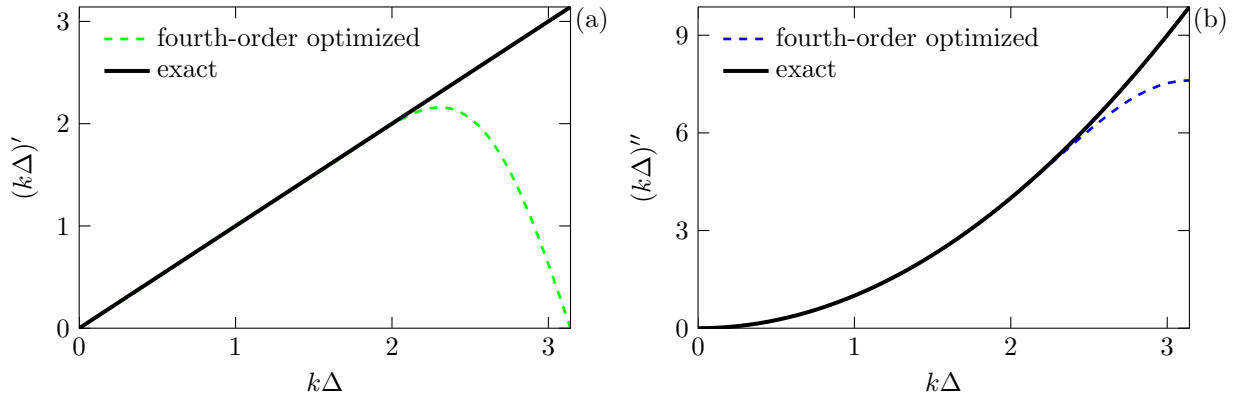

Figure 2.2: Modified wave number assessment of resolution for the (a) first and (b) second derivative approximations.

In implementing the simulations, we truncate the y-extent, and at this point, it is important that the computational boundary mimics the properties of a radiation boundary conditions so numerical reflections do not degrade the solution. Experience has shown for flows of this kind (Kleinman & Freund, 2008) that a combination of an absorbing sponge (Freund, 1997*b*) augmented with one-dimensional characteristic radiation boundary conditions (Thompson, 1987) can achieve the desired radiation-like behavior, provided that the amplitude of fluctuating quantities leaving the domain is sufficiently small. To help ensure the fluctuations of quantities are small near the boundaries, sponge regions of width $w_s = 44\,\delta_m^o$ at $y = \pm L_y/2$ are included with a source term on the right-hand-side of the governing equations of the form

$$\mathcal{N}(\mathbf{q}) = -\xi(y)(\mathbf{q} - \mathbf{q}_{\text{target}}). \tag{2.18}$$

The target solution vector for our configuration is

$$\mathbf{q}_{\text{target}} = \left[\rho_\infty, \pm\rho_\infty \frac{\Delta U}{2}, 0, 0, \frac{p_\infty}{\gamma - 1} + \frac{1}{2}\rho_\infty \left(\frac{\Delta U}{2}\right)^2\right], \tag{2.19}$$

which forces the solution vector $\mathbf{q}$ toward the ambient, free-stream conditions. The sponge strength increases quadratically toward the domain extent as

$$\xi(y) = \begin{cases} \frac{1}{2}\left[\frac{|y| - \left(\frac{L_y}{2} - w_s\right)}{w_s}\right]^2, & |y| > \frac{L_y}{2} - w_s \\ 0, & \text{otherwise} \end{cases}. \tag{2.20}$$

Numerical stabilization

To suppress the mild instabilities these numerical schemes are known to have, selective high-wavenumber numerical filtering was applied in all three coordinate directions, as is often done (Kleinman & Freund, 2008). A 13-point, fourth-order filter (Bogey & Bailly, 2004) was applied every $5\,\Delta t$ to each conservative variable. The filter selectively reduces energy in high-wavenumber components: the wavenumber $k_c\Delta = 1.81$ had 1% reduction upon application, and 100% at $k_c\Delta = \pi$, as shown in figure 2.3. Details of the finite-difference filter is provided in appendix A. Extensive numerical tests, which will explained later in section 3.2, show that the filtering affects only the targeted high-wave-number range of the flow which contains little energy. In section 4.1.4 (figure 4.12), key quantities of crackle are also shown to be insensitive to the filter application.

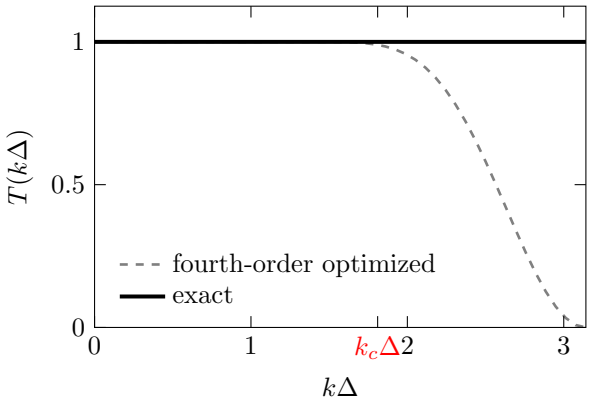

Figure 2.3: Transfer function $T(k\Delta)$ of the selective high-wavenumber filtering scheme.

Time integration

The flow solution $(\mathbf{q}_i)$ was advanced in time $t_{i+1} = t_i + \Delta t$ using an explicit fourth-order Runge–Kutta method

$$\mathbf{q}_{i+1} = \mathbf{q}_i + \frac{1}{6}\left(\mathbf{s}_1 + 2\mathbf{s}_2 + 2\mathbf{s}_3 + \mathbf{s}_4\right), \tag{2.21}$$

where each stage $(\mathbf{s}_i)$ is

$$s_1 = \Delta t\mathbf{R}(\mathbf{q}_i, t_i) \tag{2.22}$$

$$s_2 = \Delta t\mathbf{R}(\mathbf{q}_i + \tfrac{1}{2}\mathbf{s}_1, t_i + \tfrac{1}{2}\Delta t) \tag{2.23}$$

$$s_3 = \Delta t\mathbf{R}(\mathbf{q}_i + \tfrac{1}{2}\mathbf{s}_2, t_i + \tfrac{1}{2}\Delta t) \tag{2.24}$$

$$s_4 = \Delta t\mathbf{R}(\mathbf{q}_i + \mathbf{s}_3, t_i + \Delta t). \tag{2.25}$$

The operator $\mathbf{R}(\mathbf{q}_i, t_i)$ is the discretized right side of (2.3)–(2.5). The time step was set to a constant of $\Delta t = 0.02\delta_m^o/\Delta U$ so that the ratio of the maximum acoustic velocity scale with respect to the mesh scale $(\Delta x/\Delta t)$,

$$\max\left((|u|+c)\tfrac{\Delta t}{\Delta x} + (|v|+c)\tfrac{\Delta t}{\Delta y} + (|w|+c)\tfrac{\Delta t}{\Delta z}\right), \tag{2.26}$$

remained below 0.5 during all of the simulations.

Chapter 3

Turbulence

This chapter confirms that the turbulence develops to be realistic and consistent with measurements and simulations. We also provide detailed documentation of the fundamental turbulence statistics some of which will be referenced in chapter 6 for parameterizing skewness models with scales from the DNS. The effects of the Reynolds number, numerical dissipation, and domain size for the $M = 2.5$ flow are discussed in section 3.2 and 3.3.

3.1 Shear-layer development

The growth of turbulent shear layers is shown in figure 3.1. After spreading by a factor of about 3, which has been observed in simulations of this kind (Pantano & Sarkar, 2002; Kleinman & Freund, 2008), the growth is approximately linear between $20 < \delta_m(t)/\delta_m^o < 35$.

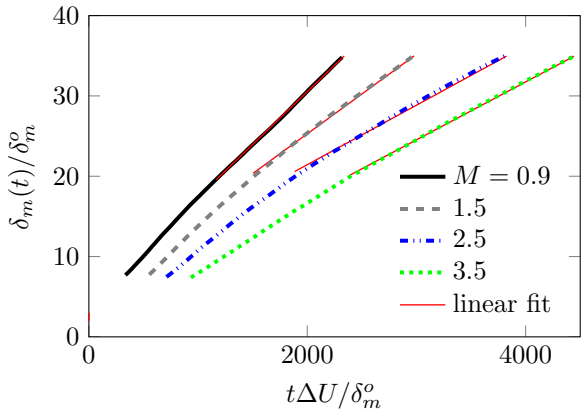

Figure 3.1: Effect of Mach number on the shear layer growth.

Taking the time derivative of (2.15) and neglecting molecular dissipation effects on the mean flow, which are known to be small (Vreman *et al.*, 1996), the momentum thickness growth rate is

$$\dot{\delta}_m(t) = -\frac{2}{\rho_\infty \Delta U^2} \int_{-L_y/2}^{L_y/2} \bar{\rho} \widetilde{u''v''} \frac{\partial \tilde{u}}{\partial y}\, dy, \tag{3.1}$$

where $(''$) represents a Favre fluctuation,

$$q'' = q - \frac{\overline{\rho q}}{\bar{\rho}}. \tag{3.2}$$

Figure 3.2 shows that the growth rate of the simulations normalized by the incompressible growth rate. As expected, based on previous observation, the shear layer growth is suppressed with increasing

$$M_c = \frac{U_j}{c_\infty + c_j}, \tag{3.3}$$

and the trends with M_c compare well with observations from spatially-developing shear flows (Elliott & Samimy, 1990; Goebel & Dutton, 1991; Debisschop *et al.*, 1994) and simulations of other temporally-developing mixing layers (Pantano & Sarkar, 2002; Kleinman & Freund, 2008).

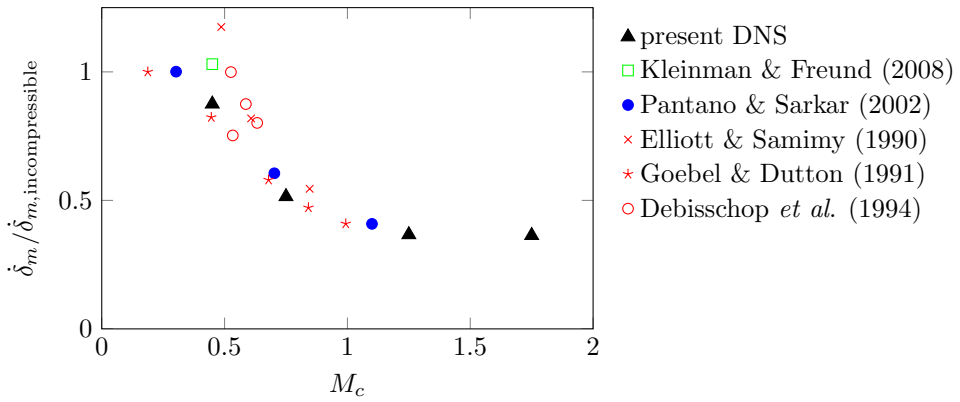

Figure 3.2: Effect of M_c on the shear layer growth rate.

In a self-similar, temporally developing flow, the Reynolds stresses depend only on $y/\delta_m(t)$. The evolution of Reynolds stress profiles from the simulated turbulence for $M = 0.9$–3.5 are shown in figures 3.3–3.6. For $M = 0.9$, the collapse of their spatial profiles between $\delta_m(t)/\delta_m^o = 10$ to 30 suggest an approximate self-similar development. For Mach numbers $M \gtrsim 1.5$, the self-similar collapse of the Reynolds stresses is not as clear as for the $M = 0.9$. Elliott & Samimy (1990) reported that for higher convective Mach numbers the development to self-similarity was more gradual than for subsonic flows. Previous simulations of temporally-

developing shear layers also show that a longer time is needed to achieve approximate self-similarity for compressible shear layers (Pantano & Sarkar, 2002), which is consistent with our observations for $M \gtrsim 1.5$.

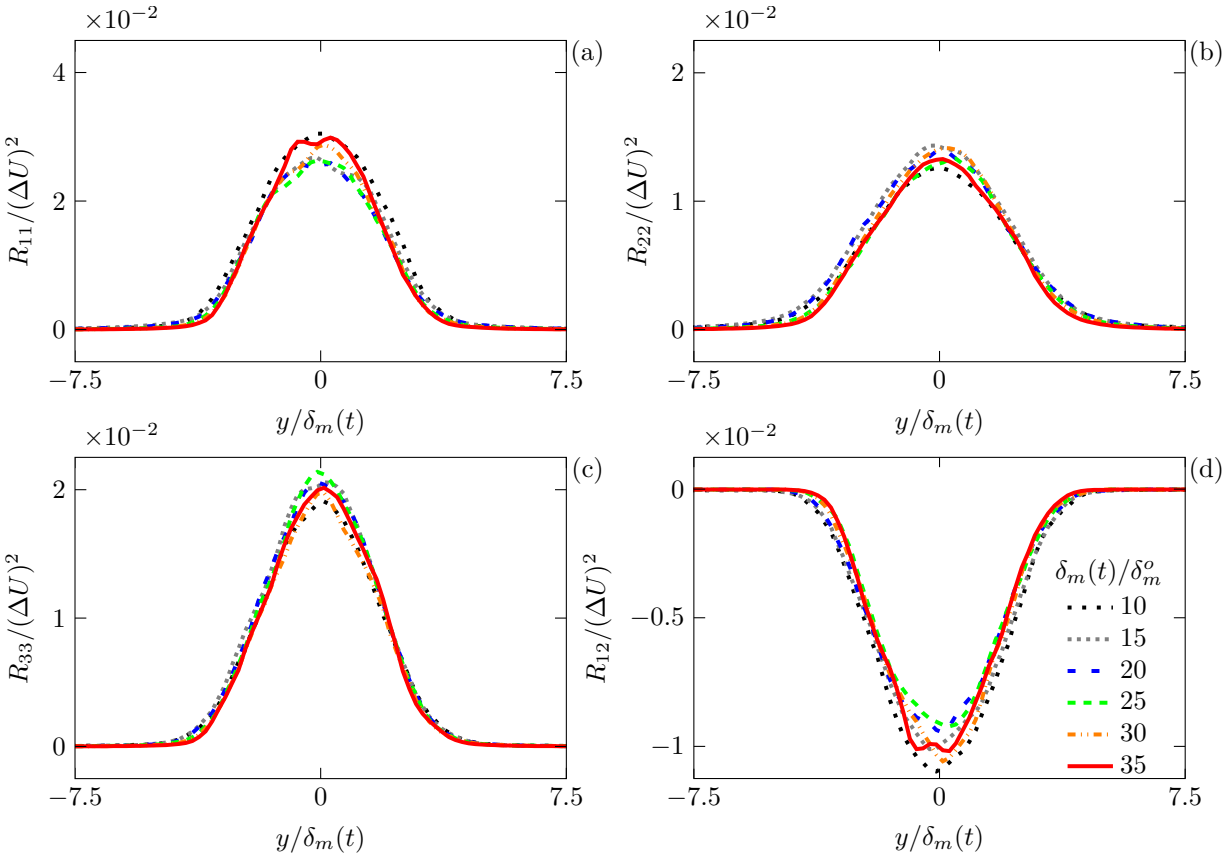

Figure 3.3: Reynolds stress profiles for $M = 0.9$ with shear layer growth.

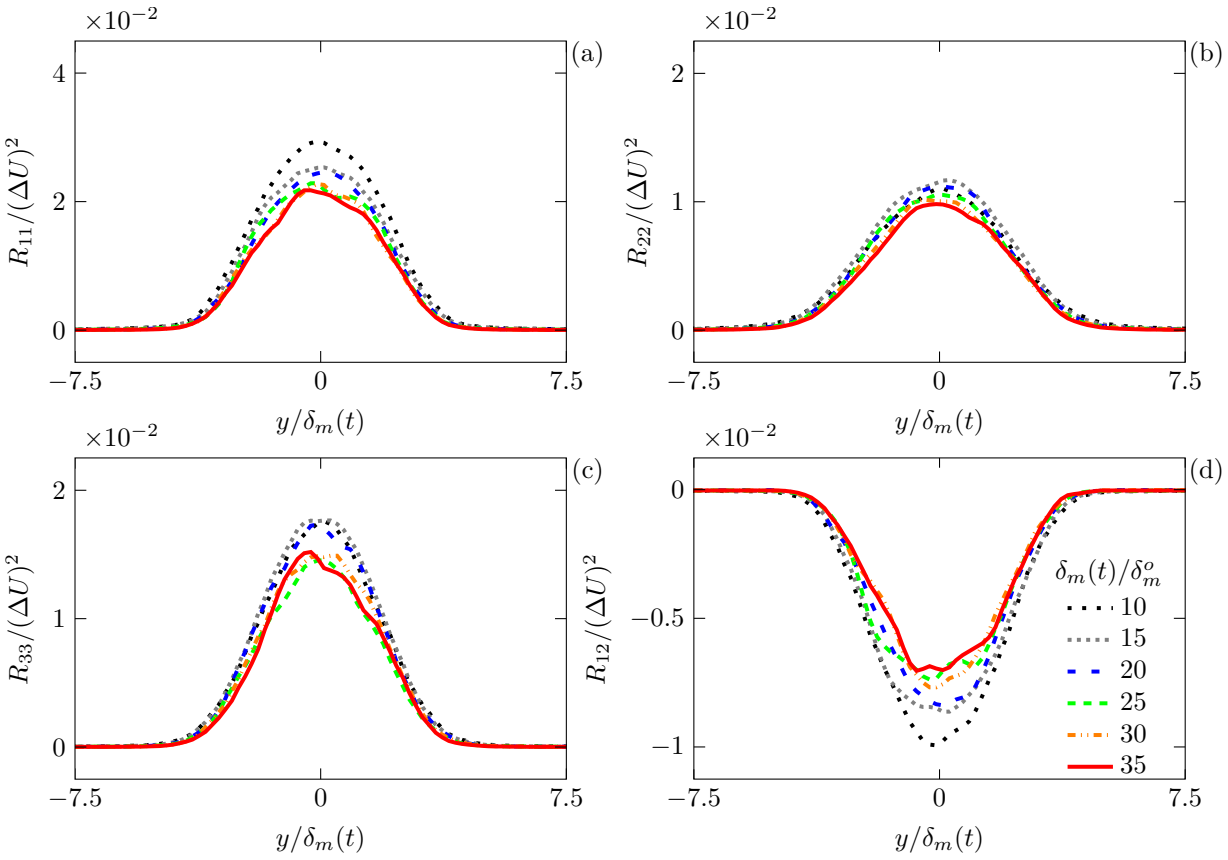

Figure 3.4: Reynolds stress profiles for $M = 1.5$ with shear layer growth.

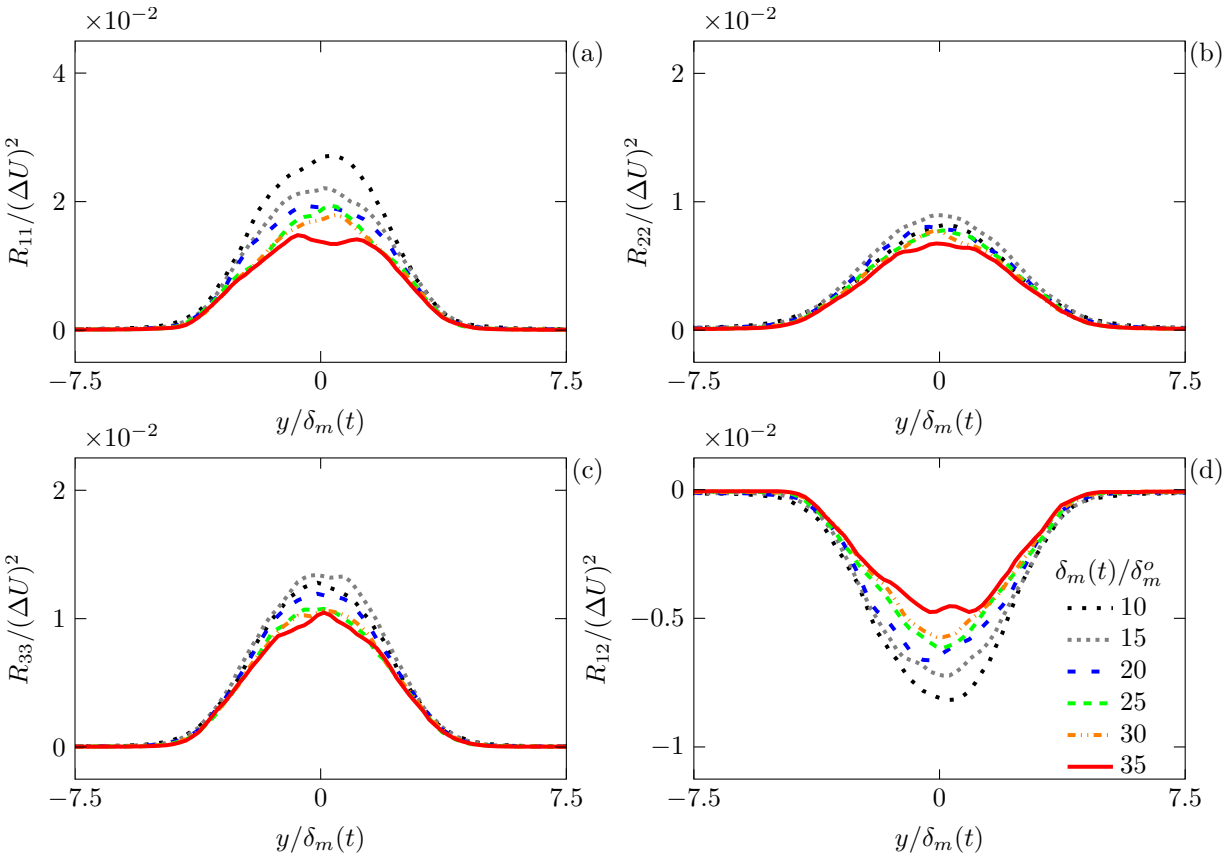

Figure 3.5: Reynolds stress profiles for $M = 2.5$ with shear layer growth.

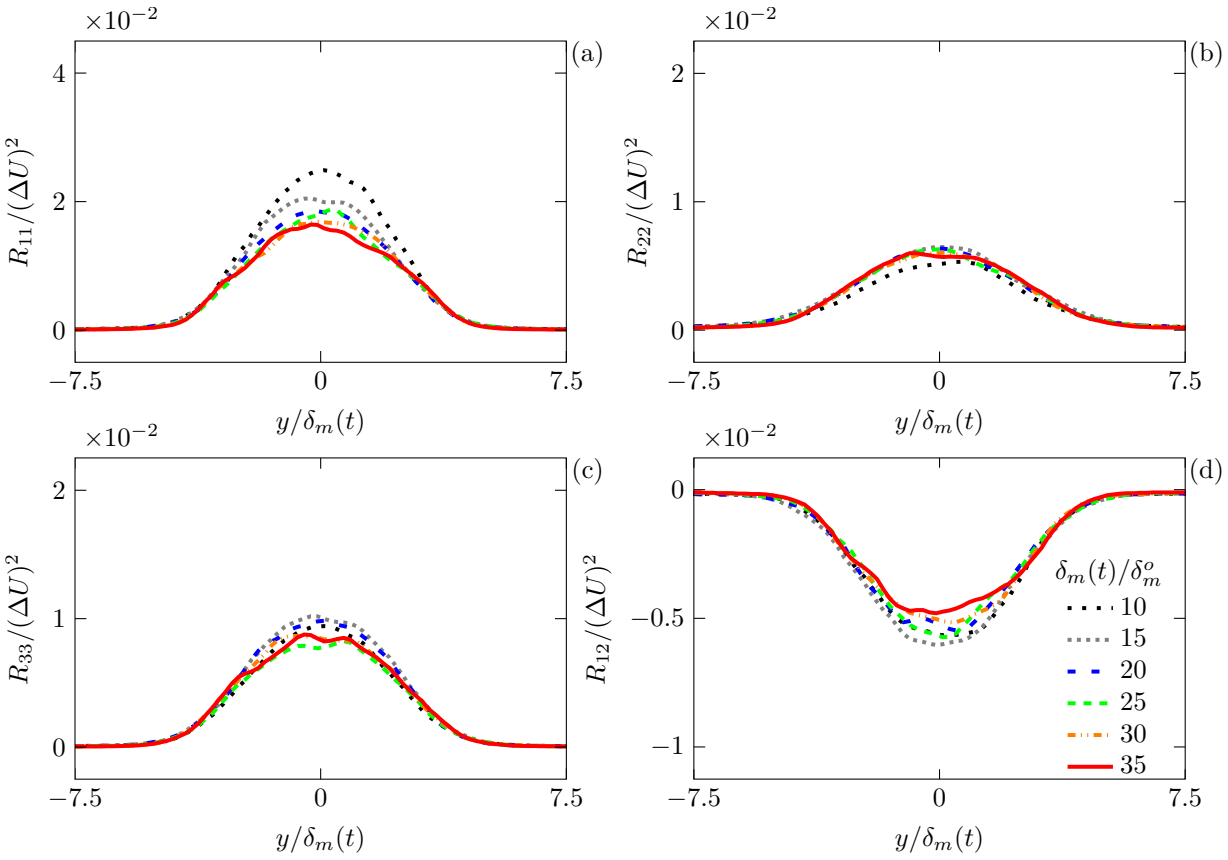

Figure 3.6: Reynolds stress profiles for $M = 3.5$ with shear layer growth.

The average Reynolds stress profiles are shown in figure 3.7. All of the components of the peak turbulence intensities decrease with M_c as shown in figure 3.8. The current DNS reproduces the same trend as seen in simulation (Pantano & Sarkar, 2002; Kleinman & Freund, 2008; Foysi & Sarkar, 2010) and within the scatter of observations in the experiments (Elliott & Samimy, 1990; Goebel & Dutton, 1991; Debisschop *et al.*, 1994) at similar Mach numbers.

We note here that all of the statistical quantities are averaged over the periodic x- and z-directions during the shear layer growth between $\delta_m(t)/\delta_m^o = 20$ and 35 for discrete t intervals of $20\delta_m^o/\Delta U$ (every $100\,\Delta t$). For the results presented in the coordinates, $|y|/\delta_m(t)$, the values are averaged at their corresponding $\pm y$ locations,

$$q\left(|y|/\delta_m\right) = \frac{1}{2}\left[q(y/\delta_m) + q(-y/\delta_m)\right], \tag{3.4}$$

due to the symmetry of the temporally-developing flow. We will show later, for quantities assessing crackle noise, that the average is insensitive to including more samples (see section 4.1.6 and 5.2.5).

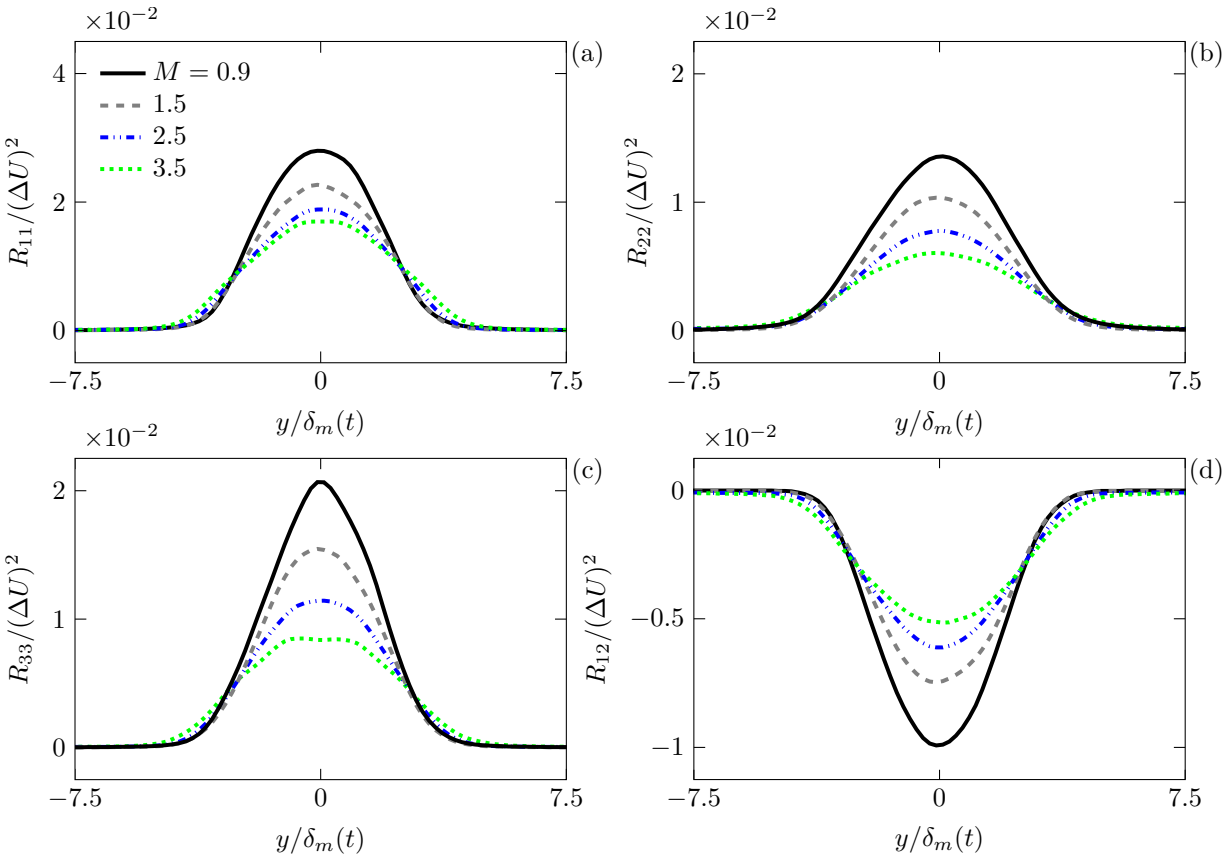

Figure 3.7: Effect of Mach number on the average Reynolds stress profiles.

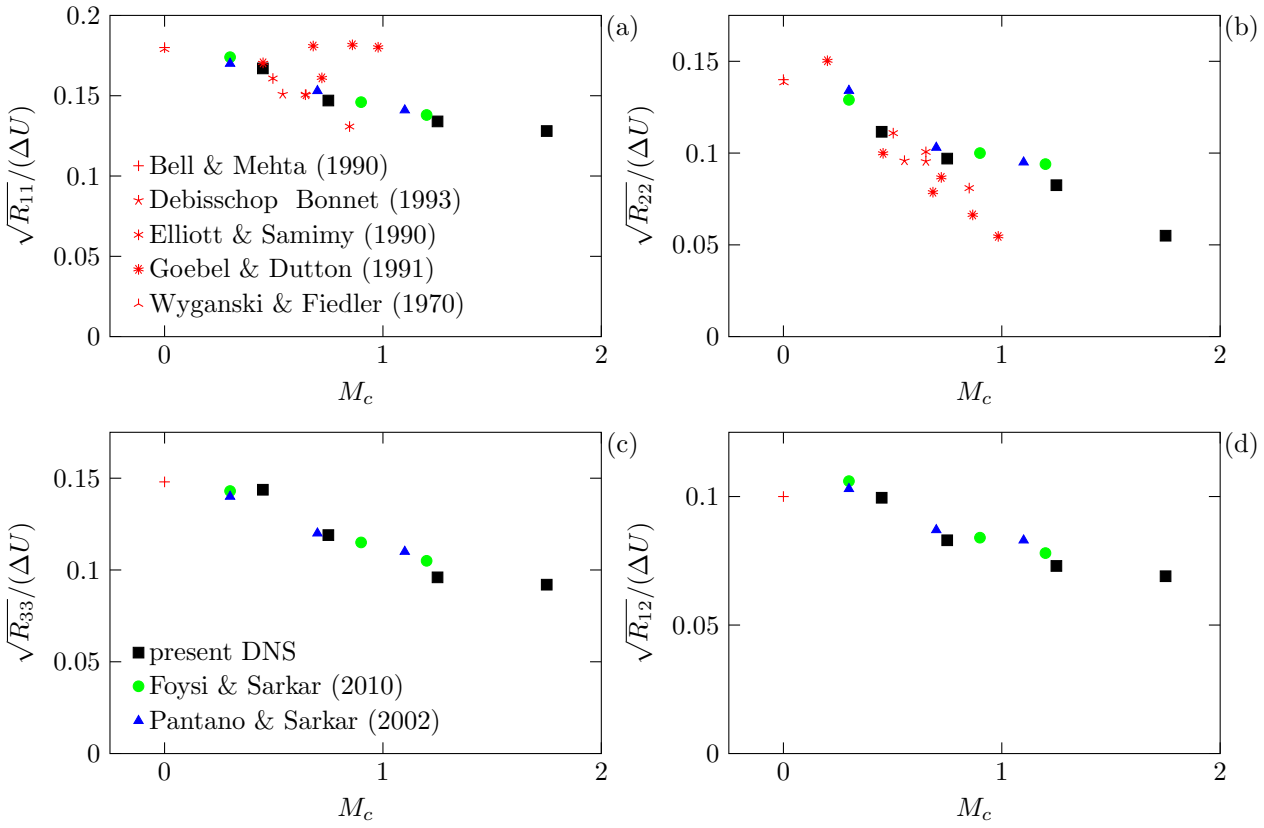

Figure 3.8: Effect of M_c on the peak turbulent intensities.

3.1.1 Turbulence spectra

The range of turbulence length scales are quantified with the midplane u-velocity spectra in figure 3.9. The turbulence spectra are broadbanded and appear realistic, though it is not expected that an inertial subrange would be clear at this Reynolds number (Pantano & Sarkar, 2002; Kleinman & Freund, 2008). The energy in the wavenumbers beyond $k\delta_m \gtrsim 10$ also decreases with increasing M, which is consistent with mixing layer simulations at similar Mach numbers (Pantano & Sarkar, 2002).

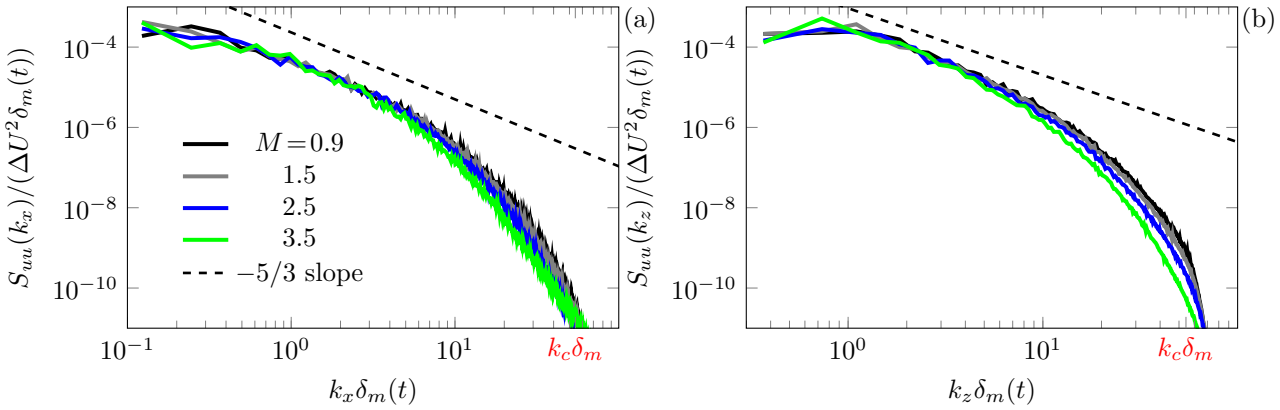

Figure 3.9: Effect of Mach number on the u-velocity energy spectra at $y = 0$ when $\delta_m(t)/\delta_m^o = 30$ in the (a) streamwise and (b) spanwise direction.

3.2 Reynolds number and numerical dissipation effects

For $Re_{\delta_m^o} = 60$ and 120, the spectra collapse at the largest, most energetic scales for $k\,\delta_m^o < 0.01$. In the larger Reynolds number flows, the range of energetic scales broadens beyond $k\,\delta_m^o > 0.03$. Comparing the $\Delta = 1\,\delta_m^o$ and the higher resolution $\Delta = 0.5\,\delta_m^o$ at $Re_{\delta_m^o} = 120$, the two spectra collapse until $k_c^I = k\,\delta_m^o \approx 1.81$, where the high-wavenumber filtering affects these smaller scales (see figure 2.3). The pressure spectra in figure 3.11 show a similar collapse as the velocity spectra.

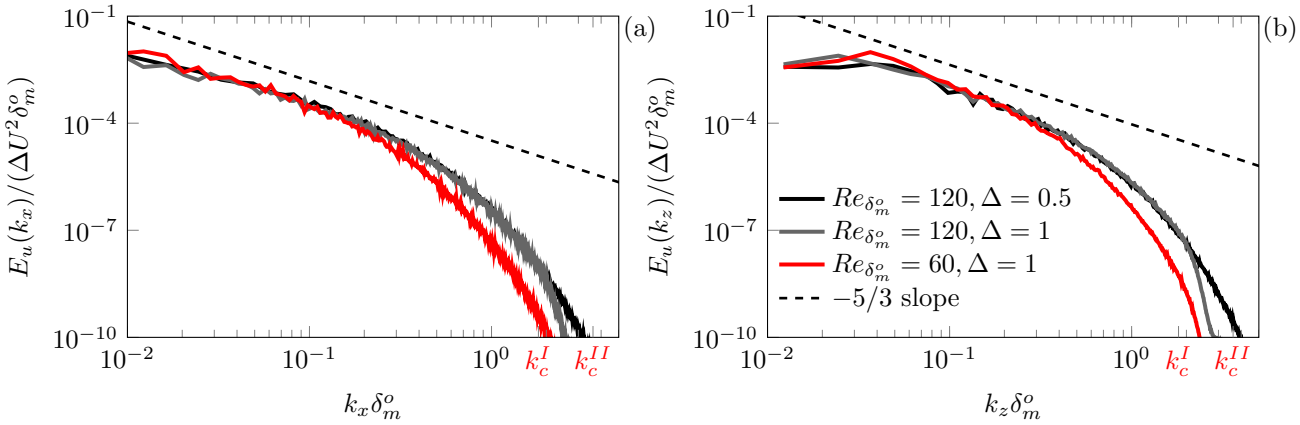

Figure 3.10: Effect of the Reynolds number on the u-velocity energy spectra for $M = 2.5$ at $y = 0$ when $\delta_m(t)/\delta_m^o = 30$ in the (a) streamwise and (b) spanwise direction.

We test the filter affect by varying the frequency at which the filter is applied, which is similar to the approach taken in previous work (Pantano & Sarkar, 2002). We consider three schedules: applying the filter

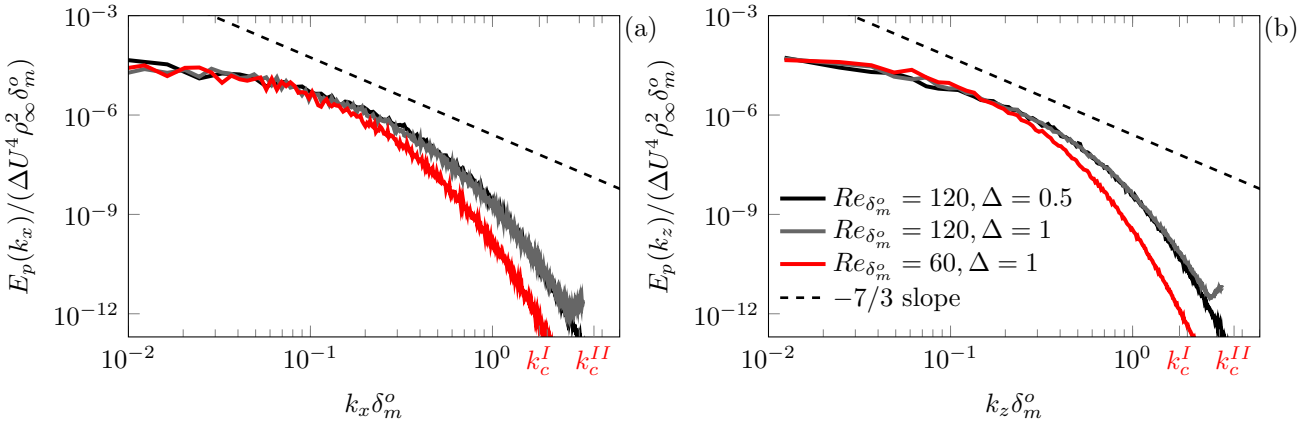

Figure 3.11: Effect of the Reynolds number on the pressure spectra for $M = 2.5$ at $y = 0$ when $\delta_m(t)/\delta_m^o = 30$ in the (a) streamwise and (b) spanwise direction.

every one, five, and fifty time steps. For most of our simulations, we apply the numerical filter every five time steps. The midplane u-velocity and pressure spectra are shown in the streamwise and spanwise directions in figure 3.12–3.13, respectively, to highlight the filter's effect on the energy in the high-wavenumber region of the spectrum. The filter application after every time step affects the high wavenumbers beyond $k\,\delta_m^o > 1.81$. The wavenumber $k\,\delta_m^o = 1.81$ corresponds to the length scale at which 1% of the energy is dissipated as shown in figure 2.3.

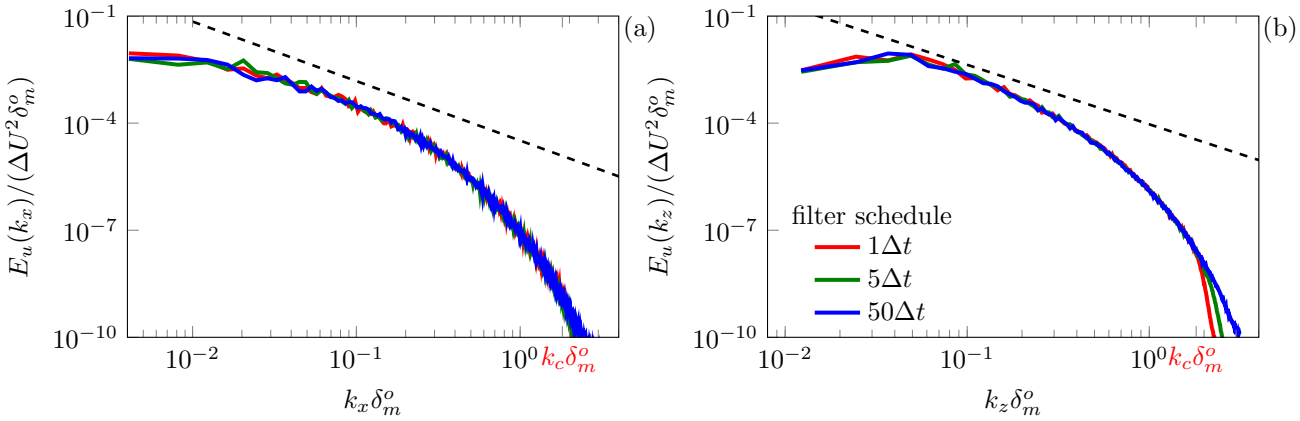

Figure 3.12: Effect of the numerical filter on the u-velocity spectra in the (a) streamwise and (b) spanwise direction.

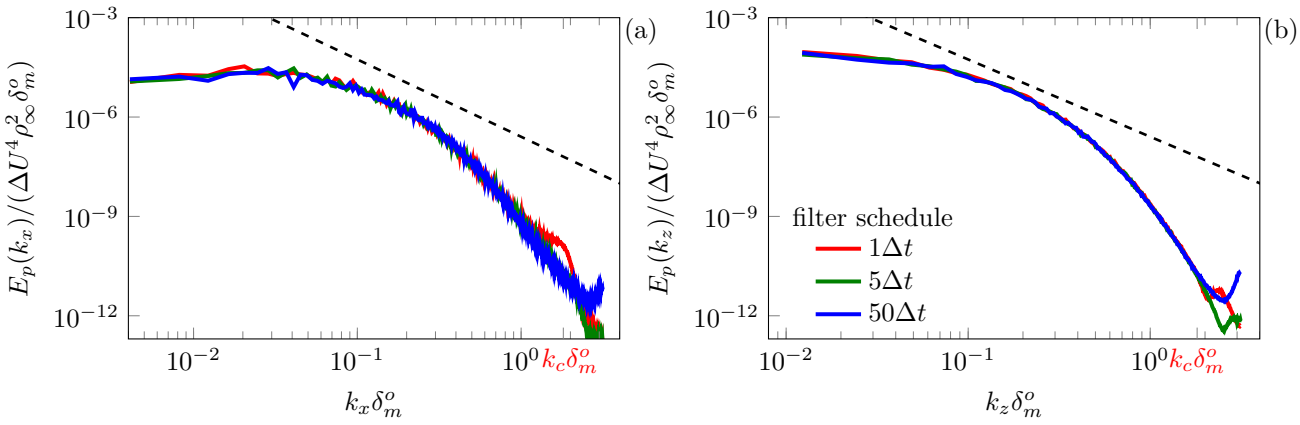

Figure 3.13: Effect of the numerical filter on the pressure spectra in the (a) streamwise and (b) spanwise direction.

We now examine the effect of the filter on the dissipation spectrum which we take in the streamwise direction

$$D(k_x) = 2\nu k_x^2 S_{uu}(k_x), \tag{3.5}$$

with the kinematic viscosity $\nu = \mu_\infty/\rho_\infty$. For the filter schedule $50\Delta t$, the wavenumber where 99% of the total dissipation spectrum,

$$\frac{\sum_{k_x=0}^{k_{99}} D(k_x)}{\sum_{k_x} D(k_x)} = 0.99, \tag{3.6}$$

is $k_{99}\eta = 0.678$ compared to the filter wavenumber cutoff, $k_c\eta = 1.225$, as shown in figure 3.14. This quantifies that the filter affects short wavelengths beyond the wavenumber where 99% of the dissipation spectrum is resolved in the DNS.

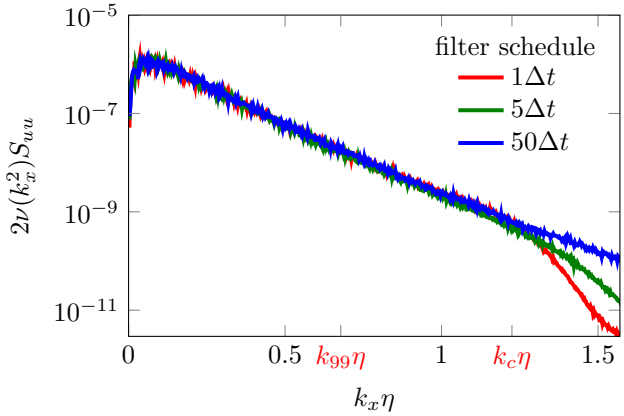

Figure 3.14: Effect of the numerical filter on the one-dimensional dissipation spectrum for $M = 2.5$. The wavenumber k_{99} is the scale at which 99% of the spectrum energy is resolved (see text). The wavenumber corresponding to 1% dissipation by the numerical filter is $k_c\eta$.

3.3 Domain and grid effects

The previous section showed that the simulations have adequate resolution for $Re_{\delta_m^o} = 60$ to 120. We now assess the effect of the domain size on the turbulence for $M = 2.5$. Table 2.2 summarizes the grids used in this study. Note that simulation (a) has the same number of points as (b), but the resolution in the z-direction is 50% less. The effect of these grids on the pressure statistics are examined in section 4.1.5.

Simulation	$N_x \times N_y \times N_z$	M	$Re_{\delta_m^o}$	$\Delta x/\delta_m^o$	$\Delta y/\delta_m^o$	$\Delta z/\delta_m^o$
(a)	$768\times801\times256^*$	2.5	60	1	1	1.5
(b)	$768\times801\times256$	2.5	60	1	1	1
(c)	$1152\times801\times384$	2.5	60	1	1	1
(d)	$1536\times1601\times512$	2.5	60	1	1	1

Table 3.1: Simulation configurations for domain and grid sensitivity.

Figure 3.15 shows the collapse of growth rate with configurations in table 3.1, indicating that the shear layer growth is insensitive to the grid.

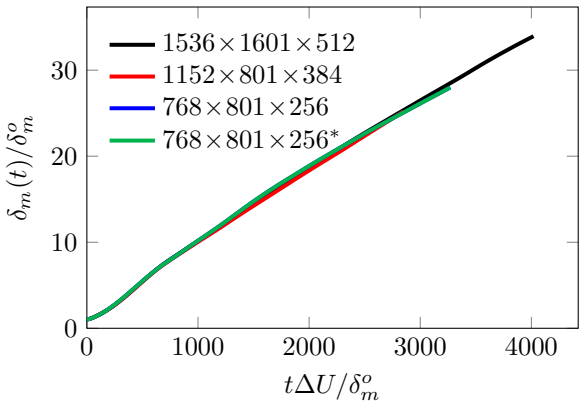

Figure 3.15: Effect of domain size on the shear layer growth for $M = 2.5$.

The collapse of the midplane u'-velocity and p' spectra are shown in figure 3.16 and 3.17, respectively. Differences arise at the low-wavenumber spectrum due to difference in the domain extents. In figure 3.16 (b), the roll-off in the spectra at $k_z/\delta_m^o > 1$ for case (a) $768\times801\times256^*$ is due to its lower resolution in the z-direction. The collapse of the pressure spectra at the midplane agree well for all of the resolutions in table 3.17.

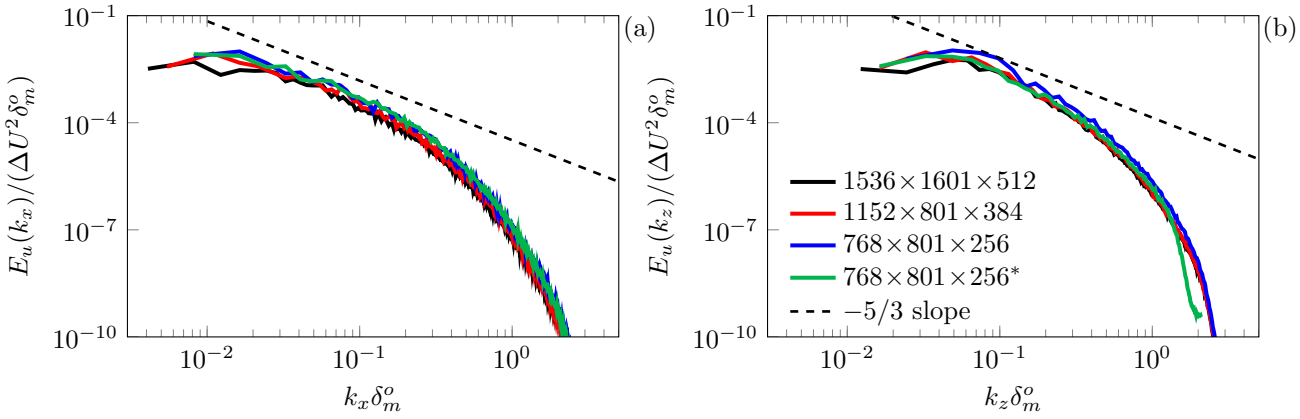

Figure 3.16: Effect of domain size on the u-velocity energy spectra for $M = 2.5$ at $y = 0$ when $\delta_m(t)/\delta_m^o = 20$ in the (a) streamwise and (b) spanwise direction.

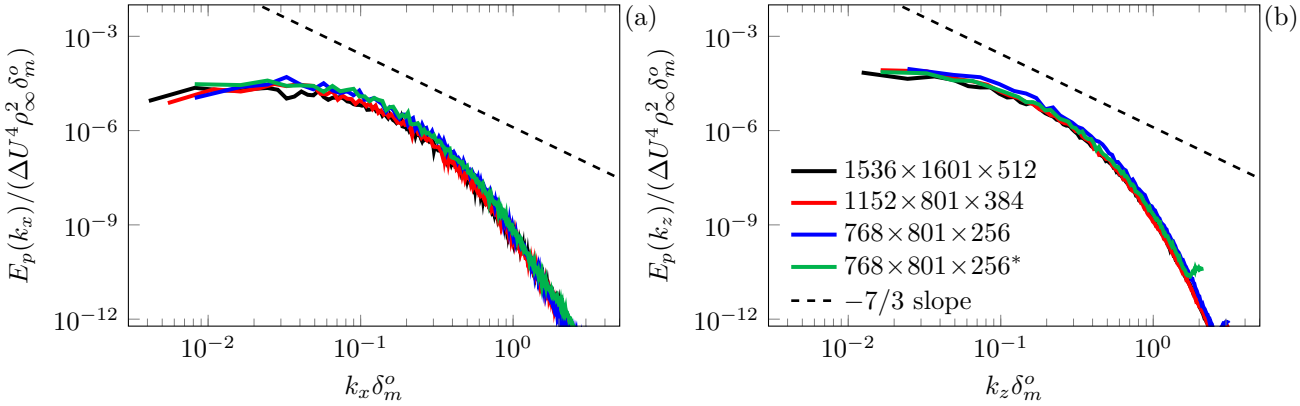

Figure 3.17: Effect of domain size on the pressure spectra for $M = 2.5$ at $y = 0$ when $\delta_m(t)/\delta_m^o = 20$ in the (a) streamwise and (b) spanwise direction.

The two-point correlation of turbulence quantities (figures 3.18–3.22) shows that the turbulence decays rapidly to zero within the domain size for all of the simulations, which confirms that the largest grid ($1536 \times 1601 \times 512$), which is used in most of the simulations, does not to constrain the turbulence.

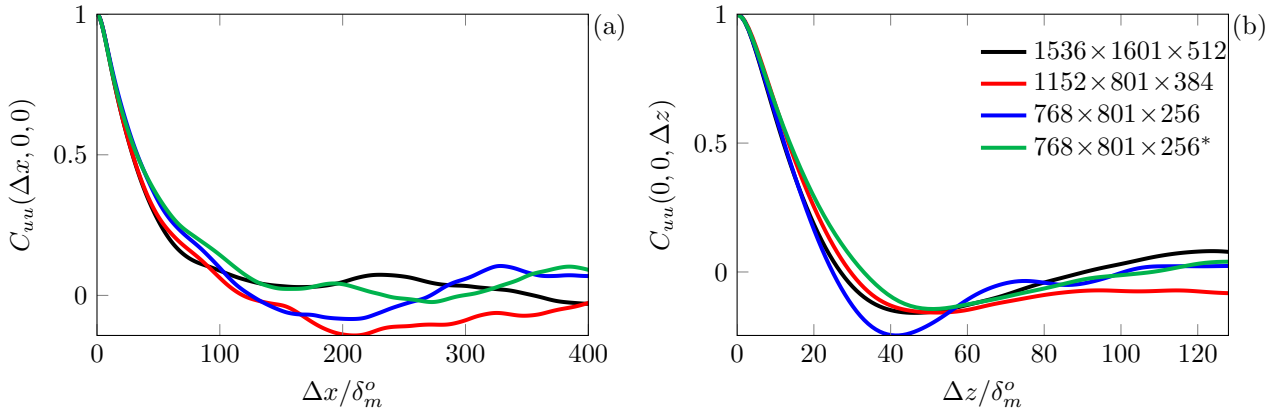

Figure 3.18: Effect of domain size on the two-point u-velocity correlation in the streamwise (a) and spanwise (b) directions for $M = 2.5$ when $\delta_m(t)/\delta_m^o$=20.

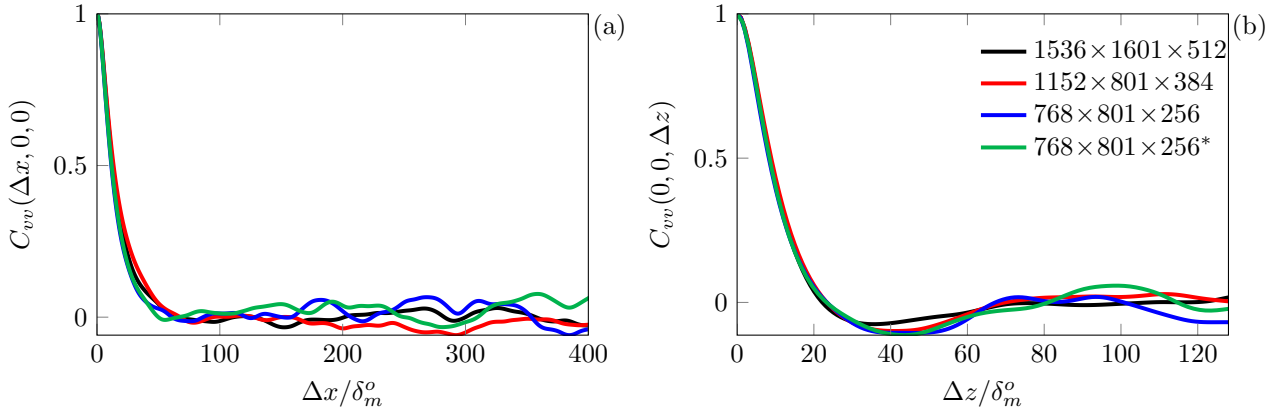

Figure 3.19: Effect of domain size on the two-point v-velocity correlation in the streamwise (a) and spanwise (b) directions for $M = 2.5$ when $\delta_m(t)/\delta_m^o$=20.

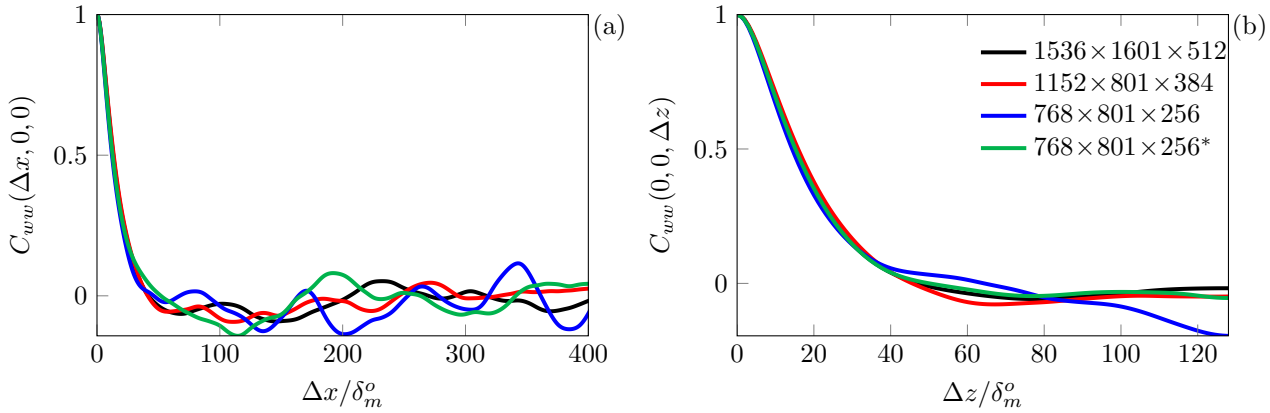

Figure 3.20: Effect of domain size on the two-point w-velocity correlation in the streamwise (a) and spanwise (b) directions for $M = 2.5$ when $\delta_m(t)/\delta_m^o$=20.

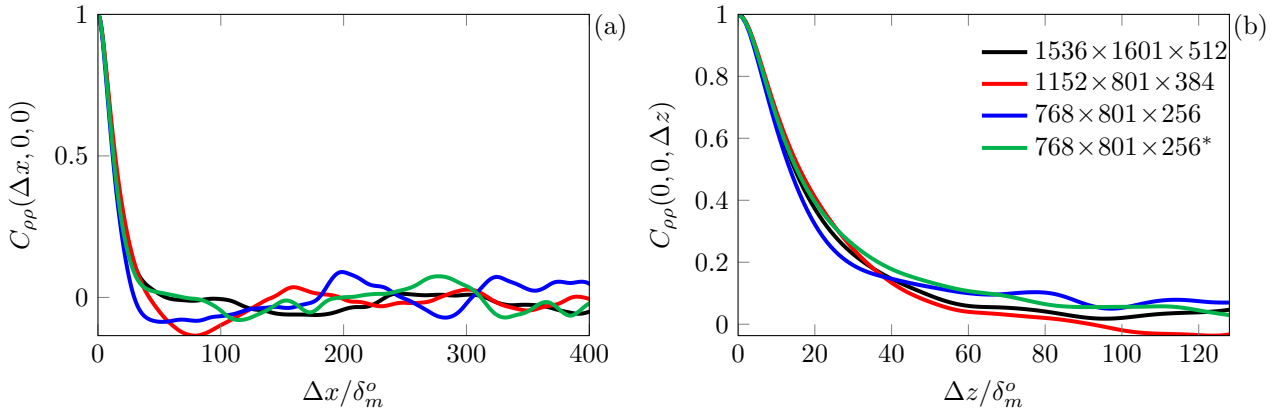

Figure 3.21: Effect of domain size on the two-point density correlation in the streamwise (a) and spanwise (b) directions for $M = 2.5$ when $\delta_m(t)/\delta_m^o$=20.

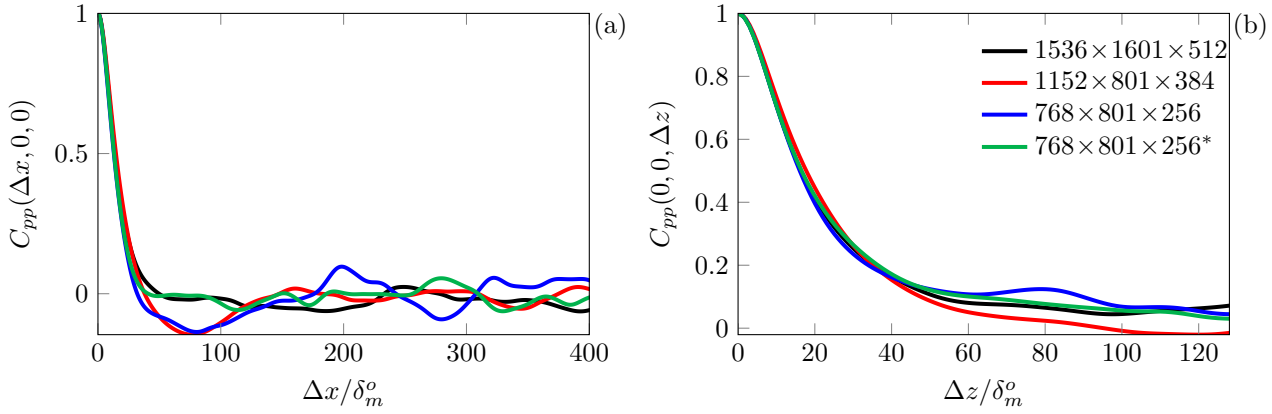

Figure 3.22: Effect of domain size on the two-point pressure correlation in the streamwise (a) and spanwise (b) directions for $M = 2.5$ when $\delta_m(t)/\delta_m^o$=20.

3.4 Turbulence and the near-acoustic field

In later assessments of crackle, it will be useful to distinguish between the turbulence and the near-acoustic field. Since there is not one unique measure of this, we evaluate and compare several statistical measures. The first indicator corresponds to the flow location where the mean u-velocity reaches 99% of the free-stream value called δ_{99}. This y-location corresponds to approximately free-stream conditions with low shear and therefore low turbulence production, though δ_{99} is not a direct measure of these. This location is extracted from the mean u-velocity profiles in figure 3.23. The value of δ_{99} increases with flow speed ranging between $\delta_{99} = 4.2$ to 5.1 between $M = 0.9$ and 3.5, respectively. Table 3.2 summarizes the corresponding δ_{99} values for each flow speed.

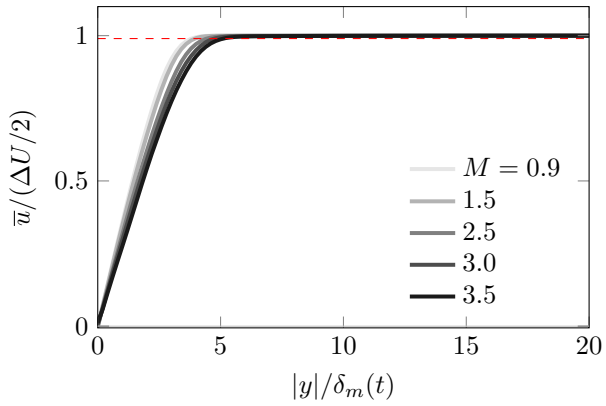

Figure 3.23: Effect of Mach number on the average u-velocity with distance from the mixing layer. The red dashed line corresponds to $0.99\,\Delta U/2$.

In the high-shear regions at $y = 0$, the vorticity magnitude is maximum, and we use a threshold

$$\frac{|\nabla \times \mathbf{u}|}{|\nabla \times \mathbf{u}|_{y=0}} = 10^{-3} \tag{3.7}$$

to discriminate between the rotational region and the approximately irrotational near-field. The normalized vorticity magnitude with distance from the mixing layer is shown in figures 3.24. A complementary assessment considers the ratio of acoustic to vortical disturbances,

$$\frac{(\nabla \cdot \mathbf{u}')^2}{|\nabla \times \mathbf{u}'|^2} \tag{3.8}$$

which was also used by Duan *et al.* (2014) to establish the character of the field above high-speed boundary layers. The y-location where vorticity magnitude is 10^{-3} and those where (3.8) is 10^3 is reported in table 3.2. Both indicators increase with M and span $y/\delta_m = 4.92$ to 8.83.

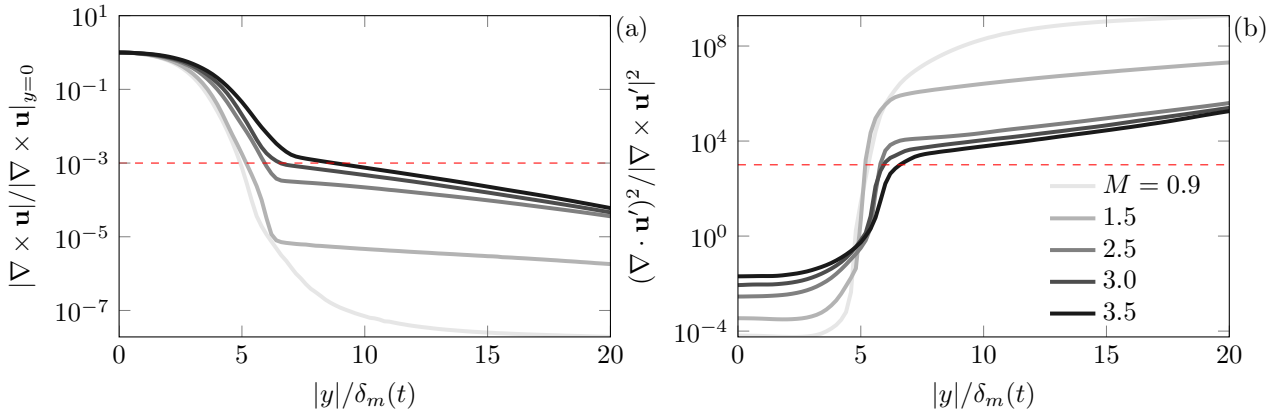

Figure 3.24: Effect of Mach number on the (a) vorticity magnitude and (b) the ratio of vortical disturbances to acoustic ones with distance from the mixing layer. The red dashed line corresponds to 10^{-3} in (a) and 10^3 in (b).

We next appeal to a thermodynamic assessment to distinguish the turbulent field from the regions that are approximately isentropic, since the thermodynamic quantities in the acoustic field are isentropic. We consider the location in the mixing layer where the pressure-density and pressure-temperature correlations are

$$\frac{\overline{p'\rho'}}{p'_{\text{rms}}\rho'_{\text{rms}}} = 0.99 \tag{3.9}$$

$$\frac{\overline{T'\rho'}}{T'_{\text{rms}}\rho'_{\text{rms}}} = 0.99, \tag{3.10}$$

as shown in figure 3.25 (a) and (b), respectively. The location at the thresholds increase with M and range from 4.83–6.33 and 5.19–6.98 for (3.9) and (3.10), respectively. Table 3.2 summarizes their values.

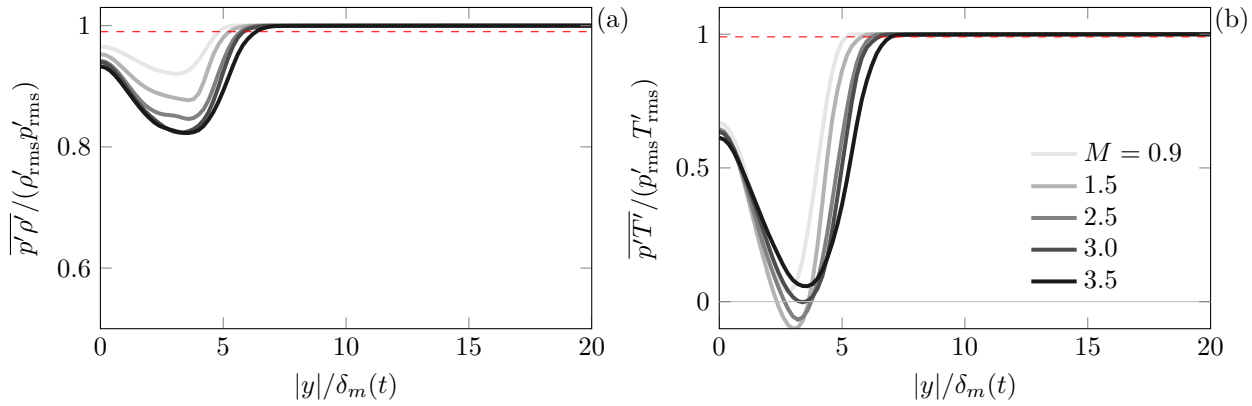

Figure 3.25: Effect of Mach number on the (a) pressure-density correlation and (b) pressure-temperature correlation with distance from the mixing layer. The red dashed line corresponds to the correlation value of 0.99.

As one might anticipate, not one of these quantities provides a distinct location that separates the turbulent field from the non-turbulent field, through there is reasonable agreement $3.8 < y/\delta_m < 8.83$ for the range of quantities we consider. For that reason, we will typically mark $\overline{\delta_{99}} = 4.4$ as an indication of the transition between the turbulence and the near-acoustic field, keeping in mind that this marker is mildly sensitive to M and that it is not unique to other considerations.

M	δ_{99}	$\overline{\lvert\omega\rvert}$	$\overline{d'd'}/\overline{\omega'\omega'}$	$\overline{\rho'p'}$	$\overline{p'T'}$	average
0.9	3.8	4.92	5.25	4.83	5.19	4.8
1.5	3.9	5.17	5.11	5.26	5.78	5.0
2.5	4.4	5.91	5.78	5.7	6.2	5.6
3	4.8	6.52	5.90	5.81	6.49	5.9
3.5	5.2	8.83	6.59	6.33	6.98	6.8
average	4.4	6.3	5.9	5.6	6.1	–

Table 3.2: Location at $y/\delta_m(t)$ for different thresholds marking the near field (see text in section 3.4).

3.5 Statistical moments of velocity

Gas dynamics models in chapter 6 that will be used to explain source mechanisms of skewness are informed by the statistical moments of velocity components within the turbulence. Figure 3.26 shows distribution of u'-velocity at the midplane of the mixing layers. The distributions appear symmetric and its width decreases with M. Table 3.3-3.4 summarizes the moments for u'- and v'-velocity in the DNS. The intensities, u'_{rms} and v'_{rms}, decrease with M which is consistent with experimental observation and simulation as cited in section 3.1.1. Also, the skewness of the velocity components is small $|S_k| < 0.025$ for all M, which is reflected in the visually symmetric distribution in figure 3.26. The kurtosis

$$\kappa = \frac{\overline{(u')^4}}{\overline{(u')^2}^2}, \tag{3.11}$$

is less than Gaussian ($\kappa = 3$) with $\kappa = 2.6$ to 2.9, and it does not appear to have a Mach number dependence.

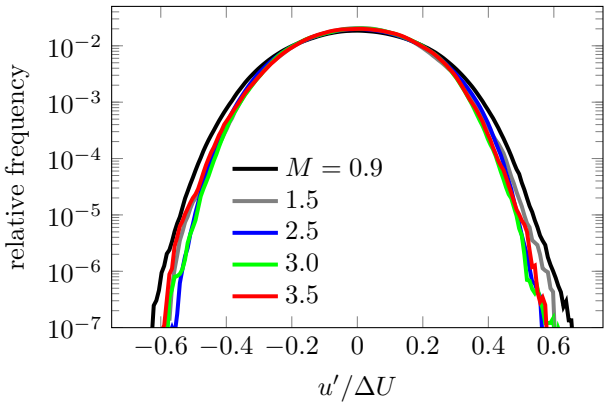

Figure 3.26: Effect of Mach number on the u'-velocity distribution at the midplane.

M	$u'_{\text{rms}}/\Delta U$	$S_k(u')$	$\kappa(u')$
0.9	0.162	-0.014	2.63
1.5	0.153	1.8×10^{-3}	2.61
2.5	0.150	3.5×10^{-4}	2.61
3.0	0.141	-0.021	2.57
3.5	0.142	-0.018	2.63

Table 3.3: Effect of Mach number on the statistical moments of u'-velocity at $y = 0$.

M	$v'_{\text{rms}}/\Delta U$	$S_k(v')$	$\kappa(v')$
0.9	0.112	-0.015	2.77
1.5	0.102	4.1×10^{-3}	2.83
2.5	0.099	4.2×10^{-3}	2.87
3.0	0.095	0.024	2.88
3.5	0.093	4.4×10^{-3}	2.88

Table 3.4: Effect of Mach number on the statistical moments of v'-velocity at $y = 0$.

Chapter 4

The Near-acoustic Field

Chapter 3 focused on turbulence statistics of the simulations, with a goal to confirm consistency with reported jet turbulence. This chapter examines in detail the near-field dynamics leading to crackle noise. In section 4.1.1, we validate that the acoustics above the mixing layers agree with observation and show that the sound intensity scales with the flow speed as expected from aeroacoustic theory: the $\langle p'p' \rangle \sim U^8$ for $M \lesssim 1.5$ and U^3 for $M \gtrsim 2.5$.

Section 4.1 shows that the simulated near-field sound does indeed reproduce the hallmark characteristics of jet crackle: pressure signals have strong, sharp compressions followed by weaker, rounded expansions very near the turbulence. For $M \gtrsim 2.5$, $S_k \gtrsim 0.4$, which is consistent with measurements cited in section 4.1.3. We also confirm that S_k is insensitive to Reynolds number in section 4.1.4, which aligns with previous reports that S_k is independent of jet scale.

Visualizations in section 4.2 show that the near field of crackling flows ($S_k \gtrsim 0.4$) have directional, steepened, shock-like-wave features, consistent with previous observations of jet turbulence at similar Mach numbers. The pressure fields are shown to have a complex, three-dimensional structures with peaked pressure near regions where compression waves intersect. We document the wave angle statistics in section 4.3 and assess the nonlinear propagation effects of wave merging in section 4.4. These results show the presence of near-field nonlinearity close above the turbulence, $y < 20\delta_m$, which lead to additional nonlinear sound mechanics affecting crackle. A statistical assessment of the physical factors, including the essential nonlinear effects, generating and transporting the S_k is provided in the following chapter.

4.1 Pressure characteristics

4.1.1 Pressure intensity

Experimental observations show that the pressure intensity changes character at high speed beyond $M > 1$ (Chobotov & Powell, 1957; Tanna *et al.*, 1976; Seiner *et al.*, 1992; Greska, 2005). For lower speed jets,

Lighthill's famous eighth power law for the radiated acoustic power,

$$\langle p'p' \rangle \propto U_j^8, \tag{4.1}$$

has been successful at predicting the scaling of noise levels (Lighthill, 1952; Crighton, 1975). Ffowcs Williams (1963) expanded upon Lighthill's basic theory to include eddy convection along with a statistical distribution of eddies as a more realistic representation of turbulence rather than a single eddy. The change in character of the radiated power at high speed is due to several factors. One, the well-known Doppler effect due to convection increases the efficiency of sound sources, since the self-canceling effects of multipole sources is diminished. Two, convection increases the source's volume which in turn increases its acoustic efficiency due to its increased correlation length. However, the increased source volume with convection has a limiting effect on the total number of eddies that can contribute to the overall sound, since the turbulent volume is fixed. Including these effects, Ffowcs Williams (1963) anticipated that the acoustic intensity scales like U^3, in contrast to U^8, which agrees well with the experimental data at high speed (Chobotov & Powell, 1957; Tanna *et al.*, 1976; Seiner *et al.*, 1992; Greska, 2005).

Figure 4.1 shows that the intensity $\langle p'p' \rangle$ appears to increase according to ΔU^8 for $M \lesssim 1.5$ and with U^3 for $M \gtrsim 2.5$. At $y/\delta_m = 10$ for the $M = 0.9$ case, the intensity appears to scale shallower than U^8 between $M = 0.9$ and 1.5, which may be due to the larger hydrodynamic near field of this subsonic case, primarily made up of evanescent waves, compared to the supersonic flow. Roughly speaking, the characteristics of these near-field evanescent waves do not follow the pressure scaling laws from the propagating wave solution of pressure in the far field. At $y/\delta_m = 20$, the DNS results do show this anticipated switch in scaling with M near $M \approx 2$.

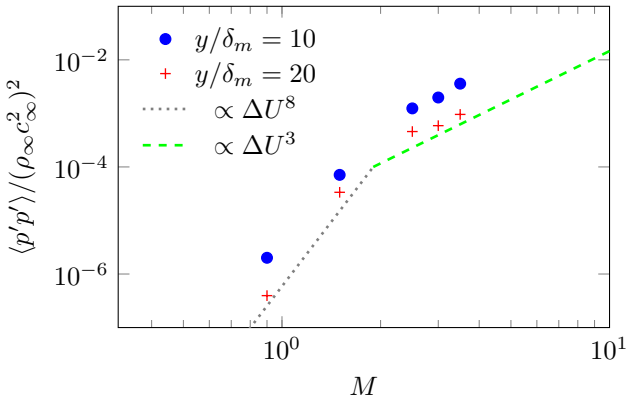

Figure 4.1: Effect of Mach number on the pressure intensity at $y/\delta_m = 10$ and 20.

With the sound intensity increasing with M, we anticipate that any sound field nonlinearities will be

more pronounced at higher M. We will show later in figure 4.6 that $S_k \gtrsim 0.4$ just outside the turbulence, suggesting that crackle is a near source effect, but that does not preclude additional propagation nonlinearity from being important. It is possible to estimate nonlinear effects in propagation using one-dimensional, weakly nonlinear wave theory (Ffowcs Williams *et al.*, 1975; Crighton, 1986; Freund *et al.*, 2000*b*; Petitjean & McLaughlin, 2003; Baars *et al.*, 2014), but these nonlinear assessments do not facilitate an estimate of skewness for crackle. One-dimensional models also miss key features observed in the radiating field near the turbulence: thin, steep, shock-like waves with additional three-dimensional wave–wave interactions. We show in sections 4.2.2 and 4.2.3 that the sound near the turbulence is three-dimensional and that waves nonlinearly merge with nearby waves. Also, the key factors transporting S_k above the mixing layers are shown in chapter 5 to be a fundamentally multidimensional and nonlinear effect.

4.1.2 Pressure traces

As discussed in the chapter 1, the observations of crackle corresponds to asymmetric acoustic signals, and we confirm that the pressure signals from the present simulations reproduce this behavior. Figures 4.2-4.5 show an example pressure trace at a fixed y and z for the different M. For $M \lesssim 1.5$, there are no obvious sharp peaks, and their amplitudes vary about $p' = 0$, symmetrically. In contrast, for $M \gtrsim 2.5$, the asymmetry (stronger $+p'$ than $-p'$) is apparent. Notably, the asymmetry is present at distances $y = 5\delta_m$, for $M \gtrsim 2.5$. The peaked $+p'$ and rounded $-p'$ persist out to $y = 20\delta_m$ in figure 4.5 (c)–(d). Though plotted versus position for the temporally developing flow, the traces from the simulations make the main characteristics of those observed in the acoustic field near round jets. We note that the near-acoustic-field pressure is typically acquired for $r \gtrsim 10D_j$ and often $r > 100D_j$ (Ffowcs Williams *et al.*, 1975; Laufer *et al.*, 1976; Szewczyk, 1978; Krothapalli *et al.*, 2000; Petitjean *et al.*, 2005; Baars & Tinney, 2014). Thus, the current pressure, with its steepened skewed features, suggest that they are already present immediately at the turbulent source, where pressure is not usually reported in experiments.

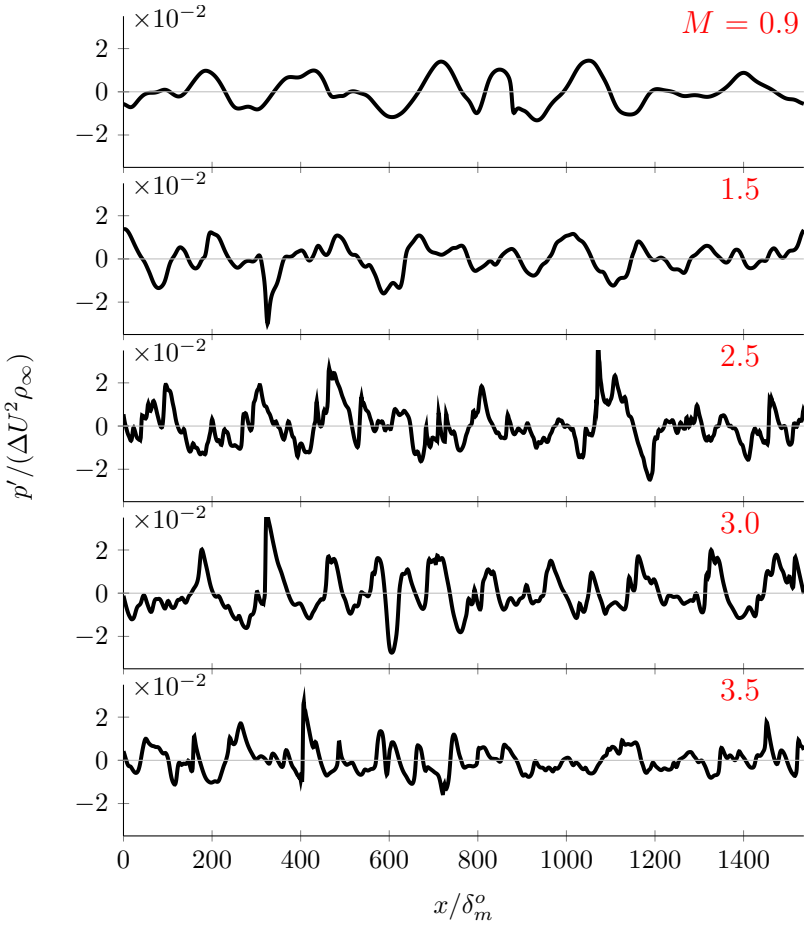

Figure 4.2: Pressure variation with x at $y/\delta_m(t) = 5.$ on $z = 0$ when $\delta_m(t)/\delta_m^o = 10.$

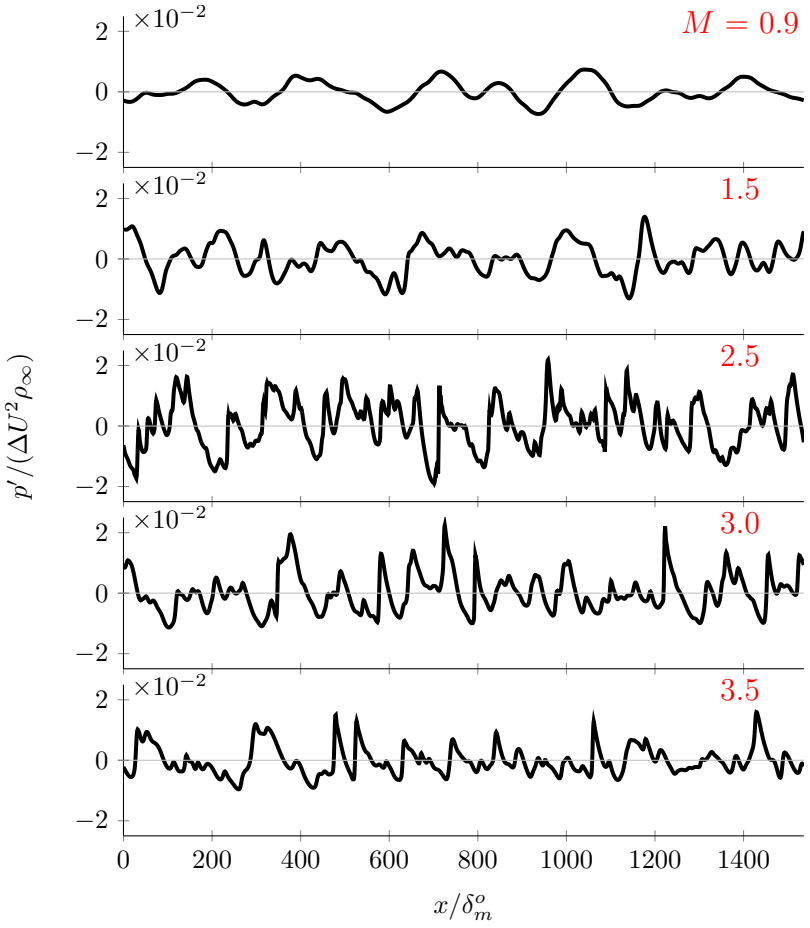

Figure 4.3: Pressure variation with x at $y/\delta_m(t) = 7.5$ on $z = 0$ when $\delta_m(t)/\delta_m^o = 10$.

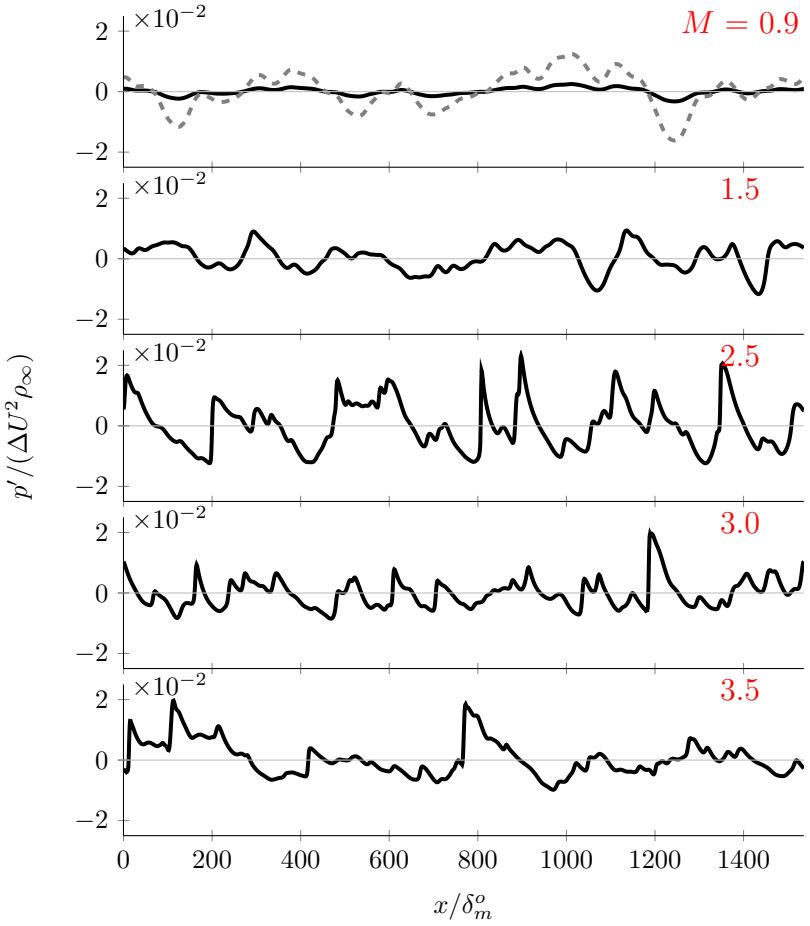

Figure 4.4: Pressure variation with x at $y/\delta_m(t) = 10$ on $z = 0$ when $\delta_m(t)/\delta_m^o = 20$. The dashed line corresponds to $5.0 \times p'$ for $M = 0.9$.

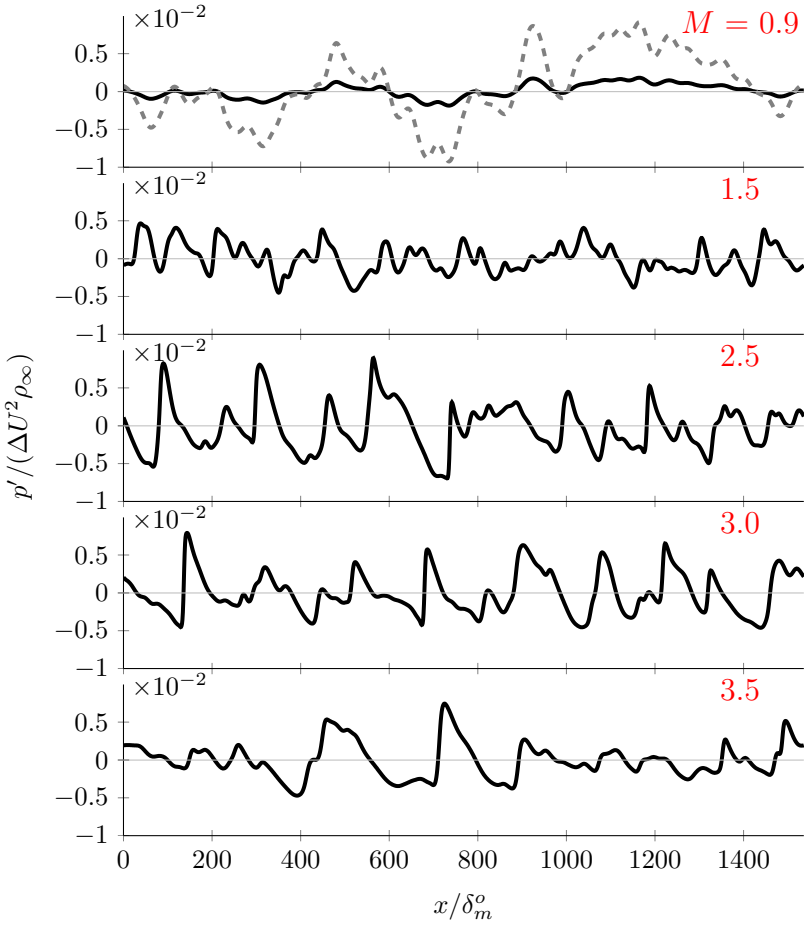

Figure 4.5: Pressure variation with x at $y/\delta_m(t) = 20$ on $z = 0$ when $\delta_m(t)/\delta_m^o = 20$. The dashed line corresponds to $5.0 \times p'$ for $M = 0.9$.

4.1.3 Pressure skewness

Based in part from the initial investigations of Ffowcs Williams *et al.* (1975), we also use $S_k(p')$ as a statistical assessment of the p'-asymmetry observed in the near-field pressure. Figure 4.6 shows that $S_k(p')$ at all y increases with M. This appears to happen continuously, without a distinct transition to a finite S_k and nominally 'crackling' behavior, though the discrete M simulated does not necessarily preclude some sort of jump to finite S_k for $M \approx 1.5$. For $M \gtrsim 2.5$, the $S_k(p')$ exceeds 0.4, which was originally reported by Ffowcs Williams *et al.* (1975) as the approximate skewness when the distinct crackle noise became apparent to the listener. So we typically mark this value for reference, to nominally distinguish between crackle and crackle-free noise, though also keeping in mind that no value of $S_k(p')$ is expected to be a definitive measure of crackle.

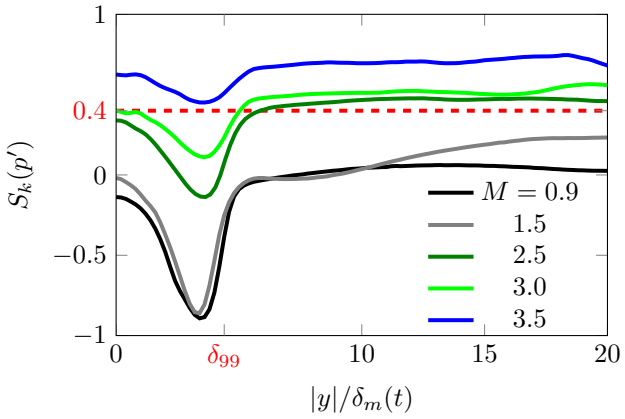

Figure 4.6: Variation of pressure skewness with distance from the mixing layer. The dashed line corresponds to the empirical crackle threshold set by Ffowcs Williams *et al.*, 1975.

For $y \gtrsim \delta_{99}$, $S_k(p')$ is relatively constant, though this is a relatively short range compared to the distances over which S_k is reported to increases with propagation distance (Szewczyk, 1978; Petitjean & McLaughlin, 2003; Petitjean *et al.*, 2005). Similarly, Nichols *et al.* (2013) showed that the skewness above the round jet shear layer, within $\approx 2D_j$ above the visual turbulence, is approximately constant with downstream development of the shear layers. Chapter 5 provides a detailed statistical assessment of the factors transporting S_k in the flow normal direction, and we show that high-order statistics generating S_k are countered by molecular effects over these short distances. This balance of factors then leads to an approximately constant S_k with distance from the mixing layers as seen in figure 4.6.

An advantage of the simplified configuration we consider is that we can study the noise-source mechanics of realistic turbulence in a configuration with only a modest number of parameters. As shown in figure 4.7, the free-shear-flow turbulence (with uniform free-stream temperatures) is set by five parameters

$[\Delta U, \rho_\infty, c_\infty, \mu_\infty, \delta_m, \kappa, \gamma]$. Rather than a single thickness length scale, jets would have a nozzle-lip shear layer thickness, a potential core length, and a diameter. The behavior here thus depends on four nondimensional groups arranged to be the Reynolds number, the flow Mach number, the ratio of specific heats, and the Prandtl number by

$$Re_{\delta_m} = \frac{\rho_\infty \Delta U \delta_m}{\mu_\infty}, M = \frac{\Delta U}{c_\infty}, \gamma = \frac{c_p}{c_v}, Pr = \frac{c_p \mu}{\kappa}.$$

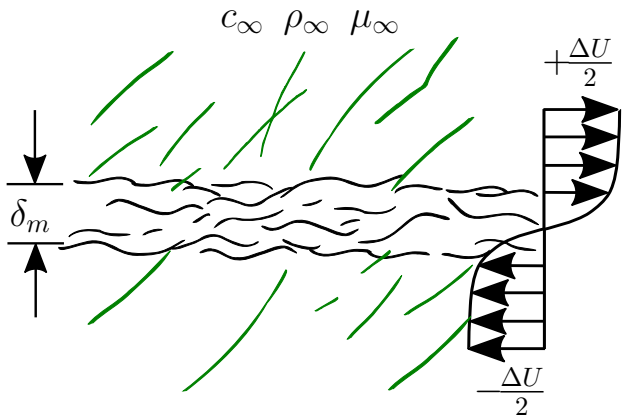

Figure 4.7: Parameters of free-shear flow turbulence with uniform free-stream temperature and zero bulk viscosity.

Results in section 4.1.4 will show that S_k is independent of Re_{δ_m} for the Reynolds number range considered, which is consistent with reports that crackle noise is independent of jet scale (and therefore flow Reynolds number). We now consider its relationship to M as the primary parameter on which S_k depends as initially indicated by the trends in figure 4.6. Since S_k is nearly constant for $\delta_{99} < y < 20\,\delta_m$, as seen in figure 4.6, we average the y-direction,

$$\langle S_k \rangle_{|y|>\delta_{99}} = \frac{1}{n} \sum_{j=1}^{n} S_k(y_j), \tag{4.2}$$

and we observe a monotonic increase with M in figure 4.8. Again, there is not a distinct 'switch' from crackle-free to crackle noise, based in the $S_k \gtrsim 0.4$ denoting crackle noise. However, the skewness increases more rapidly over $M = 0.9$ to 2.5 and slower between $2.5 \lesssim M \lesssim 3.5$ suggesting the possibility of distinct Mach number scaling for low-M ($M \lesssim 2.5$) and high-M ($M \gtrsim 2.5$). A rapid increase in S_k for $M_a \lesssim 1.7$ and slower increase beyond $M_a \gtrsim 1.7$ based on $M_a = U_j/c_\infty$ is also observed in experiments (Ffowcs Williams *et al.*, 1975; Szewczyk, 1978).

We investigate the possibility of distinct M-scaling for skewness and draw from an earlier result to explain this trend. Ffowcs Williams *et al.* (1975) showed that S_k increases approximately linearly with the sound

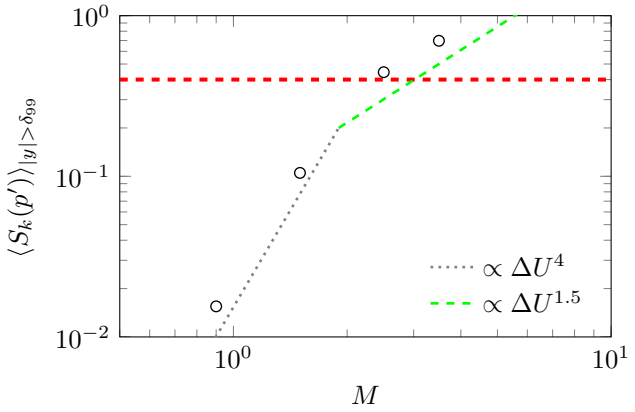

Figure 4.8: Effect of Mach number on the average pressure skewness.

pressure level as is replotted in figure 4.9 (a). We first confirm that the present DNS reproduce this linear behavior in figure 4.9 (b), focusing on data at $y/\delta_m = 20$. The slope in figure 4.9 (b) is $\approx 10\times$ larger than that in (a), which is due to the difference in sound level and location between the experimental measurements ($r/D_j \approx 40$) and the mixing layers ($y/\delta_m = 20$).

Since S_k is approximately linear with p'_{rms}, pressure skewness will have two different M-scalings. We showed in figure 4.1 that the pressure intensity goes like U^8 for $M \lesssim 2.5$ and U^3 beyond $M \gtrsim 2.5$. This implies that S_k will scale like U^4 for $M \lesssim 2.5$ and $U^{1.5}$ for $M \gtrsim 2.5$. The DNS appears to follow these trends in figure 4.8. The conclusion that S_k is less sensitive to changes in M with $M \gtrsim 2.5$ has implications for mitigation strategies of crackle at high speed.

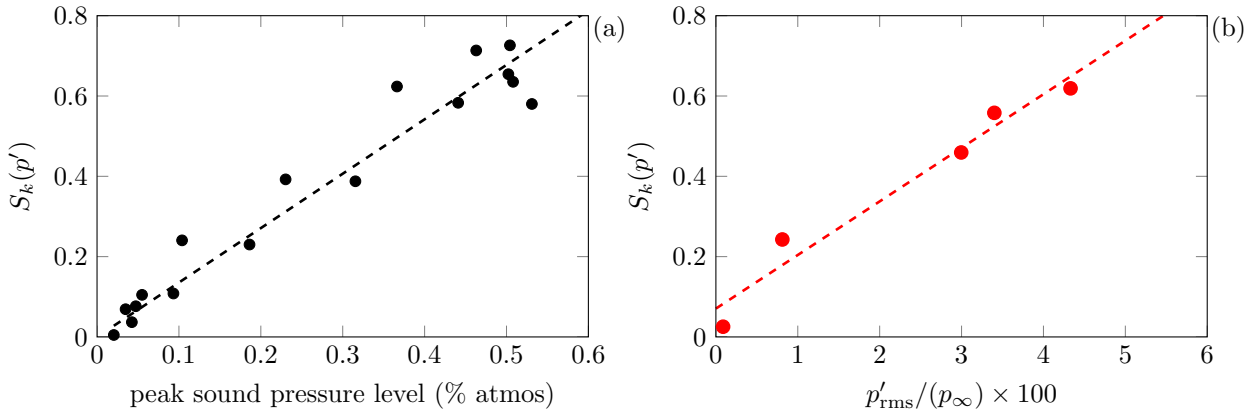

Figure 4.9: Near-field pressure skewness with sound level from the (a) experiments in Ffowcs Williams (1975) and (b) DNS at $y/\delta_m = 20$. The dashed lines correspond to linear fits with the data.

We now—perhaps brazenly—directly compare the S_k in the near-field DNS to the acoustic measurements

of those found near turbulent jets in figure 4.10. We choose to collapse the data using

$$M_o = \frac{M_j}{1 + \frac{c_\infty}{c_j}} \tag{4.3}$$

as a generalized compressibility parameter including the effects of jet temperature (Papamoschou & Roshko, 1988). Figure 4.10 shows that the skewness from the experiments are higher than those in the DNS, and we consider two possibilities for this difference. The first possibility, which has been discussed in this section, is the simulated acoustic field in the DNS does not extend out as as far as those in experiments. Reports have indicated that over relatively long distances, as in the experiments, S_k increases with range (Szewczyk, 1978; Petitjean & McLaughlin, 2003; Petitjean *et al.*, 2005). This somewhat qualifies our conclusion that S_k is primarily a source effect. Although high values of S_k are found at the turbulence source, its larger values observed in the experiment might indicate an additional propagation effect. The close agreement of S_k for the near-field S_k for the LES jet turbulence (Nichols *et al.*, 2013) supports this further, so it is not expected to be just a function of the planar, temporally developing configuration we consider. In figure 4.10, the near-field S_k of the jet turbulence from Nichols *et al.* (2013) is an average between $1 < x/D_j < 10$ of the data they report in figure 10.

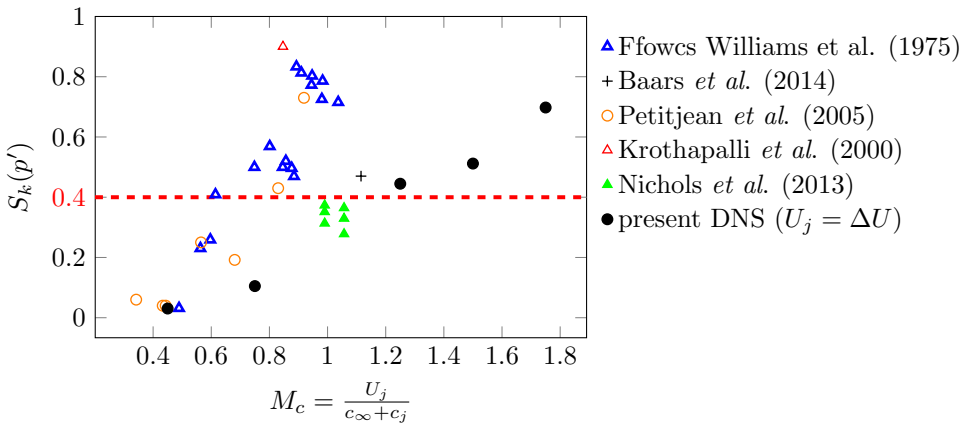

Figure 4.10: Pressure skewness with M_c.

These observations, however, do not preclude the possibility that there is also an effect of geometry. This field has a structure, with different levels of p'_{rms} and different S_k depending upon location and angle, in addition to the distance from the source. This is the case for both laboratory measurements (Gee *et al.*, 2013*a*; Baars *et al.*, 2014) as well as full-scale jet engines (Gee *et al.*, 2013*b*). Hence, no direct one-to-one correspondence is expected.

4.1.4 Reynolds number and numerical dissipation effects

Experiments indicate that crackle is independent of scale (Ffowcs Williams *et al.*, 1975; Mora *et al.*, 2013*b*), which suggests that it is insensitive to the Reynolds number. Most of our simulations have $Re_{\delta_m} = 60$. However, in section 3.2, the $M = 2.5$ flow at $Re_{\delta_m^o} = 120$ was used to show Reynolds-number insensitivity of the turbulence statistics. Figure 4.11 shows that the S_k is also Reynolds number insensitive. This comparison also includes a $Re_{\delta_m} = 120$ simulation done on the same lower-resolution mesh as the $Re_{\delta_m} = 60$ cases (see section 3.2) to assess, particularly, the impact of discretization effects on the thinner, shock-wave-like features. Again, only mild sensitivity at most is seen in figure 4.11. We conclude that the S_k is insensitive to both the physical Reynolds number and to any numerical dissipation.

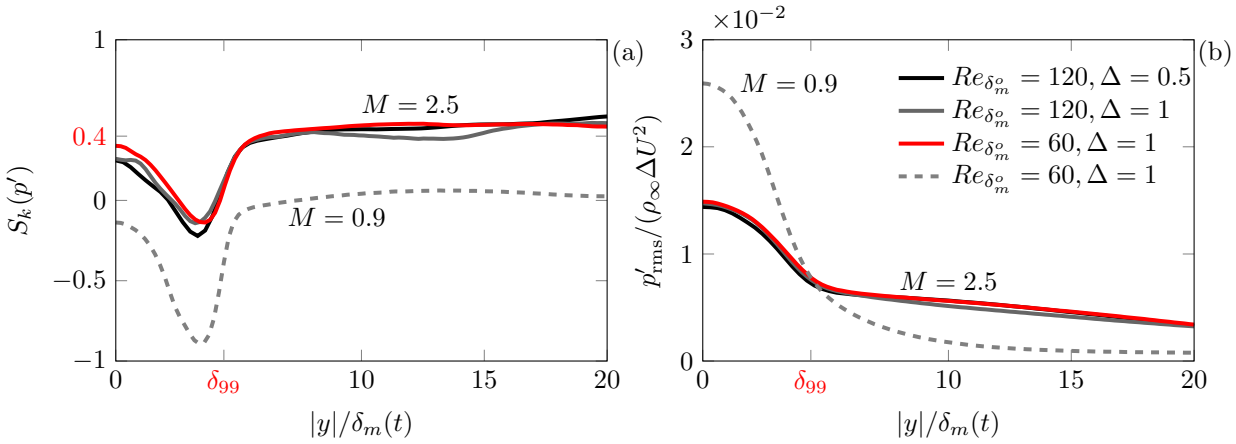

Figure 4.11: Reynolds number effect on the (a) pressure skewness and (b) pressure intensity with distance from the mixing layer at $M = 2.5$. The subsonic $M = 0.9$ is shown for comparison.

Because it would seem that the weak shock-like wave in the sound field might be particularly sensitive to any numerical dissipation, we analyze its effect further. The effect of the filter is examined by varying the frequency that it is applied to the flow solution as described in section 3.2. Figure 4.12 (a) shows that the S_k trend and magnitude is insensitive to the scheduling of the filter. The average pressure intensity in (b) is also unchanged. In section 3.2, the energy spectra show that the different filter frequencies only impact the high-wavenumber scales of the turbulence, and its effect it more pronounced to more frequent filter applications. These results show that S_k is insensitive to numerical filter, but they also indicate that crackle is insensitive to the small-scale details in the turbulence.

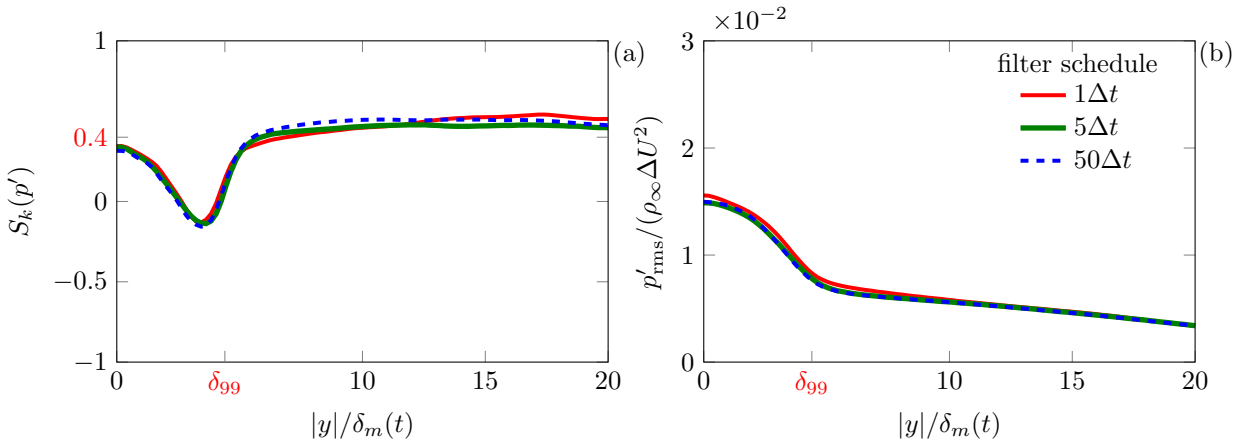

Figure 4.12: Effect of the numerical filter on the (a) pressure skewness and (b) pressure intensity with distance from the mixing layer at $M = 2.5$.

4.1.5 Domain and grid effects

Section 3.3 described the computational domains and grids used to assess their corresponding effect on the turbulence statistics. In particular, it was shown that the two-point correlations decayed rapidly relative to the domain size, suggesting that the computational box was not constraining the turbulence. In figure 4.13, the pressure statistics are also domain size insensitive.

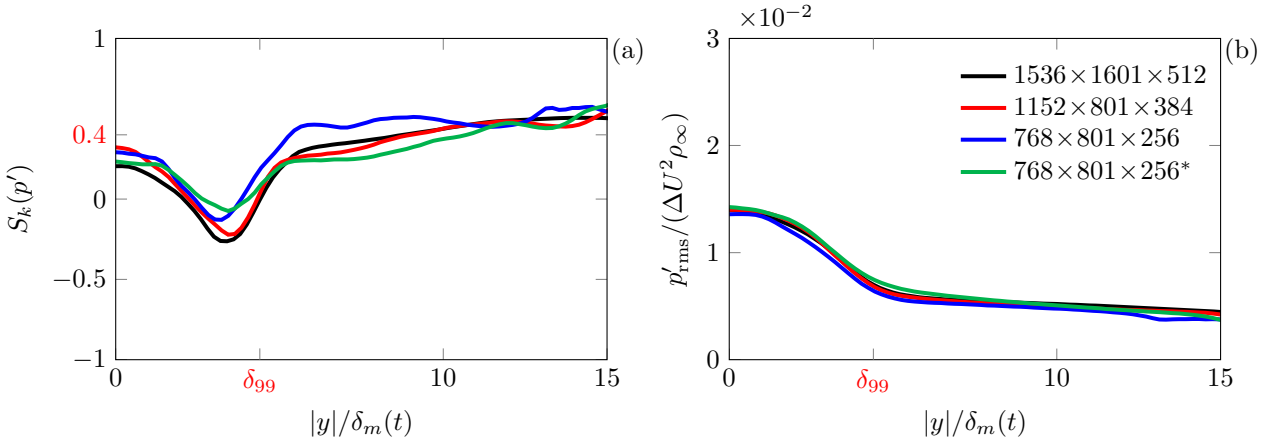

Figure 4.13: Effect of domain size on (a) pressure skewness and (b) pressure intensity with distance from the mixing layer at $M = 2.5$. The meshes summarized in table 3.1.

4.1.6 Effect of initial condition

The initial condition of Kleinman & Freund (2008) that was used to perturb the shear layer depends on a random seed, which generates a different realization of pseudo-random velocity fluctuations. The effect of the initial seed on the pressure statistics is assessed by running the $M = 2.5$ flow two more times. Figure

4.14 shows that the pressure statistics are insensitive to the realization of the initial condition and to the averaging of multiple sets of realizations.

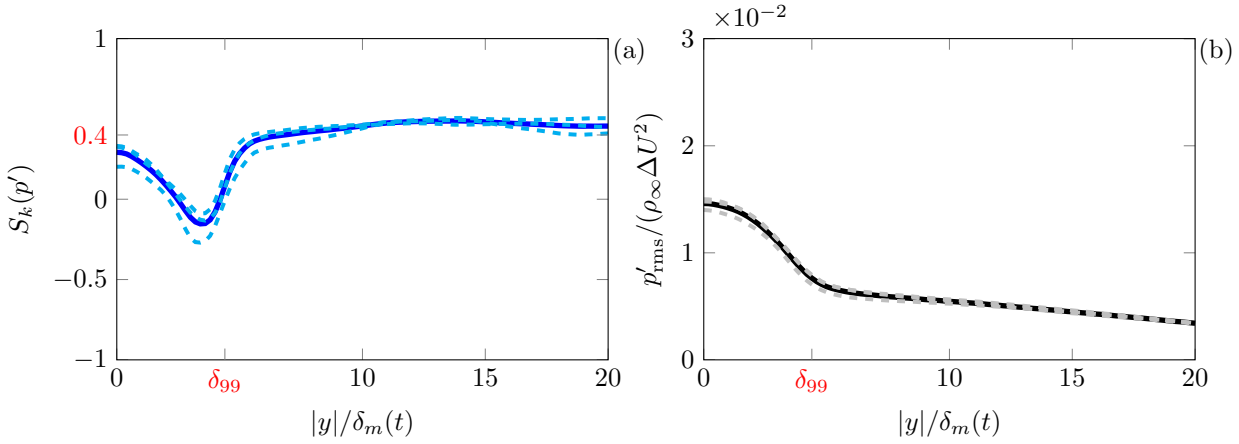

Figure 4.14: Effect of the initial condition on (a) pressure skewness and (b) pressure intensity with distance from the mixing layer at $M = 2.5$: (dashed) three different seeds and (solid) average.

4.2 Visualization

4.2.1 Mach-wave-like radiation

Figure 4.15 compares the instantaneous x-y planes of the different cases, for a late time in their evolution, when $\delta = 32\,\delta_m^o$. For the subsonic flow in figure 4.15 (a), there are no obvious directional waves. For $M \geq 2.5$, the sound field has distinct, shock-like-wave features oriented more parallel to the sheared flow for higher shear rates. At the $M = 1.5$ speed, no sharp waves are obvious, but the waves in figure 4.15 (b) and the pressure fluctuations in figure 4.16 (b) still show a dominant Mach-angle-like direction. The apparent angles agrees with the

$$\theta = \sin^{-1}\left(\frac{2c_\infty}{\Delta U + 1}\right), \tag{4.4}$$

which was presented as a useful relation in regard to source advection speed by Oertel (1979). More detailed analysis of the wave angle statistics are provided in section 4.3.

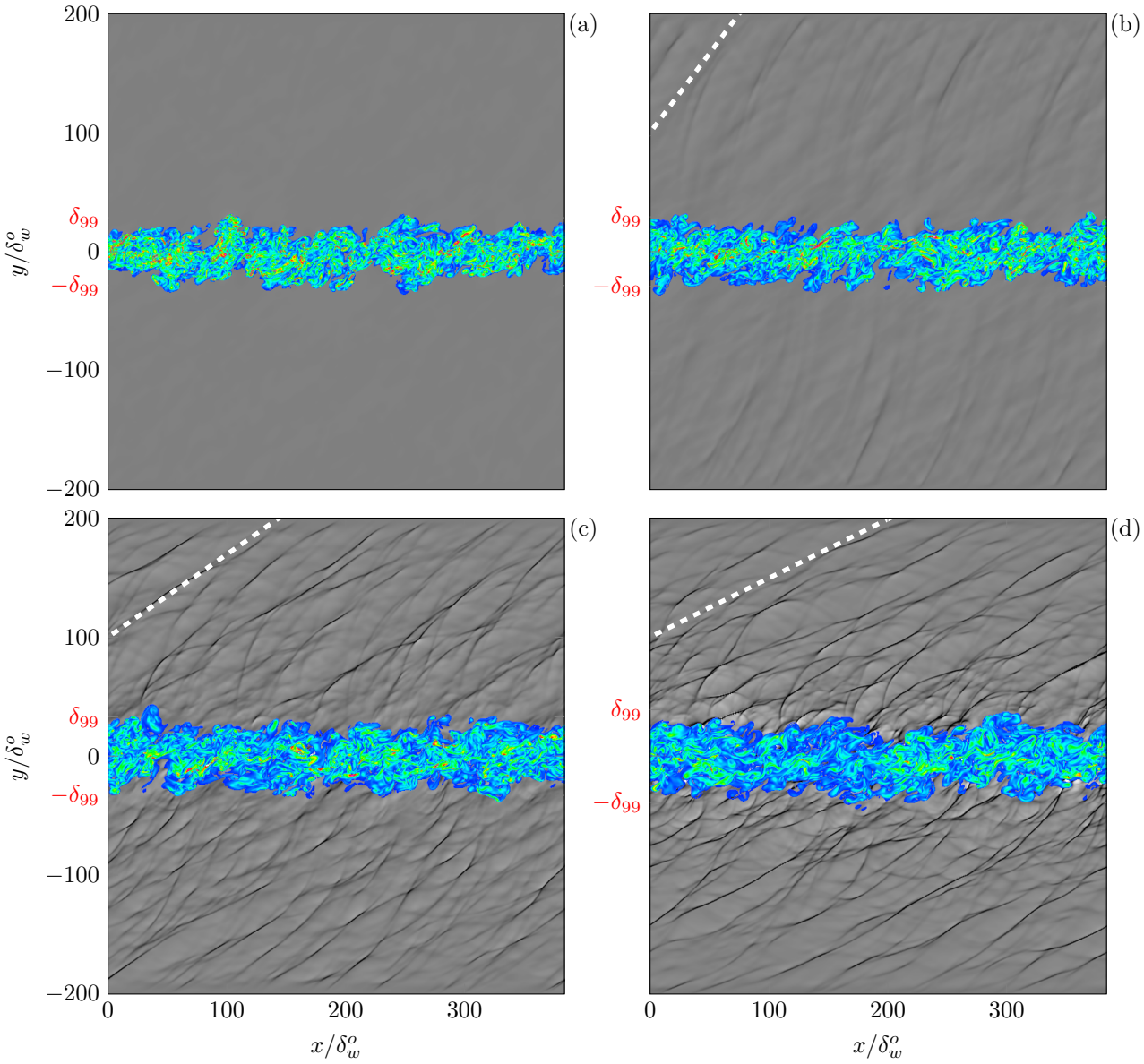

Figure 4.15: Two-dimensional plane of vorticity magnitude in color scale from $0 < |\nabla \times \mathbf{u}| \cdot \delta_m/\Delta U < 5$ and dilatation in gray scale from $-0.01 < \nabla \cdot \mathbf{u} \cdot \delta_m/\Delta U < 0.01$ at $z = L_z/2$ when $\delta_m/\delta_m^o = 32$ for (a) $M = 0.9$, (b) 1.5, (c) 2.5, and (d) 3.5. The dashed lines in (b)–(d) correspond to the Mach line orientation in (6.18).

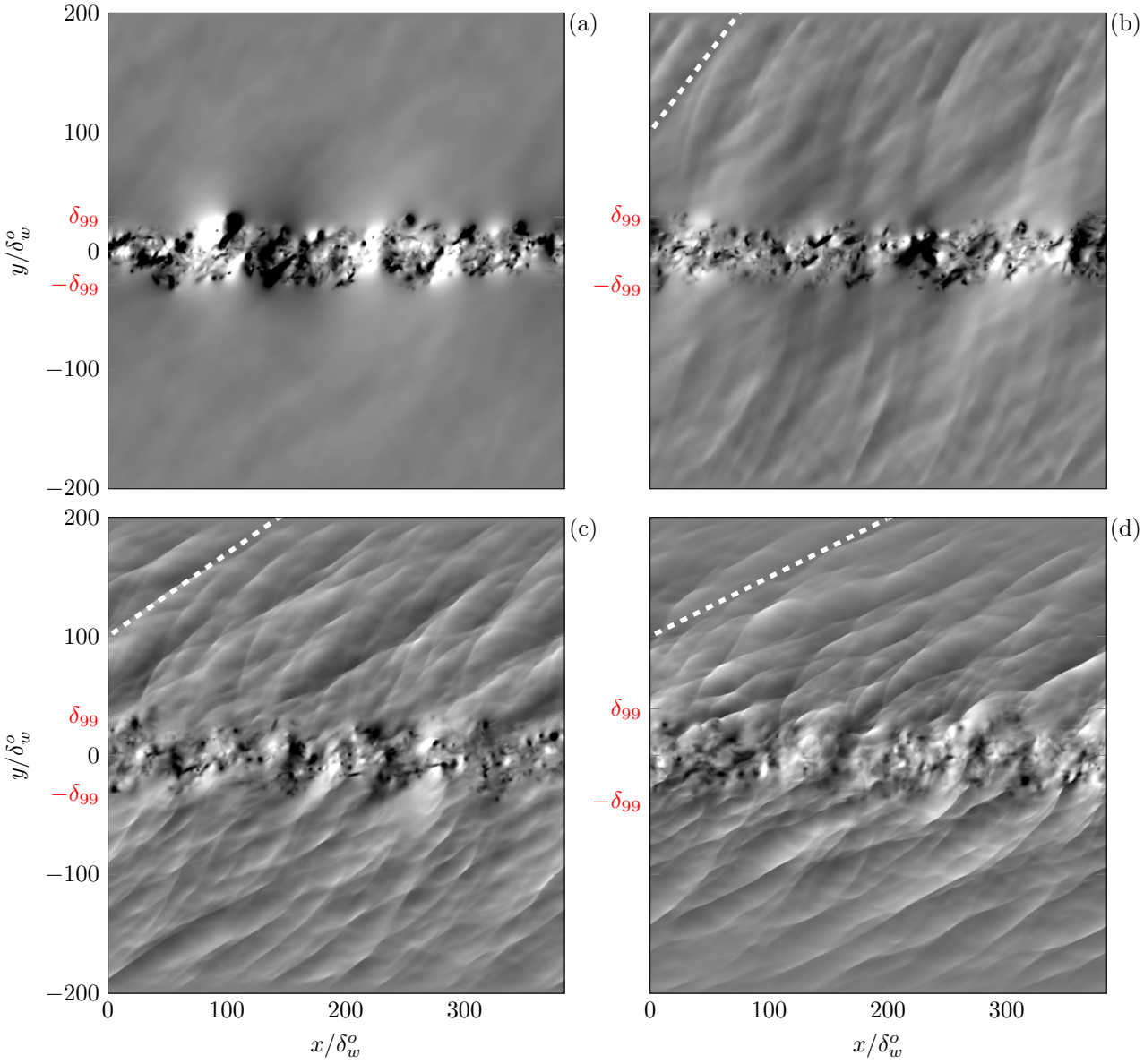

Figure 4.16: Two-dimensional plane of p'-fluctuations $-0.025 < p'/(c_\infty \Delta U^2) < 0.025$ at $z = L_z/2$ when $\delta_m/\delta_m^o = 32$ for (a) $M = 0.9$, (b) 1.5, (c) 2.5, and (d) 3.5. The dashed lines in (b)–(d) correspond to the Mach line orientation in (6.18).

4.2.2 Three-dimensional near field

Figures 4.17 show the in-plane dilatation and pressure fields have a complex, three-dimensional structure, much more so than might be expected when viewed from the side. The pressure waves form curved shock-like regions with obvious wave intersections. These structures are reminiscent of the three-dimensionality observed with acetone PLIF (planar laser-induced fluorescence) near supersonic planar shear layers (Rossmann *et al.*, 2002). Also, when viewed from 'above' in figure 4.18 in the streamwise x-direction, the dilatation fields are composed an array of thin, curved shock-like waves that crisscross with each other. The pressure fields are three-dimensional and appear to have stronger compressions where waves come together. These interactions have the potential to elevate pressure skewness, and their overall statistical effect will be examined in chapter 5 with a complete skewness transport budget.

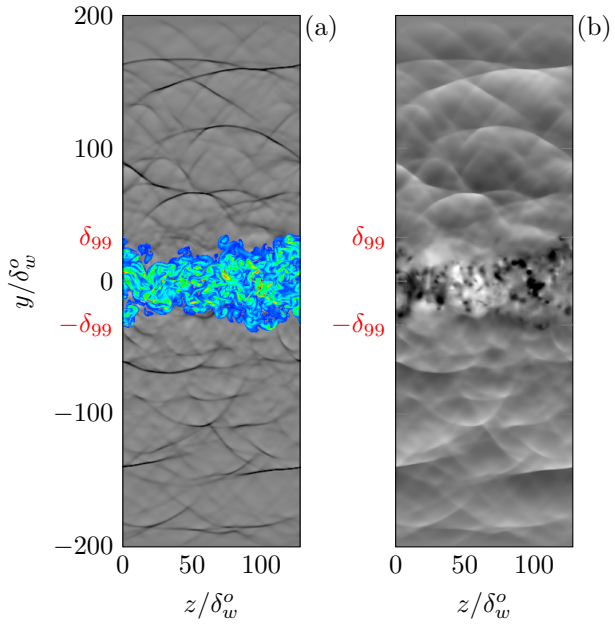

Figure 4.17: Visualized (a) vorticity (color) and dilatation (gray scale) and (b) p'-fluctuation at $x = L_x/2$ for $M = 2.5$. The colormaps match those of figures 4.15 and 4.16.

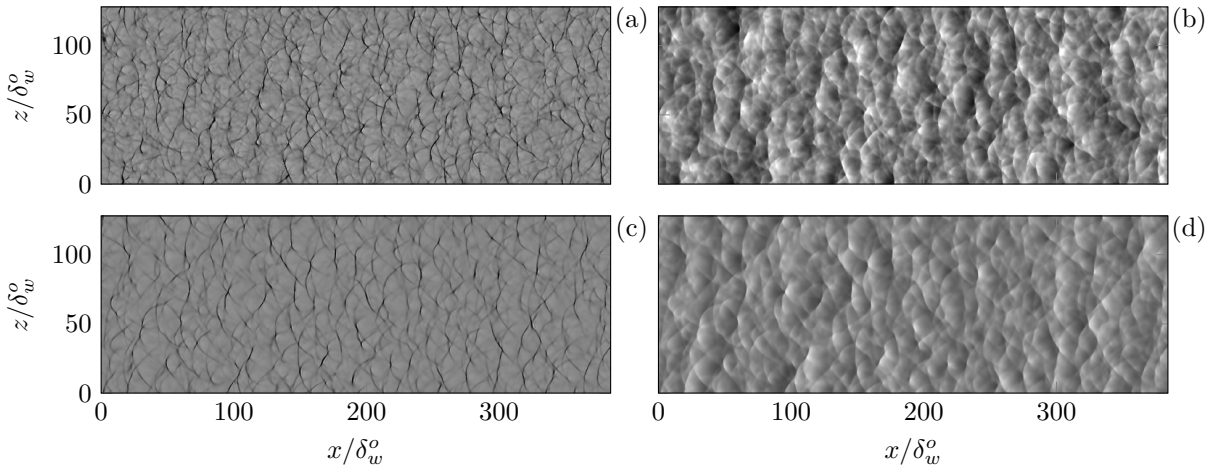

Figure 4.18: $M = 2.5$, x-z plane of (a), (c) dilatation and (b), (d) p'-fluctuation when $\delta_m/\delta_m^o = 10$. (a),(b) and (c),(d) correspond to planes above the turbulence at $y = 7.5\,\delta_m$ and $15\,\delta_m$, respectively. The colormaps match those of figures 4.15 and 4.16.

4.2.3 Wave merging

As mentioned in section 4.1.1, the increase in pressure intensity with M indicates the potential for any sound nonlinearity. In figure 4.19, the evolution of waves at discrete times ($\Delta t = 64\delta_m^o/c_\infty$) show a particular wave merging event, which is fundamentally a nonlinear phenomenon since linear waves would simply superpose. Section 4.4 quantifies the effect of this nonlinearity by counting the strong compressions above the mixing layer.

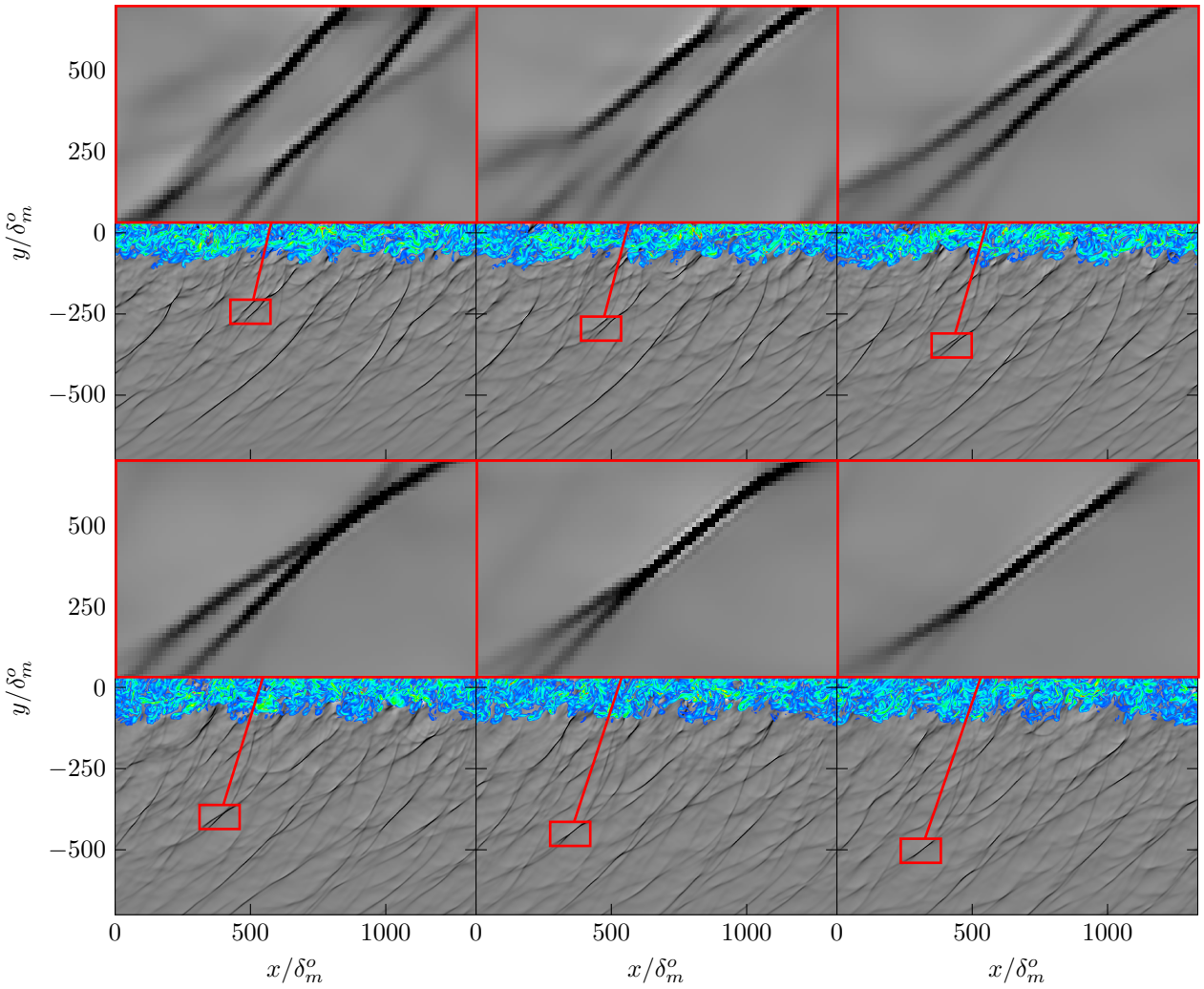

Figure 4.19: Visualizations of merging wave fronts for $M = 2.5$ when $\delta_m(t)/\delta_m^o = 15$ to 25 at $z = L_z/2$: colormaps of $|\nabla \times \mathbf{u}|$ between 0.1 and $5\Delta U/\delta_m(t)$ with gray-scale levels of $\nabla \cdot \mathbf{u}$ between $\pm 0.5\Delta U/\delta_m(t)$.

4.3 Angle of the compressive waves

The visualizations in the previous section showed an array of waves radiating from the turbulence, and although they appear to radiate close to a preferred direction, waves with different velocities (and angles) are seen to intersect and merge nonlinearly, which has implications on the sound mechanics of crackle. We examine the evolving distribution of wave orientations beyond the turbulence by measuring the wave angle from the flow solution. Figure 4.20 shows how the wave angles at each mesh point in the near acoustic field is extracted. Strong compression waves are marked based dilatation threshold

$$\nabla \cdot \mathbf{u} < d_c, \tag{4.5}$$

and the angle with respect to the streamwise direction is then

$$\theta = \cos^{-1} n_y, \tag{4.6}$$

where n_y is the y-component of the normal vector computed from the gradient of the pressure field

$$\mathbf{n} = \frac{\nabla p}{|\nabla p|}. \tag{4.7}$$

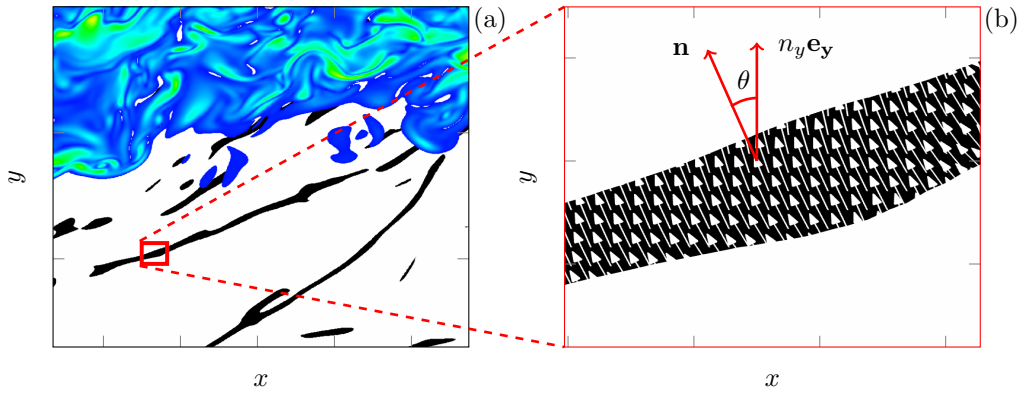

Figure 4.20: (a) View in the near field with $\nabla \cdot \mathbf{u} < -0.0125 \Delta U/\delta_m(t)$ (black) with vorticity magnitude (color) between $|\nabla \times \mathbf{u}| = 0.1$ and $5\,\Delta U/\delta_m(t)$. (b) Detailed view of the wavefront with normal vectors shown at each computational grid point where (4.5) is satisfied.

Averaging over the periodic x- and z-directions and in time, as was done for other turbulence quantities discussed in chapter 3, yields the data of figures 4.21–4.23 (b) for the average wave angle for $M = 1.5$, 2.5 and 3.5. The statistics from the $M = 0.9$ case are omitted because the near field did not have sufficiently strong compressions for the range of dilatation thresholds considered to have converged statistics. The DNS results support the eddy advection hypothesis with $\langle\theta\rangle = 55°$, 34°, and 27° at $y = 15\,\delta_m(t)$ for $M = 1.5$, 2.5, and 3.5, respectively. The expected wave orientation corresponding to empirical relation of Oertel (1979)

$$\theta = \sin^{-1}\left(\frac{2c_\infty}{\Delta U + 1}\right), \tag{4.8}$$

is $\theta = 53°$, 35°, and 27° for $\Delta U = 1.5$, 2.5, 3.5, respectively. Of course, the turbulence does not have a single, fixed advection speed. Thus, we quantify the range of the wave angles by the standard deviation bounds in figures 4.21–4.23. We observe smaller standard deviations about the mean for slower speeds. For $M = 3.5$, in particular, the range of angles decreases with distance from the mixing layer. This would be

consistent with increased geometric flattening and merging of different waves due to weak-shock propagation nonlinearity (Whitham, 1974).

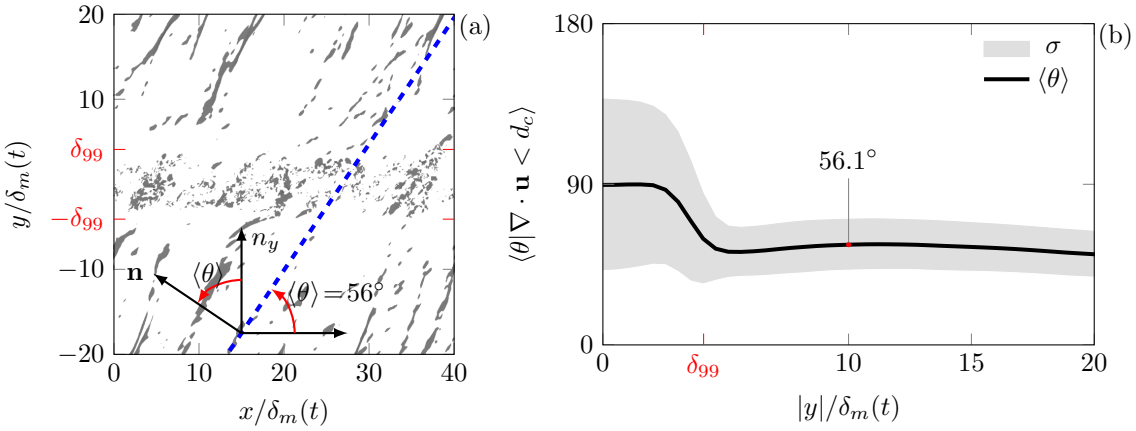

Figure 4.21: $M = 1.5$: (a) Dilatation, $(\nabla\cdot\mathbf{u})\delta_m(t)/\Delta U < -0.0125$, when $\delta_m(t)/\delta_m^o = 32.8$ at $z = L_z/2$. (b) Average wave angles $\langle\theta\rangle$ conditioned on $(\nabla\cdot\mathbf{u})\delta_m(t)/\Delta U < d_c = -0.0125$ shaded by one standard deviation (σ) about the mean.

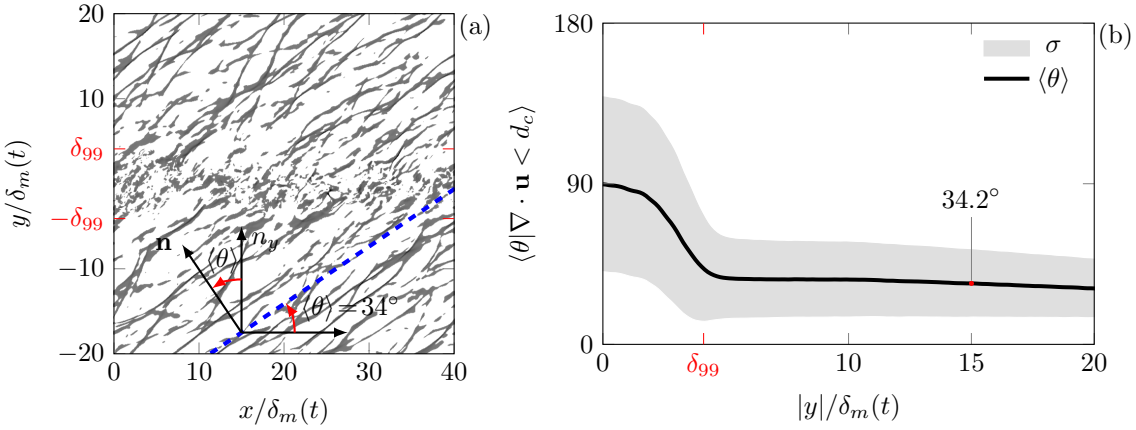

Figure 4.22: $M = 2.5$: (a) Dilatation, $(\nabla\cdot\mathbf{u})\delta_m(t)/\Delta U < -0.0125$, when $\delta_m(t)/\delta_m^o = 32.8$ at $z = L_z/2$. (b) Average wave angles $\langle\theta\rangle$ conditioned on $(\nabla\cdot\mathbf{u})\delta_m(t)/\Delta U < d_c - 0.0125$ shaded by one standard deviation (σ) about the mean.

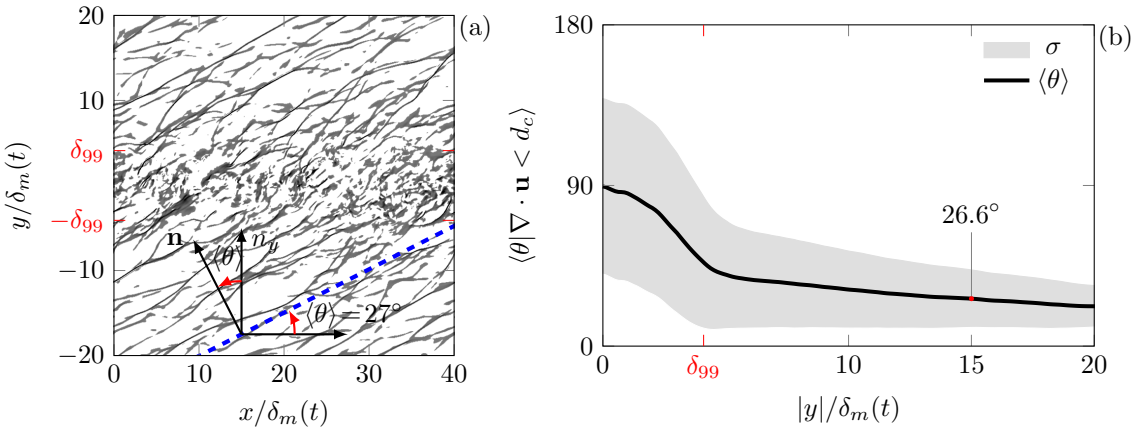

Figure 4.23: $M = 3.5$: (a) Dilatation, $(\nabla\cdot\mathbf{u})\delta_m(t)/\Delta U < -0.0125$, when $\delta_m(t)/\delta_m^o = 32.8$ at $z = L_z/2$. (b) Average wave angles $\langle\theta\rangle$ conditioned on $(\nabla\cdot\mathbf{u})\delta_m(t)/\Delta U < d_c - 0.0125$ shaded by one standard deviation (σ) about the mean.

We now examine the effect of this threshold by varying d_c over an order of magnitude between $d_c = -10^{-1}\,\delta_m(t)/\Delta U$ and $-10^{-2.5}\,\delta_m(t)/\Delta U$. Figure 4.24 (b)–(c) shows that for decreasing d_c (including fewer of the strongest waves), the wave angle statistics appear to converge, meaning that the angle of the strongest waves dominate the average value. For $M = 1.5$, the trend with distance seems to diverge slightly. This effect is due to the decrease in the number counted waves (shown in figure 4.27), which impacts the convergence of this average quantity.

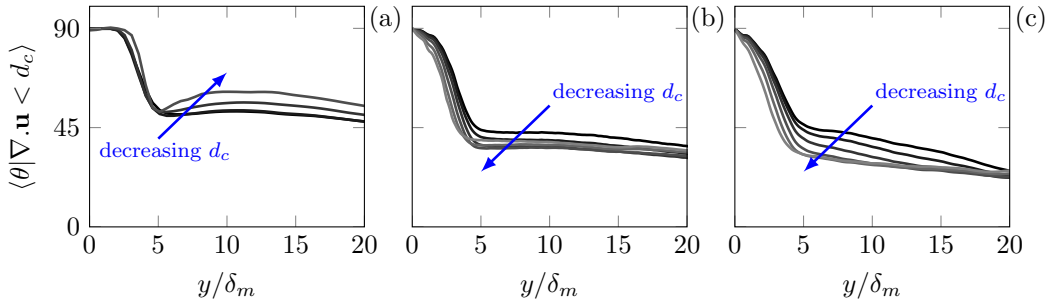

Figure 4.24: Effect of the dilatation threshold (d_c) on the average wave angle for (a) $M = 1.5$, (b) 2.5, and (c) 3.5. The values of d_c range between $d_c = -0.0125$ to -3×10^{-3}.

4.4 Wave merging: the number of distinct waves

Cumulative nonlinear propagation effects are anticipated to reduce the number of distinct waves (Lighthill, 1956). Described as 'wave-bunching', stronger shocks with a higher propagation velocity will 'consume'

weaker, more slowly propagating ones (Lighthill, 1956, 1993). Recent measurements also suggest the existence of wave merging phenomenon (Fiévet *et al.*, 2015) though no correlation with S_k was measured.

We count the number of distinct waves directly by summing the number of compression regions at a fixed y-position that satisfy the dilatation threshold (4.5) as shown in figure 4.25.

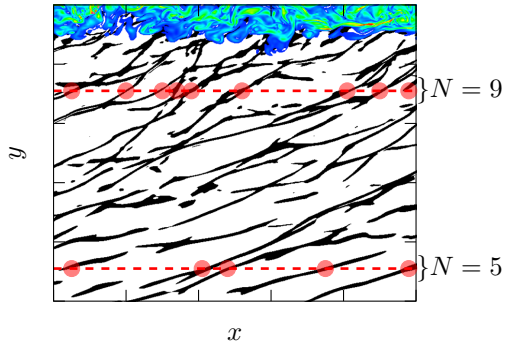

Figure 4.25: View in the near field with $\nabla \cdot \mathbf{u} < -0.0125\Delta U/\delta_m(t)$ (black) with vorticity magnitude (color) between $|\nabla \times \mathbf{u}| = 0.1$ and $5\,\Delta U/\delta_m(t)$.

The average number of waves with distance from the mixing layer is shown in 4.26. We see a different evolution of wave density between the $M = 1.5$ and the nominally crackling cases, $M = 2.5$ and 3.5. The wave density increases for $M = 1.5$ because at earlier times the smaller scales of the turbulence produce more compression waves. At larger y, these shorter waves (and higher frequencies) persist. Nonlinear merging counters this behavior. For $M = 2.5$ and 3.5, the nonlinear merging effect dominates, and the number of waves decreases with distance from the mixing layer.

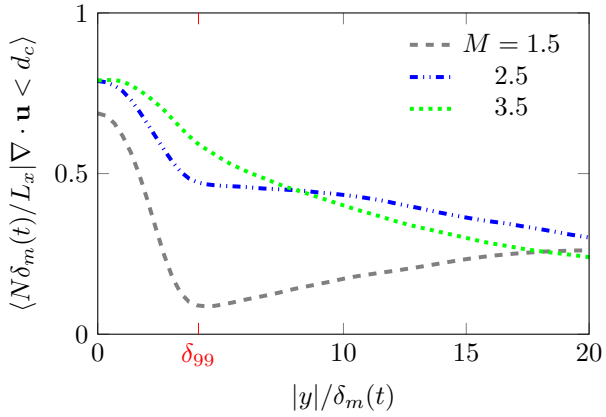

Figure 4.26: Average number of waves conditioned on $(\nabla \cdot \mathbf{u})\delta_m(t)/\Delta U < d_c = -0.0125$.

Compressions that exceed a specified threshold in (4.5) are included in this statistical assessment, and we examine the effect of this threshold by varying d_c over an order of magnitude between $d_c = -10^{-1}$ and $-10^{-2.5}\,\delta_m(t)/\Delta U$ as done in section 4.3. Decreasing the threshold leads to a decrease in the average wave density shown in figure 4.27. This decrease is reflected by a downward shift of the $N\delta_m/L_x$ curves where fewer of the strongest waves are being counted, though the general trend with distance remains unchanged. The conclusion is insensitive despite changing the dilatation threshold by an order of magnitude: the wave density decreases with range for $M \gtrsim 2.5$ by over 50% between $y = 5\,\delta_m$ to $20\,\delta_m$.

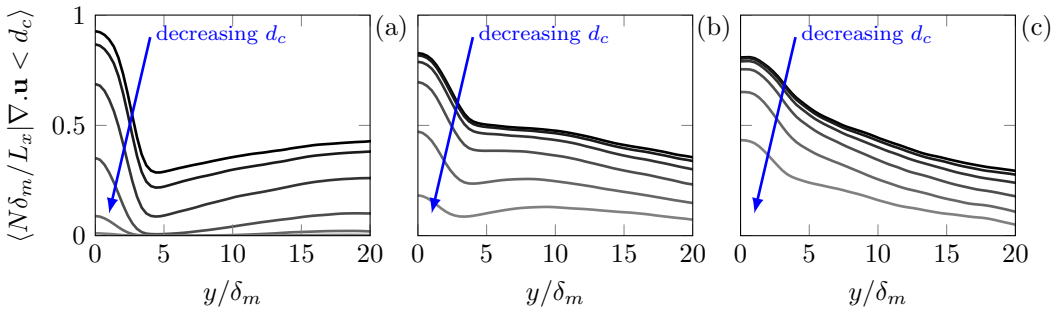

Figure 4.27: Effect of the dilatation threshold (d_c) on the average number of waves for (a) $M = 1.5$, (b) 2.5, and (c) 3.5. The values of d_c range between $d_c = -0.0125$ to -3×10^{-3}.

Chapter 5

Pressure Skewness Transport

One approach to examine the workings of turbulence is to examine the equations governing its statistics. The budget of turbulence kinetic energy transport can, for example, be used to explain the production, transport, and dissipation of turbulence and is therefore useful in turbulence modeling. We take a similar approach to identifying the factors that affect S_k by developing and evaluating a S_k transport equation. We show that sources of skewness are found near the turbulence for $M \geq 2.5$ to be dominated by two correlations: $\overline{(p')^3 d'}$ and $\frac{\partial \overline{v'(p')^3}}{\partial y}$, where $d' = \nabla \cdot \mathbf{u}'$. These sources of S_k are countered by a viscous, heat conduction factor which dominates the entropy production.

5.1 Pressure skewness transport equation

We start with the product-rule differentiation of pressure skewness advection

$$\frac{\overline{D}}{Dt} S_k(p') \equiv \frac{\overline{D}}{Dt}\left[\frac{\overline{(p')}^3}{\overline{(p')^2}^{3/2}}\right] = \left[\overline{(p')^2}\right]^{-3/2}\left\{\frac{\overline{D}}{Dt}\overline{(p')^3} - \frac{3}{2}\frac{\overline{(p')^3}}{\overline{(p')^2}}\frac{\overline{D}}{Dt}\overline{(p')^2}\right\}, \tag{5.1}$$

where

$$\frac{\overline{D}}{Dt}() \equiv \frac{\partial}{\partial t} + \overline{v}\frac{\partial}{\partial y}, \tag{5.2}$$

has only a y-advection component since the turbulence is statistically homogeneous in the x- and z-directions, though we anticipate this too to be small. Evaluation of (5.1) is based on evolution equations for both the two more fundamental correlations, $\overline{(p')^3}$ and $\overline{(p')^2}$. To derive these, we begin with the equation for pressure

$$\frac{\partial p}{\partial t} = -u_i\frac{\partial p}{\partial x_i} - \gamma p\frac{\partial u_i}{\partial x_i} + \mathcal{D}, \tag{5.3}$$

where the heat conduction and viscous terms are combined in

$$\mathcal{D} = (\gamma - 1)\left\{ \frac{1}{RePr}\frac{\partial^2 T}{\partial x_i \partial x_i} + \tau_{ij}\frac{\partial u_i}{\partial x_j} \right\}. \tag{5.4}$$

The viscous stress tensor τ_{ij} is as (2.6). Substituting the Reynolds decomposed pressure and velocity,

$$p = \overline{p} + p' \tag{5.5}$$

$$u_i = \overline{u}_i + u_i', \tag{5.6}$$

into (5.3) and averaging yields the mean pressure equation

$$\frac{\partial \overline{p}}{\partial t} + \overline{u_i}\frac{\partial \overline{p}}{\partial x_i} + \overline{u_i'\frac{\partial p'}{\partial x_i}} = -\gamma\left[\overline{p}\frac{\partial \overline{u_i}}{\partial x_i} + \overline{p'\frac{\partial u_i'}{\partial x_i}}\right] + \overline{\mathcal{D}}. \tag{5.7}$$

The time rate-of-change of pressure fluctuations is

$$\frac{\partial p'}{\partial t} = \frac{\partial p}{\partial t} - \frac{\partial \overline{p}}{\partial t}, \tag{5.8}$$

and substituting in (5.3) and (5.7) in the right side of (5.8) gives

$$\frac{\partial p'}{\partial t} = -\overline{u_i}\frac{\partial p'}{\partial x_i} - u_i'\frac{\partial \overline{p}}{\partial x_i} - u_i'\frac{\partial p'}{\partial x_i} + \overline{u_i'\frac{\partial p'}{\partial x_i}} - \gamma\left[\overline{p}\frac{\partial u_i'}{\partial x_i} + p'\frac{\partial \overline{u_i}}{\partial x_i} + p'\frac{\partial u_i'}{\partial x_i} - \overline{p'\frac{\partial u_i'}{\partial x_i}}\right] + \mathcal{D}'. \tag{5.9}$$

The fluctuating viscous and heat conduction term in (5.9) is $\mathcal{D}' = \mathcal{D} - \overline{\mathcal{D}}$. Noting the chain-rule relationship

$$\frac{\partial \overline{(p')^3}}{\partial t} = \overline{3(p')^2\frac{\partial p'}{\partial t}}, \tag{5.10}$$

the first term on the right side of (5.1) along with (5.9) and (5.10) gives

$$\left[\overline{(p')^2}\right]^{-3/2}\frac{\overline{D}}{Dt}\overline{(p')^3} = \left[\overline{(p')^2}\right]^{-3/2}\times$$

$$\begin{aligned}
&\Bigg[-3\overline{v'(p')^2}\frac{\partial \overline{p}}{\partial y} && \text{(Ia)}\\
&-\overline{\frac{\partial v'(p')^3}{\partial y}} && \text{(IIa)}\\
&+3\overline{(p')^2}\overline{u_i'\frac{\partial p'}{\partial x_i}} && \text{(IIIa)}\\
&-3\gamma\overline{p}\overline{(p')^2 d'} && \text{(IVa)}\\
&-3\gamma\overline{(p')^3}\frac{\partial \overline{v}}{\partial y} && \text{(Va)}\\
&+(-3\gamma+1)\overline{(p')^3 d'} && \text{(VIa)}\\
&+3\gamma\overline{(p')^2}\cdot\overline{p'd'} && \text{(VIIa)}\\
&+3\overline{(p')^2\mathcal{D}'} \quad \Bigg]. && \text{(VIIIa)}
\end{aligned} \tag{5.11}$$

Similarly, noting the chain-rule relationship for pressure intensity,

$$\overline{\frac{\partial (p')^2}{\partial t}} = \overline{2p'\frac{\partial p'}{\partial t}}, \tag{5.12}$$

the remaining term on the right sides of (5.1) along with (5.9) and (5.12) is

$$-\frac{3}{2}\frac{\overline{(p')^3}}{\overline{(p')^2}^{5/2}}\times\frac{\overline{D}}{Dt}\overline{(p')^2} = -\frac{3}{2}\frac{\overline{(p')^3}}{\overline{(p')^2}^{5/2}}\times$$

$$\begin{aligned}
&\Bigg[-2\overline{v'p'}\frac{\partial \overline{p}}{\partial y} && \text{(Ib)}\\
&-2\overline{p'u_i'\frac{\partial p'}{\partial x_i}} && \text{(IIb)}\\
&-2\gamma\overline{p}\overline{p'd'} && \text{(IIIb)}\\
&-2\gamma\overline{(p')^2}\frac{\partial \overline{v}}{\partial y} && \text{(IVb)}\\
&-2\gamma\overline{(p')^2 d'} && \text{(Vb)}\\
&+2\overline{p'\mathcal{D}'} \quad \Bigg]. && \text{(VIb)}
\end{aligned} \tag{5.13}$$

Together, the right side of (5.11) and (5.13) govern the dynamics of pressure skewness in (5.1). We remark that positive valued sources of pressure intensity in (5.13) are sinks of pressure skewness, which is reflected

by the negative sign in the prefactor in (5.13). This is simply because $\overline{(p')^2}$ appears in the denominator of skewness in (5.1), so increasing $\overline{(p')^2}$ will decrease S_k. The specific terms selected to form (5.11) and (5.13) is not unique but was deemed useful for the following discussion. The next section will evaluate these terms using the DNS data and consider some specific combinations in some cases.

5.2 Results

Figure 5.1 shows the factors governing $S_k(p')$ on the right side of (5.11) and (5.13). Terms Va and IVb have been combined since they represent the transport of S_k with $d\overline{v}/dy$. Terms VIIIa and VIb are also combined to represent all of the molecular effects on S_k. For $M \gtrsim 2.5$, above the mixing layer ($|y| > \delta_{99}$), two principle factors diminish skewness in this region: molecular effects (terms VIIIa and VIb) and the pressure-dilatation correlation (term IIIb). Terms IIa, IVa and VIa represent the largest contributors to S_k, where IIa and VIa would otherwise be zero in the linearized version of (5.9).

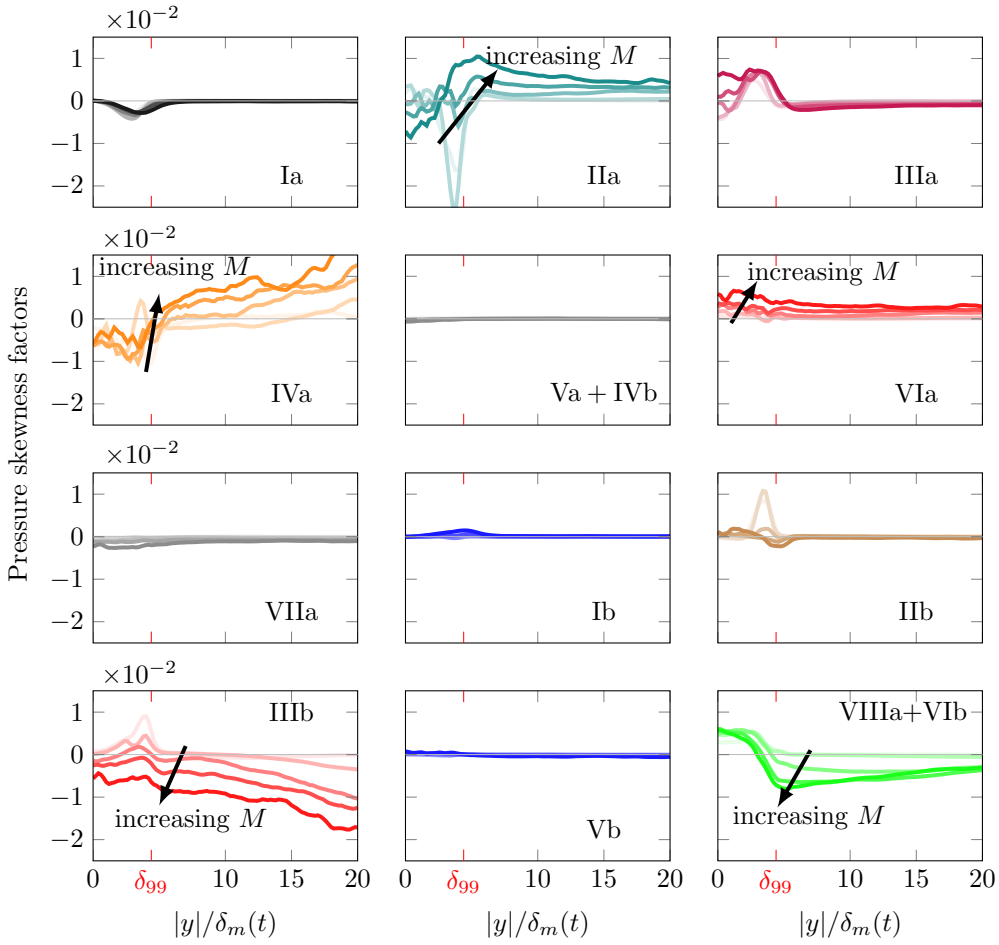

Figure 5.1: Pressure skewness factors from the right side of (5.11) and (5.13) for $M = 0.9$ to 3.5.

From figure 5.1, the terms IVa and IIIb added together

$$\underbrace{-3\gamma\overline{p}\overline{(p')^2 d'}\cdot\overline{(p')^2}^{-3/2}}_{\text{IVa}}+\underbrace{3\gamma\overline{p}\cdot\overline{p'd'}\cdot\overline{(p')^3}\cdot\overline{(p')^2}^{-5/2}}_{\text{IIIb}} \tag{5.14}$$

are insignificant contributors to S_k change. This can be anticipated from weak shock relations. The pressure increase across a weak, viscous shock is (Thompson, 1988)

$$p' \propto -\rho_\infty c_\infty^2 \frac{l_s d'}{2U_\infty}, \tag{5.15}$$

where l_s is a measure of the shock thickness. With (5.15), the terms IVa and IIIb in (5.14) cancel. Their sum from the DNS is shown in figure 5.2, and it is indeed significantly smaller than their individual contribution (see terms IVa and IIIb in figure 5.1). Thus, the pressure-squared dilatation (IVa) and pressure-dilatation correlation (IIIb), cancel in the weak-shock limit, which seems to exist for $|y|/\delta_m \gtrsim \delta_{99}$. (The convergence of this statistic, in particular for $M = 2.5$, is assessed in section 5.2.5, figure 5.8.)

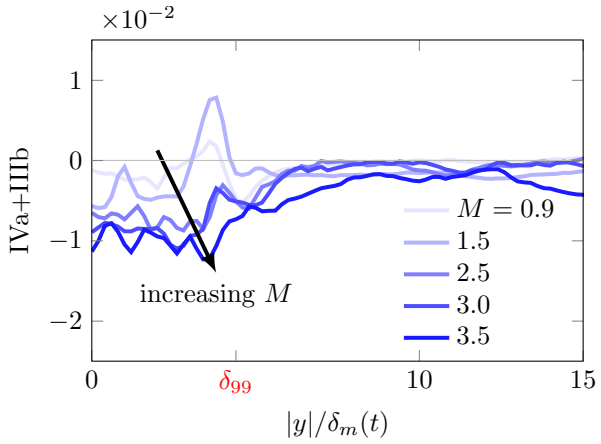

Figure 5.2: The sum of terms IVa and IIIb in (5.14).

5.2.1 Total transport of skewness

Figure 5.3 shows the total transport of pressure skewness for all the M cases. There is no clear Mach number dependence despite the distinct sound fields of $M \gtrsim 2.5$ having sharp, shock-like waves (see figure 4.15). The wiggles suggest it is also poorly converged, which is examined further in section 5.2.5. For $|y| \gtrsim \delta_{99}$, the skewness is essentially unchanged, $\overline{D}/Dt(S_k) \approx 0$, which is consistent with the present observations that S_k is also constant above the mixing layer (see figure 4.6) and that it varies at most slowly in the sound field from jets at similar flow conditions (see section 4.1.3 and references therein). Considering the self-similar

coordinate, $\eta = y/\delta_m$, yields

$$\left[\overline{v} - \eta\dot{\delta}_m\right] \frac{1}{\delta_m}\frac{\partial}{\partial\eta}S_k(\eta), \tag{5.16}$$

with the corresponding shear layer growth rate, $\dot{\delta}_m$. From this perspective, the value of (5.16) is essentially zero at $y = 0$, and the departure from this in figure 5.3 provides a measure of small deviation from strict self-similarity.

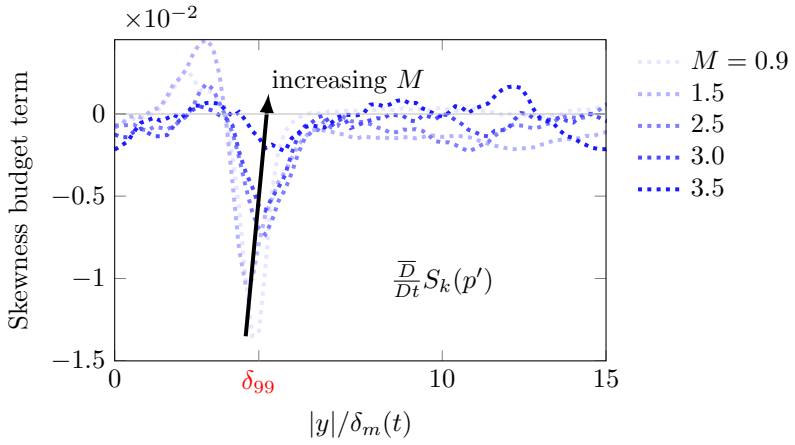

Figure 5.3: Total transport of pressure skewness with distance from the mixing layer.

5.2.2 Pressure-cubed dilatation correlation (term VIa)

Figure 5.4 shows that the pressure-cubed dilatation is a source of skewness at all y, and its effect increases with M. The $\overline{(p')^3 d'}$ correlation shares the same sign as pressure dilatation, but this correlation is weighted by more extreme pressure events via the cube exponent. This result suggests that the near field contains relatively extreme positive pressure events correlated to negative fluctuating dilatation (d'). Again using the weak-shock relation (5.15), this term can be anticipated to be positive with

$$\text{VIa} \propto (3\gamma - 1) l_s \overline{(p')^4} > 0, \tag{5.17}$$

which also supports a weak-shock description of the dynamics here.

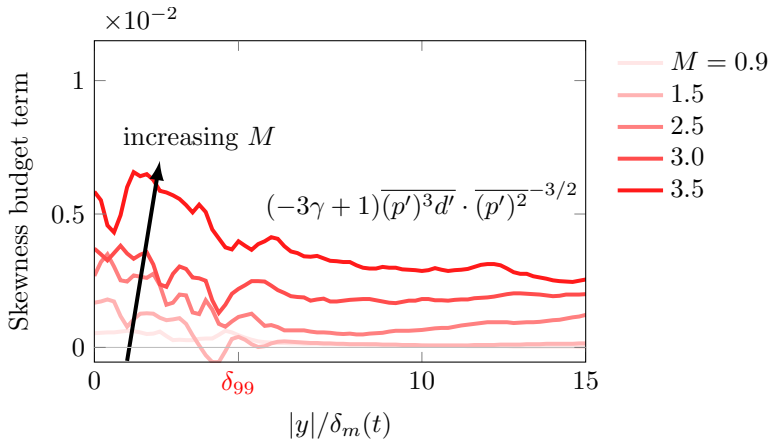

Figure 5.4: Pressure-cubed dilatation from term VIa in (5.11) with distance from the mixing layer.

5.2.3 Fluctuation driven correlated transport (term IIa)

In figure 5.5, the IIa term in (5.11) increases S_k beyond $|y|/\delta_m \gtrsim \delta_{99}$, and its strength increases with M. We note that this factor comes from a perturbation-squared term in (5.9), so it represents nonlinear interactions above the mixing layer. It is also fundamentally multidimensional; it would be zero for one-dimensional propagation, say in a periodic domain.

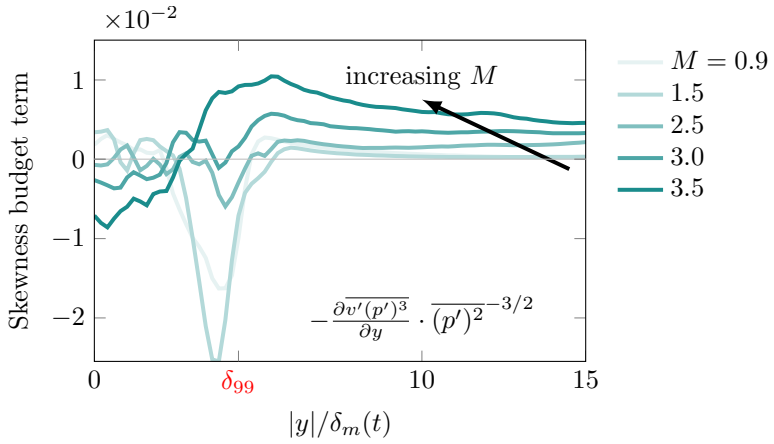

Figure 5.5: Fluctuation driven transport of $(p')^3$ from term IIa in (5.11) with distance from the mixing layer.

5.2.4 Molecular effect (terms VIIIa & VIb)

The two sources of skewness we consider in section 5.2.2 and 5.2.3, which are active beyond the mixing layer $|y|/\delta_m \gtrsim \delta_{99}$, are countered by the molecular effects (terms VIIIa and VIb) as shown in figure 5.6. For $M \geq 2.5$ this region has thin, shock-like waves (see figure 4.15), and we expect viscous and heat conduction effects to be significant there since weak viscous shocks waves arise from a balance between convective

steepening and diffusion effects (Taylor, 1910; Lighthill, 1956).

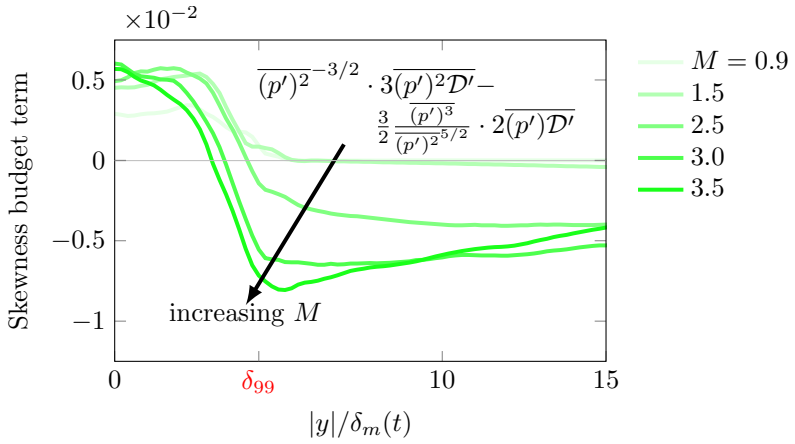

Figure 5.6: Molecular effects on the transport of pressure skewness.

5.2.5 Assessing the statistical convergence of the S_k budget terms

The wiggles in the curves in figure 5.1 and 5.3 suggest poor convergence of the statistics, which leads to the question whether or not our conclusions are indeed insensitive to the statistical sample. To assess this, the $M = 2.5$ flow is simulated two more times with different initial conditions of the velocity fluctuations. Figure 5.7 shows the largest terms transporting S_k. The sum of terms IVa and IIIb in (5.14) are shown in figure 5.8. The average of the three $M = 2.5$ simulations smooths the wiggles, but the conclusion is unchanged. Last, we show residual by subtracting the left and right side of (5.11) and (5.13) which is shown in figure 5.9.

5.2.6 Conclusions

As anticipated, the skewness transport is unchanged for $y/\delta_m \gtrsim \delta_{99}$ which is consistent with observations of S_k above the mixing layers. The effects of two terms, the pressure-squared dilatation (term IVa) and pressure-dilatation correlation (term IIIb), cancel above $y/\delta_m \gtrsim \delta_{99}$, which is supported by the expected weak-shock behavior. Two nonlinear terms, pressure-cubed dilatation (term VIa) and fluctuation-driven transport of $(p')^3$ (term IIa), are countered by molecular effects (terms VIIIa and VIb) above $y/\delta_m \gtrsim \delta_{99}$. The convergence of these statistics is assessed with three additional $M = 2.5$ simulations using different seeds to generate the initial condition; the conclusions are insensitive to this.

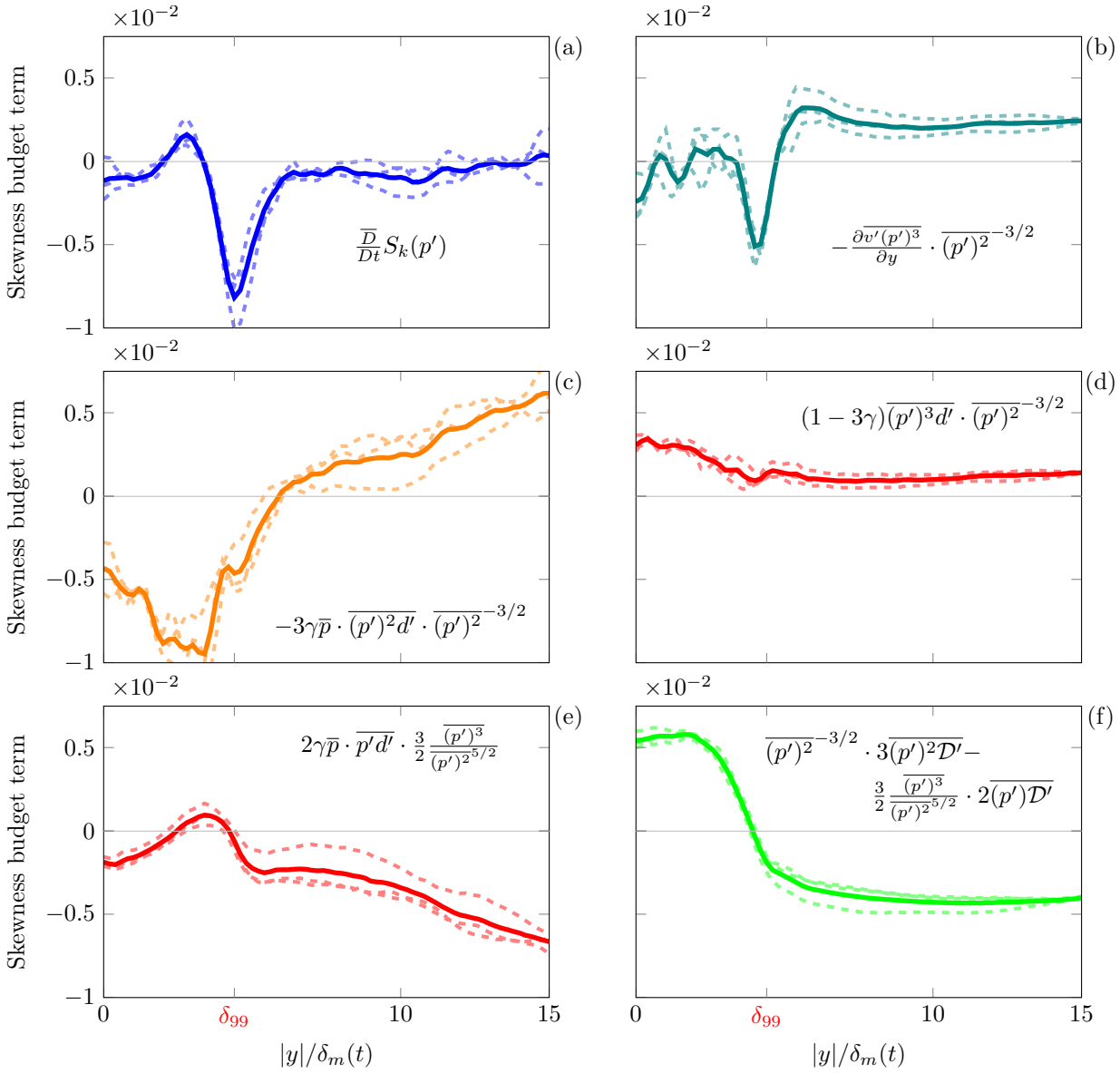

Figure 5.7: Skewness budget terms for $M = 2.5$: (dashed) three different seeds and (solid) average.

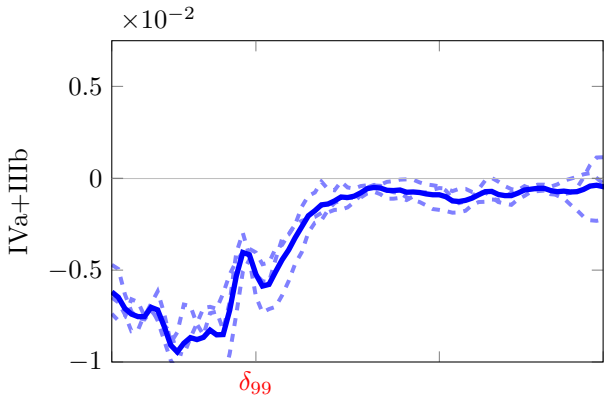

Figure 5.8: The sum of terms IVa and IIIb in (5.11) and (5.13), respectively for $M = 2.5$: (dashed) three different seeds and (solid) average.

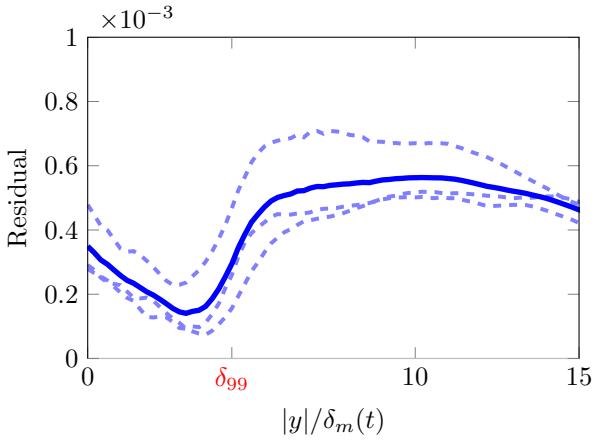

Figure 5.9: The total residual between the left and right side of (5.11) and (5.13), respectively for $M = 2.5$: (dashed) three different seeds and (solid) average.

Chapter 6

A Family of Skewness Mechanisms

This chapter describes several candidate mechanisms that can generate pressure skewness. The sharp, shock-wave-like features with distinctly skewed near-field pressure traces of section 4.2, suggest the possibility that nonlinear gas dynamics mechanism might effectively describe its source. For propagation in a homogeneous medium, linear models cannot increase S_k, and so we include (at least) weak nonlinearity to describe its generation.

To illustrate the basic gas dynamics that might lead to finite S_k, we introduce two model configurations. The underlying motivation is to relate u'-velocity fluctuations, which notionally correspond to the turbulence source, to a propagating pressure wave. In section 6.1 we include only the effect of velocity fluctuations on S_k in a one-dimensional piston-driven propagation model. In section 6.2 we introduce the additional complexity of a source plus the advection at a speed U. Both of these models include irrotational and weak-shock approximations. In section 3.4, it was shown that the temperature fluctuations in the turbulence are approximately isentropic for $y/\delta_m > \delta_{99}$, which supports this description. The near-field statistics also confirm that vorticity decays rapidly for $|y| \gtrsim \delta_{99}$ (figure 3.24), where S_k is significant. We shall see that despite these simplifications, the pressure is skewed with stronger compressions.

In section 6.3, we include a geometric effect, in which the turbulence structures are taken to be phenomenologically similar to a wavy wall, for which the waviness corresponds to the turbulence velocity fluctuations. This configuration produces an array of directional shock-like features matching the three-dimensional geometric structure of the DNS. Their corresponding pressure has the typical crackle-like waveform with $S_k \gtrsim 0.4$ for sufficiently high speed flow. The qualitative agreement is striking, and it reproduces the trends with flow speed that are seen in the DNS and also those observed for jet turbulence.

Though this description is phenomenological, not for example founded upon an acoustic analogy description, it strongly supports a near-field gas dynamics mechanism as the initial source of S_k. Crackle-like features are observed and its effect increases with M, as in the DNS. The skewness also increases with nominal turbulence intensity, further intensifying the nonlinear compressive effects, though it is insensitive to its structural details.

6.1 S_k in the piston model

The simplest configuration we consider is the generation of waves due to the often considered piston-induced motion of a gas. The well-understood space–time response is depicted in figure 6.1. This simple representation was at the core of the 'displacement-thickness' mechanism proposed by Liepmann (1954), in which the acoustic field assumed to be forced by the motion of the nominal boundary between the turbulence and the irrotational fluid beyond it. In essence, the normal velocity of the fluctuating displacement thickness is taken to act as a piston moving into a fluid. Laufer *et al.* (1964) and Howe (1981) revisited this perspective as an alternative to Lighthill's acoustic analogy (1952). The mechanistic character of this description, rather than a direct consequence of the accepted governing equations, has not developed into a quantitative model, as is the case for the more foundationally rigorous acoustic analogy. Nevertheless, it does provide a successful and well-justified mechanistic description, which is our present goal.

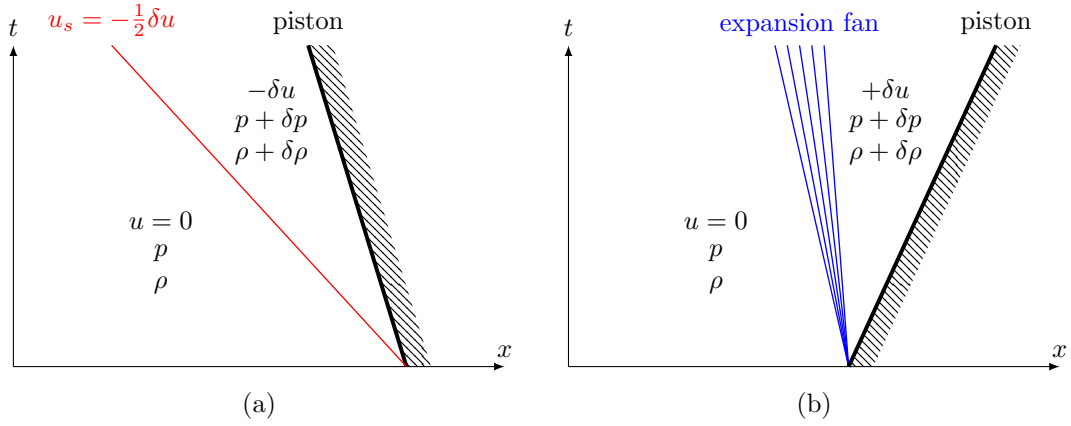

Figure 6.1: One-dimensional flow pattern from a piston: (a) compression and (b) expansion.

We start by reviewing the well-understood flow response of the piston for compressive and expansive motion, as shown in figure 6.1. The piston pushing on the fluid produces a shock wave with velocity $u_s = -\frac{1}{2}\delta u$. Assuming from the outset that the flow is isentropic, as appropriate for weak shocks, the pressure change in both waves

$$\frac{\delta p}{p} = \left[\left(1 - \frac{\gamma - 1}{2}\frac{\delta u}{c}\right)^{\frac{2\gamma}{\gamma-1}} - 1\right]. \tag{6.1}$$

(We ignore the limit in which $\delta u > 0$ is so strong that $p + \delta p = 0$.) The scale of piston velocities based on the velocity fluctuations observed in the DNS (section 3.1.1) are less than 16% of the velocity difference across the shear layers. Based on this, we expand (6.1) for small δu and retaining terms up to $O(\delta u^2)$:

$$\frac{\delta p}{p} = -\gamma\frac{\delta u}{c} + \frac{\gamma\,(\gamma+1)}{4}\left(\frac{\delta u}{c}\right)^2. \tag{6.2}$$

The resulting flow has the feature that compressions are stronger than expansions. In figure 6.2, the pressure pulse from an advancing piston is stronger than the expansion from its corresponding withdrawal, which arises simply from the nonlinearity of (6.2).

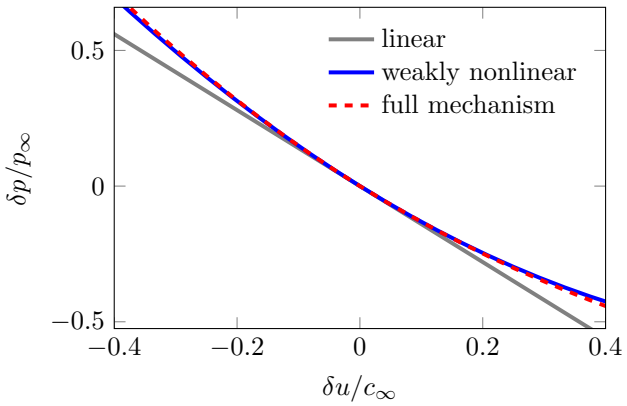

Figure 6.2: Pressure response with piston velocity: full mechanism (6.1) and weakly nonlinear (6.2).

So, even if the turbulence noise sources were to act with equal compressive and expansive components, this of itself would lead to $S_k > 0$. More specifically, we can use (6.2) to assess the δu dependence of

$$S_k(\delta p) = \frac{\overline{\delta p^3}}{\left(\overline{\delta p^2}\right)^{3/2}} \tag{6.3}$$

where

$$\frac{\overline{(\delta p)^2}}{p^2} = \gamma^2 \left(\frac{\overline{\delta u^2}}{c^2}\right) - \frac{\gamma^2(\gamma+1)}{2}\left(\frac{\overline{\delta u^3}}{c^3}\right) + \frac{\gamma^2\left(\gamma^2+2\gamma+1\right)}{16}\left(\frac{\overline{\delta u^4}}{c^4}\right) \tag{6.4}$$

$$\frac{\overline{(\delta p)^3}}{p^3} = -\gamma^3\left(\frac{\overline{\delta u^3}}{c^3}\right) + \frac{3\gamma^3(\gamma+1)}{4}\left(\frac{\overline{\delta u^4}}{c^4}\right) - \frac{\gamma^3\left(3\gamma^2+6\gamma+3\right)}{16}\left(\frac{\overline{\delta u^5}}{c^5}\right) + \frac{\gamma^3\left(\gamma^3+3\gamma^2+3\gamma+1\right)}{64}\left(\frac{\overline{\delta u^6}}{c^6}\right). \tag{6.5}$$

If we assume the distribution of piston velocities to be Gaussian

$$\overline{\delta u^2} = \left(\delta u_{\text{rms}}\right)^2 \tag{6.6}$$

$$\overline{\delta u^3} = 0 \tag{6.7}$$

$$\overline{\delta u^4} = 3\left(\delta u_{\text{rms}}\right)^4 \tag{6.8}$$

$$\overline{\delta u^5} = 0 \tag{6.9}$$

$$\overline{\delta u^6} = 15\left(\delta u_{\text{rms}}\right)^6. \tag{6.10}$$

which links the intensity of the velocities (δu_{rms}) to the resulting S_k. The velocity fluctuations in the DNS (at $y = 0$) are indeed approximately Gaussian (tables 3.3–3.4) with small $S_k(u')$: $10^{-4} \lesssim |S_k(u')| \lesssim 0.02$. Likewise, the normalized kurtosis is only $2.6 \lesssim \kappa \lesssim 2.9$ (where $\kappa = 3$ for Gaussian).

Figure 6.3 which shows how increasing δu increases pressure skewness. For small $\delta u_{\text{rms}}/c_\infty = 0.01$, the response is nearly linear with $S_k = 0.05$. In figure 6.3, we see that for $0.1 \leq v'_{\text{rms}}/c_\infty \leq 0.33$, which correspond to the v'_{rms} values from the DNS for $0.9 \leq M \leq 3.5$ at $y = 0$, would lead to somewhat stronger S_k ($0.53 \leq S_k \leq 1.6$) than is observed ($0.02 \leq \langle S_k \rangle_{y>0} \leq 0.7$, in figure 4.8), though this is not too surprising given the simplified character of this model. There is no expectation that the turbulence would be so acoustically efficient as a one-dimensional piston model.

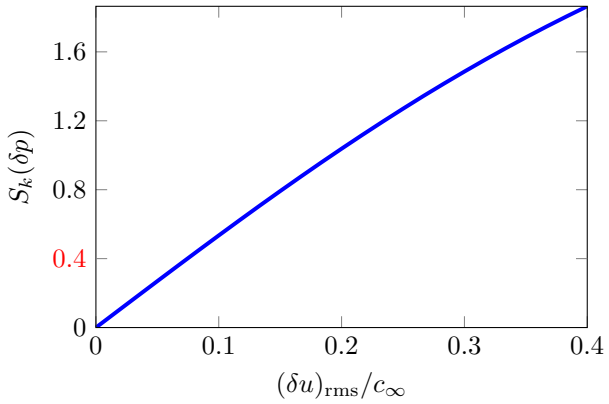

Figure 6.3: Pressure skewness variation with piston velocity intensity.

6.2 Compression along a streamline

We now include rudimentary flow effects and consider the steady, one-dimensional compression of an isentropic gas due to area contraction as shown in figure 6.4.

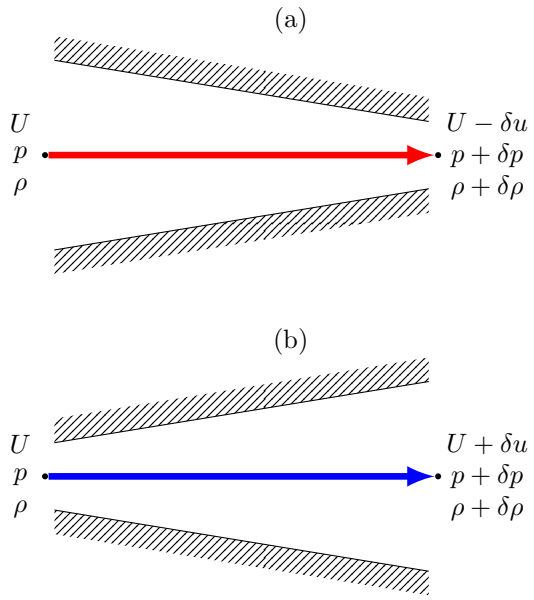

Figure 6.4: One-dimensional (a) compression and (b) expansion along a streamline.

Omitting the effects of viscosity, the steady, one-dimensional conservation of momentum and mass,

$$u\frac{du}{dx} = -\frac{1}{\rho}\frac{dp}{dx}, \tag{6.11}$$

link the properties of the inflow to the outflow in figure 6.4 by

$$\int_U^{U+\delta u} u du = -\int_p^{p+\delta p} \frac{dp}{\rho}. \tag{6.12}$$

As in section 6.1, the density and pressure are related isentropically by

$$\left(\frac{p}{p+\delta p}\right) = \left(\frac{\rho}{\rho+\delta\rho}\right)^{\gamma}, \tag{6.13}$$

and with (6.12) leads to

$$\frac{\delta p}{p} = \left\{\left[1 - \frac{\gamma-1}{c^2}\left(\frac{1}{2}\left[(U+\delta u)^2 - U^2\right]\right)\right]^{\frac{\gamma}{\gamma-1}} - 1\right\}. \tag{6.14}$$

Retaining up to second-order velocity changes with $M = U/c$ yields

$$\frac{\delta p}{p} = -\gamma M\left(\frac{\delta u}{c}\right) + \frac{\gamma(M^2-1)}{2}\left(\frac{\delta u}{c}\right)^2, \tag{6.15}$$

which is appropriate since the midplane velocity fluctuations in the DNS are $\lesssim 0.16\Delta U$. Figure 6.5 shows that the nonlinear compressive effects of flow deceleration, $-\delta u$, leads to stronger pressure compressions. This figure also shows that the weakly nonlinear approximation in (6.15) agrees with the full mechanism in (6.14). Now including the effects of a free-stream velocity, figure 6.5 (b) shows that the pressure-amplitude asymmetry is accentuated with increasing Mach number.

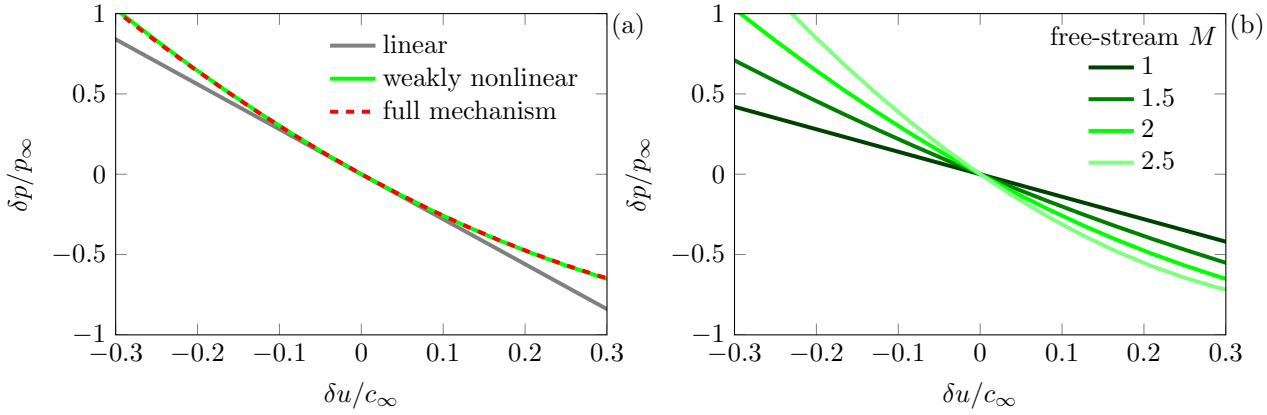

Figure 6.5: (a) Pressure response to velocity changes along a streamline at $M = 2$: full mechanism (6.14) and weakly nonlinear (6.15). (b) The effects of flow speed using (6.15).

For this model, the second- and third-order moments of (6.15) that makeup S_k are

$$\frac{\overline{(\delta p)^2}}{p^2} = \gamma^2 M^2 \left(\frac{\overline{\delta u^2}}{c^2}\right) + \gamma^2 (M - M^3)\left(\frac{\overline{\delta u^3}}{c^3}\right) + \gamma^2 \frac{1 - 2M^2 + M^4}{4}\left(\frac{\overline{\delta u^4}}{c^4}\right) \tag{6.16}$$

$$\frac{\overline{(\delta p)^3}}{p^3} = -\gamma^3 M^3 \left(\frac{\overline{\delta u^3}}{c^3}\right) - \gamma^3 \frac{3M^2 - 3M^4}{2}\left(\frac{\overline{\delta u^4}}{c^4}\right) - \gamma^3 \frac{3M - 6M^3 + 3M^5}{4}\left(\frac{\overline{\delta u^5}}{c^5}\right) - \gamma^3 \frac{1 - 3M^2 + 3M^4 - M^8}{8}\left(\frac{\overline{\delta u^6}}{c^6}\right)$$

Following section 6.1 for Gaussian velocity disturbances, we see in figure 6.6 the pressure skewness increases with both the M and the compression intensity (δu_{rms}). At $M = 1$, the skewness is zero and independent of δu_{rms}. Above $M = 1$, the skewness rises rapidly and then slows down at higher speed in a manner similar to observations in the DNS shown in figure 4.8.

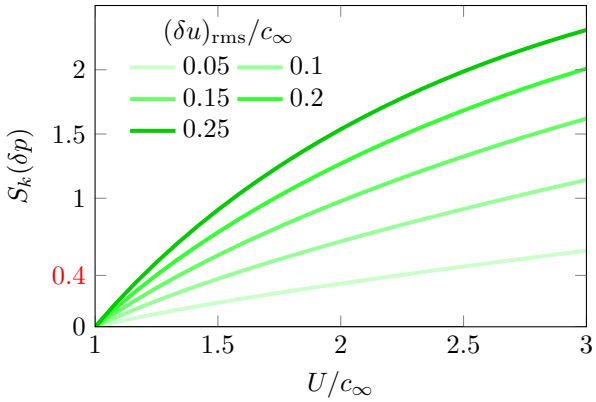

Figure 6.6: Effect of fluctuating flow speed on pressure skewness.

6.3 Supersonic flow adjacent to a wavy-wall-like boundary

The basic flows in sections 6.1-6.2 show that gas dynamic nonlinearity will tend to yield $S_k > 0$. Still, they are only statistical assessments, which include neither the geometric features of free-shear-flow turbulence nor the distinct shape of the pressure waves. The weakly nonlinear wavy-wall model we introduce includes these additional features. It also facilitates more direct parameterization based on turbulence scales observed in the shear layer. We will examine its propagation and compare with the near-field of the DNS.

Figure 6.7 (a) shows the uniform flow adjacent to a wavy wall. The amplitude of the surface's waviness is set by the amplitude, ε. The plane of normal velocities at $y = 0$, in figure 6.7 (b), which we use to force the proposed model, is set via a linearization of the kinematic boundary condition of the wavy wall about $y = 0$ in the limit that the wall height $\varepsilon \ll 1$. To first order, with $\varepsilon \ll 1$, the normal velocities on $y = 0$ is $v'(x, z) = \varepsilon g_x(x, z) + O(\varepsilon^2)$. In this limit, we are modeling the flow adjacent to a wavy-wall-like boundary condition on the plane $y = 0$.

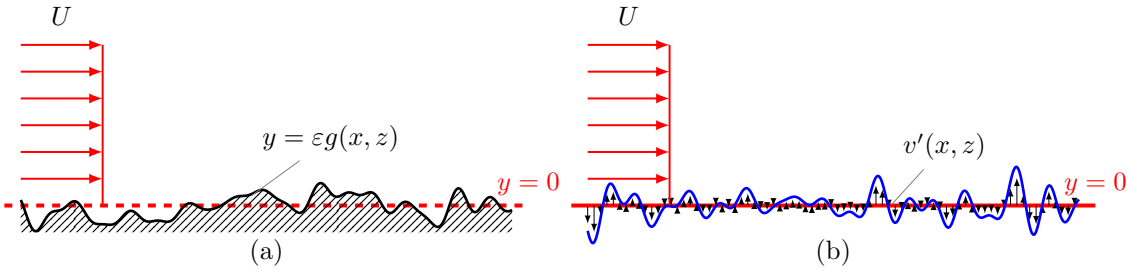

Figure 6.7: (a) Uniform flow adjacent to a wavy wall. (b) The induced v'-velocity at the $y = 0$ plane from (a) for $\varepsilon \ll 1$.

6.3.1 Simulation configuration

The weakly nonlinear wavy-wall flow is tractable for two-dimensional waviness (Van Dyke, 1951), but not in general for three-dimensional weak nonlinearity. Also, as with many of these asymptotic approximations, like the one given by Van Dyke (1951), they are not uniformly valid for $y > \varepsilon^{-1}$, over which waves are expected to steepen and form shocks. To deal with these limitations, we directly simulate the flow using the same highly accurate methods discussed in section 2.2.

Figure 6.8 visualizes a plane of the three-dimensional computational domain used to simulate the flow adjacent to the wavy-wall-like boundary. The plane of normal velocities at $y = 0$ acting on the adjacent supersonic flow is taken from the midplane of the DNS when $\delta_m(t)/\delta_m^o = 10$. These are shown in figures 6.9 (a) through (d). The structure of the distribution of velocities clearly depends on the flow speed where they were taken, becoming more streamwise correlated at high speeds. Obviously, the velocity field in the DNS is unsteady, but we use the instantaneous field to access their spatial distribution and intensity. This will facilitate a direct comparison to the DNS keeping in mind the unsteadiness from the turbulence has been omitted.

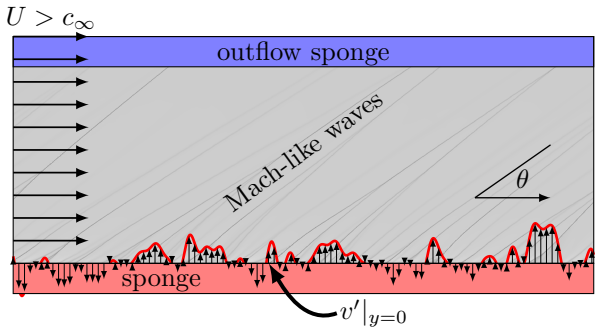

Figure 6.8: Computational box forced by $v'(x, z, t)$ plane from DNS when $\delta_m(t)/\delta_m^o = 10$.

The computational domain in the periodic x- and z-directions are identical to those described for the DNS in section 2.1, though we focus on the half plane, $0 < y/\delta_m^o < 175$. The compressible flow equations (2.3)–(2.5) are discretized in the same way as in the turbulent shear layers, discussed in section 2.2. The flow field is initialized by

$$\mathbf{q_o} = \left[\rho_\infty, \rho_\infty U, 0, 0, \frac{p_\infty}{\gamma - 1} + \frac{1}{2}\rho_\infty U^2\right]^{\mathrm{T}}, \tag{6.17}$$

and after an initial transient, the flow attains a stationary state. We choose the adjacent M in (6.17) to be based on

$$M_{co} = \frac{\Delta U + 1}{2c_\infty}, \tag{6.18}$$

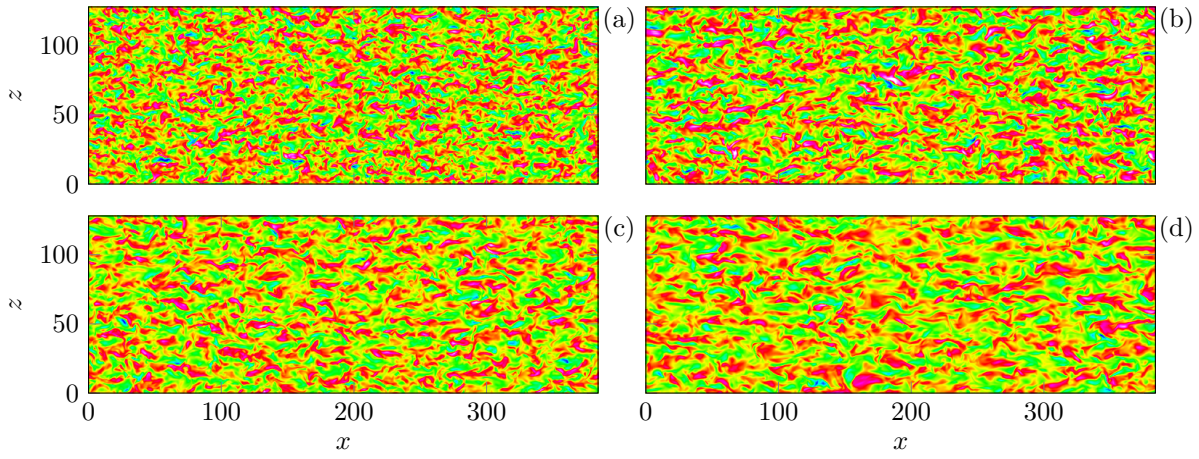

Figure 6.9: x-z planes of the y-velocity fluctuations from the DNS for (a) $\Delta U/c_\infty = 1.5$, (b) 2.5, (c) 3.0, and (d) 3.5. The colormap spans $-0.35 < v'/\Delta U < 0.35$.

with ΔU the velocity difference in the corresponding DNS. The orientation of the Mach-like waves above the mixing layer followed closely (within 2°) to the angle $\theta = \sin^{-1}[1/M_{co}]$ as shown in section 4.3. We examine the effect of the free-stream velocity on S_k separately in section 6.3.6. Table 6.1 summarizes the details of each of the simulations in this section.

v' detail in figure 6.9	U/c_∞	v'_{rms}/c_∞
(a)	1.25	0.150
(b)	1.75	0.255
(c)	2.00	0.296
(d)	2.50	0.343

Table 6.1: Summary of the wavy-wall model simulations.

The normal velocity fluctuations at $y = 0$ are set by a sponge-like forcing term added to the flow equations between $-25 < y/\delta^o_m < 0$ by

$$N(\mathbf{q}) = -A(y)\left[\mathbf{q} - \mathbf{q}_t\right], \tag{6.19}$$

where the target solution is

$$\mathbf{q}_t = \begin{bmatrix} \rho_\infty \\ \rho_\infty \left[U, v(x,z), 0\right] \\ \frac{p_\infty}{\gamma - 1} + \frac{1}{2}\rho_\infty \left(U^2 + v(x,z)^2\right) \end{bmatrix}. \tag{6.20}$$

To enforce the target at $y = 0$, the sponge strength is set by $A(y) = \frac{1}{2}(1 - \tanh(5y))$ which is zero beyond $y > 0$ as shown in figure 6.8. The results for this particular sponge enforcement (6.19) are compared to a

simultaneous-approximately-term (SAT) approach in an independent compressible flow solver in the next section.

6.3.2 Verification of the wavy-wall-like flow model

Before considering the three-dimensional flow in section 6.3.1, we verify the model for the planar case. First, we verify the formulation of the wavy-wall-like boundary conditions in (6.19) by comparing the solution to an independent flow solver that is described in detail in Vishnampet (2015). The boundary conditions there are implemented using the simultaneous-approximation-term (SAT) approach to enforce the v'-fluctuation field at $y = 0$. The penalty term added to the governing equations that enforce the boundary conditions is

$$N(\mathbf{q}) = -\sigma_I P^{-1} E A^{+} \left(\mathbf{q} - \mathbf{q}_I\right), \tag{6.21}$$

where $\sigma_I = 1$ is the penalty strength, $E = (1, 0, \ldots, 0)^{\mathrm{T}}$, and P is an operator associated with the finite-difference approximation of spatial derivatives. The matrix A^{+} selects the incoming characteristics of the flow equations. A detailed explanation of the right side of (6.21) can be found elsewhere (Bodony, 2010; Vishnampet, 2015). The target data $\mathbf{q}_I$ is set to

$$\mathbf{q}_I = \begin{bmatrix} \rho \\ \rho\left(\mathbf{u} - \left[(\mathbf{u}\cdot\mathbf{n}) - (\mathbf{u}_l\cdot\mathbf{n})\right]\mathbf{n}\right) \\ \frac{p}{\gamma-1} + \frac{1}{2}\rho\left(\mathbf{u} - \left[(\mathbf{u}\cdot\mathbf{n}) - (\mathbf{u}_l\cdot\mathbf{n})\right]\mathbf{n}\right)^2 \end{bmatrix}, \tag{6.22}$$

where $\mathbf{u}_I = [u, v(x,z), w]$ with normal vector $\mathbf{n} = [0, 1, 0]$. The discrete time integrator is a fourth-order Runge–Kutta scheme which is identical to that in the present code in section 2.2. The spatial derivatives are approximated by the same type of compact finite-differences as described in appendix A. The first-order derivatives are approximated with a fourth-order accurate boundary and eighth-order accurate interior finite-difference schemes (Vishnampet, 2015). The second derivatives in the viscous fluxes are approximated by repeated first-order derivatives (Vishnampet, 2015).

Figure 6.10 shows the collapse of the skewness and pressure intensity between the two solvers. The convergence between the two solvers with mesh refinement has not been assessed; however, the agreement at this level of grid spacing suggest that our conclusions are insensitive to the particular enforcement of the normal velocity boundary condition. Another notable difference between the flow solvers is the numerical filter to stabilize the solution. Where Vishnampet (2015) uses a SAT-dissipation term added to the right side $\mathcal{N}(\mathbf{q})$, the current DNS filters the flow field after every $5\,\Delta t$ as explained in section 2.2. Although

the numerical filter effect in the DNS has little effect on S_k, as shown in figure 4.12, the formulation in (Vishnampet, 2015) is expected to contribute to the differences in figure 6.10.

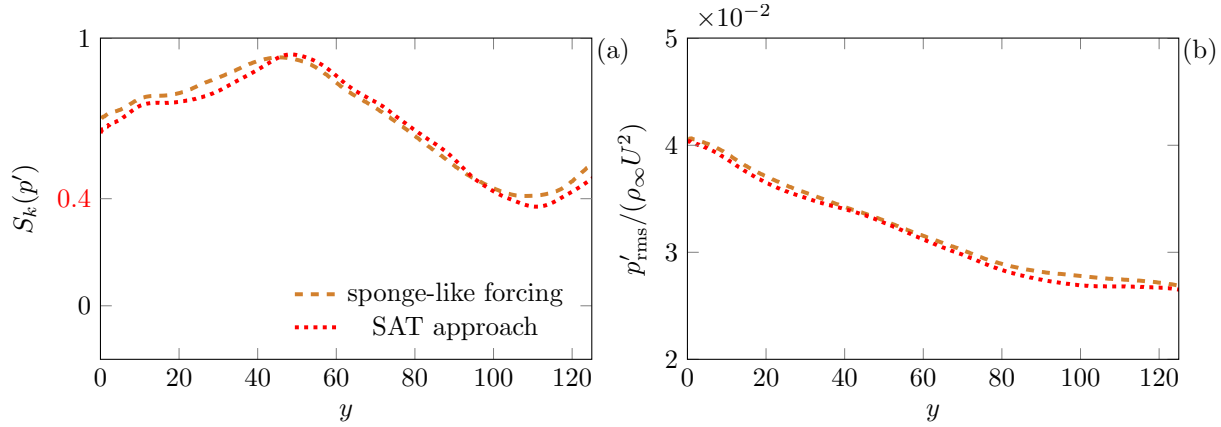

Figure 6.10: Effect of the boundary implementation on the (a) pressure skewness and (b) pressure intensity with distance from the wall-like boundary for $M = 1.75$.

Figure 6.11 compares the pressure response along $y = 0$ for $M = 1.75$ between the simulations and the weakly nonlinear asymptotic description of Van Dyke (1951), which is explained in appendix B. The large velocity fluctuations, beyond $|v'| \gtrsim 0.1$, lead to the anticipated asymmetric pressure response due to the nonlinear compressive effects. The simulations follow closely to the inviscid theory, suggesting that the viscosity and thermal conductivity, which were retained in the wavy-wall solvers, do not affect the response. Likewise, their agreement confirms that the weakly nonlinear model of Van Dyke (1951) includes the essential nonlinearities for the phenomena.

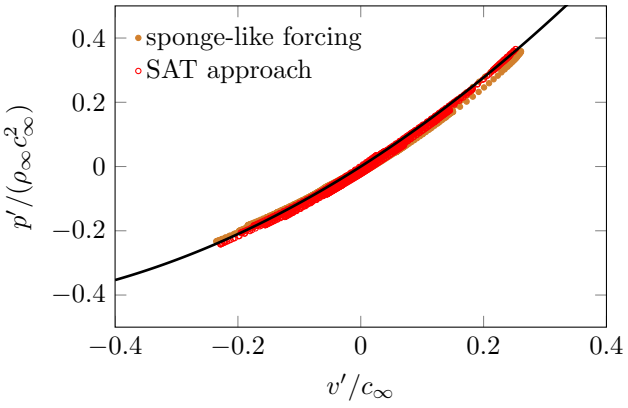

Figure 6.11: Effect of the boundary implementation on the pressure variation with v'-velocity along the boundary $y = 0$ at $M = 1.75$. The solid curve is the weakly nonlinear theory of Van Dyke (1951).

6.3.3 Visualization

For the three-dimensional simulations which facilitate comparison to the DNS, figure 6.12 (a) shows an array of sharp shock-like waves oriented with the Mach angle associated with the free-stream speed from simulation (b) in table 6.1. The sharp waves extend to the boundary $y = 0$. The waves in the DNS are directional, but also appear to have finer-scale fluctuations atop the strong waves.

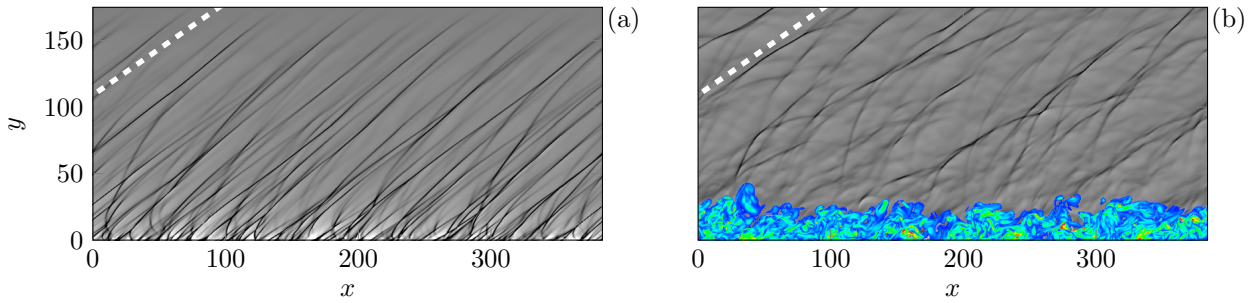

Figure 6.12: x-y planes of dilatation at $z = L_z/2$ for (a) $M = 1.75$ and (b) $M = 2.5$ ($M_{co} = 1.75$). The dashed line indicates the Mach angle.

In figure 6.13 (a), arched shock-like wave cross each other. When viewed from 'above' in x-z planes in figure 6.14, the waves are curved and intersect nearby waves in a similar pattern to the DNS. Remarkably, the model flow reproduces a similar three-dimensional wave structure observed above the turbulence. The following section will assess their corresponding pressure statistics.

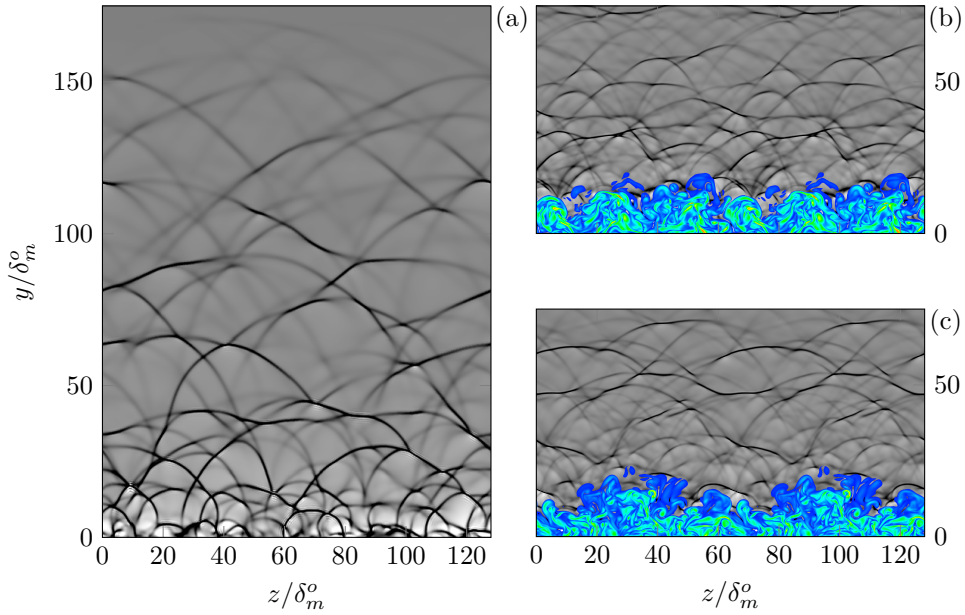

Figure 6.13: Dilatation in the z-y plane at $z = L_z/2$ for the (a) steady model $M = 1.75$ (b) upper half-plane and (c) lower half-plane oriented upwards from the DNS $M = 2.5$ ($M_{co} = 1.75$).

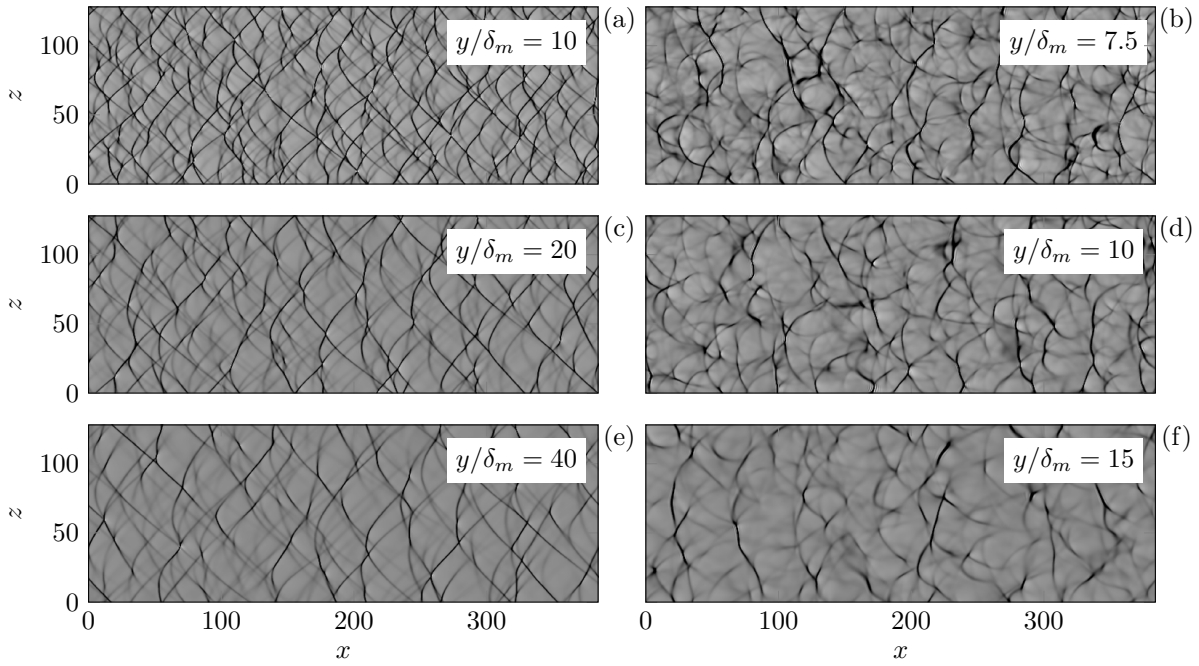

Figure 6.14: x-z planes of dilatation for (a)-(c)-(e) $M = 1.75$ and (b)-(d)-(f) $M = 2.5$ ($M_{co} = 1.75$).

6.3.4 Pressure statistics

The phenomenological gas dynamics models we consider can also be used to anticipate the effects of the nonlinearities they embody on the sound pressure statistics. In figure 6.15, for $M \gtrsim 1.75$ the pressure fluctuations have steep compressions followed by shallower, rounded expansions. For $M = 1.25$, the waves appear to be steepened, though they do not show an obvious amplitude asymmetry as for $M \geq 1.75$.

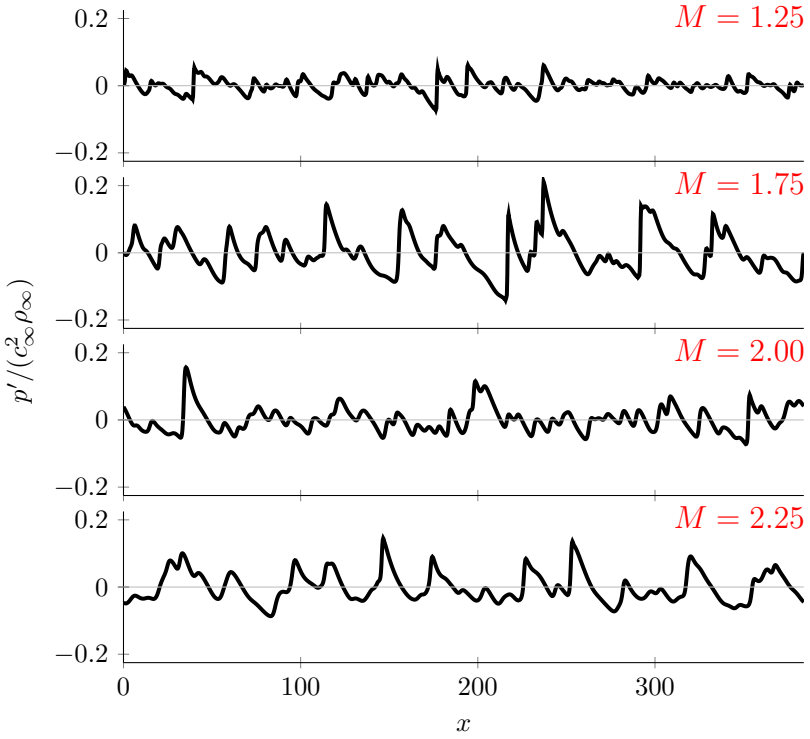

Figure 6.15: Effect of Mach number on the pressure fluctuations $p'(x)$ at $y/\delta_m^o = 25$ on $z = 0$.

Figure 6.16 shows that for $M \geq 1.75$, the pressure skewness exceeds $S_k \gtrsim 0.4$ The variation of S_k with y also appears to be relatively constant as for the DNS in figure 4.6.

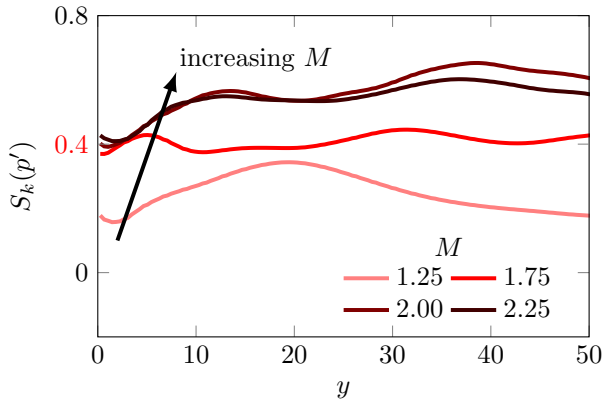

Figure 6.16: Variation in the pressure skewness.

In figure 6.17, the trend and magnitude of the domain average S_k,

$$\langle S_k \rangle_{y>0} = \frac{1}{N} \sum_{i=1}^{N} S_k(y_i), \tag{6.23}$$

for $1.25 \lesssim M \lesssim 2$ agrees with those observed in the turbulent mixing layers. We note that in the figure

the Mach number scale for the DNS takes the convection Mach number (6.18) which was the basis for the free-stream M in the model flow.

These results provide the foundation that crackle noise appears naturally in a comparable model flow to high-speed free-shear-flow turbulence. Here, the skewness rises from nonlinear compressive effects at the boundary $y = 0$ and exceeds values expected for crackle to be audible, $S_k \gtrsim 0.4$ for $M \gtrsim 1.75$. Parameterized by scales observed in the DNS, the noise characteristics agree with those above the turbulent mixing layers. The next sections are intended to assess the robustness of this model with respect to its parameterization: the particular structure of $v(x, z)$, the free-stream M, and the amplitude of the velocity fluctuations.

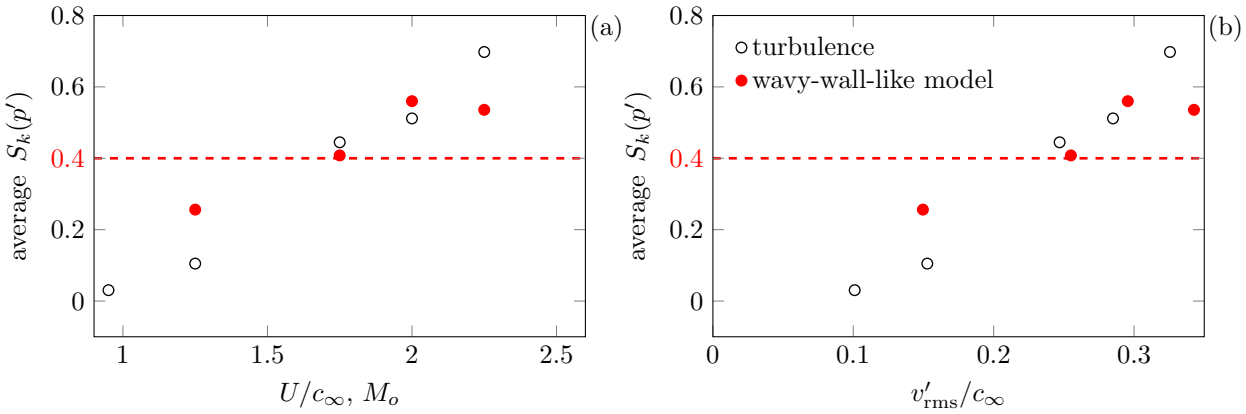

Figure 6.17: Mean domain skewness dependence on (a) free-stream M and (b) v'_{rms}.

6.3.5 Effect of the wavy-wall-like structure

The previous section showed that a wavy-wall-like model, parameterized by the scales of the DNS, can lead to crackle-like noise. We now examine the effect of the particular structure of the normal velocities on pressure skewness. A main question is whether or not it is the spatial structure of the $v(x,z)$ with M that leads to crackle and their observed sound patterns. Visually in figure 6.9 (a)–(d), the spatial structure of $v(x,z)$ is more streamwise elongated with increasing M. Similar observations have been made in experiments (Fourguette *et al.*, 1991; Clemens & Mungal, 1992; Rossmann *et al.*, 2002) and simulation (Freund *et al.*, 2000*a*). Here, we examine the possibility of a structural dependence on S_k by adjusting the boundary y-velocity field in two ways from the baseline case (b) described in section 6.3.1. First, the $v(x,z)$ is transformed as

$$\hat{v}(k_x,k_z) = \frac{1}{N_x N_z}\sum_{j=0}^{N_z-1}\sum_{m=0}^{N_x-1} v(x_m,z_j)\exp(-2i\pi k_x m/N_x)\exp(-2i\pi k_z j/N_z), \tag{6.24}$$

and the energy in the top 95% modes is set to zero by

$$\hat{v}(k_x,k_z) = \begin{cases} 0, & |k_x| > 0.05\frac{N_x}{2},\ |k_z| > 0.05\frac{N_z}{2} \\ \hat{v}(k_x,k_z), & \text{otherwise,} \end{cases} \tag{6.25}$$

This smooths the y-velocity, as shown in figure 6.18 (b). In another test, we disrupt the three-dimensional correlation of the structures in the x- and z-directions. To generate a decorrelated velocity field, two random numbers (a,b) are used to rescale the energy in $\hat{v}(k_x,k_z)$ as

$$\hat{v}_s(k_x,k_z) = \frac{a+ib}{\sqrt{a^2+b^2}} \times |\hat{v}(k_x,k_z)|. \tag{6.26}$$

The inverse Fourier transform of (6.26) is shown in figure 6.18 (c). This procedure retains the original energy spectrum in $v(x,z)$ but disrupts its structures as seen in figure 6.18 (c).

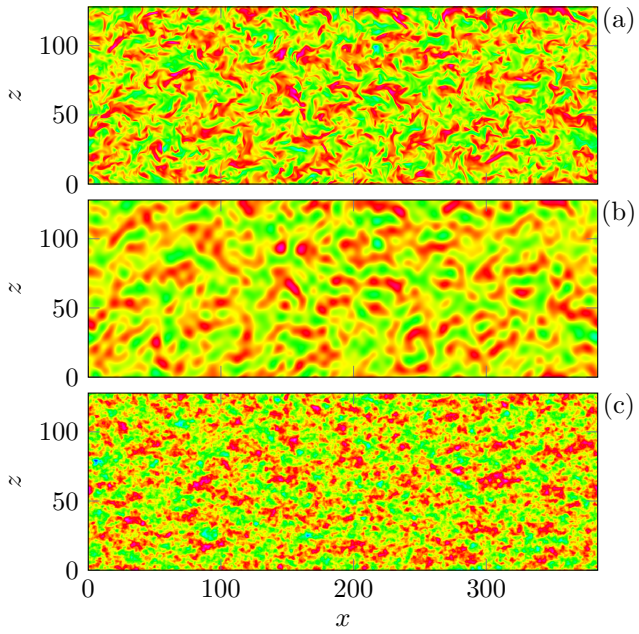

Figure 6.18: x-z planes of v at $y = 0$ for different modifications to the transformed normal velocities in (6.24): (a) unaltered (b) filtered high wavenumber components (6.25) and (c) randomized phases of all modes (6.26).

Figure 6.19 shows the effect of the different adjustments to v' on its sound. The filtering of the high-wavenumber modes from (6.25) results in near-field acoustics with less fine-scale structure, while retaining the large-scale curved shock-like waves. The general structure in the wave patterns from the original in figure 6.19 (a) and the decorrelated field in (c) do not appear to be extremely different. They both share sharp, curved shock-like waves with similar fine-scale structure.

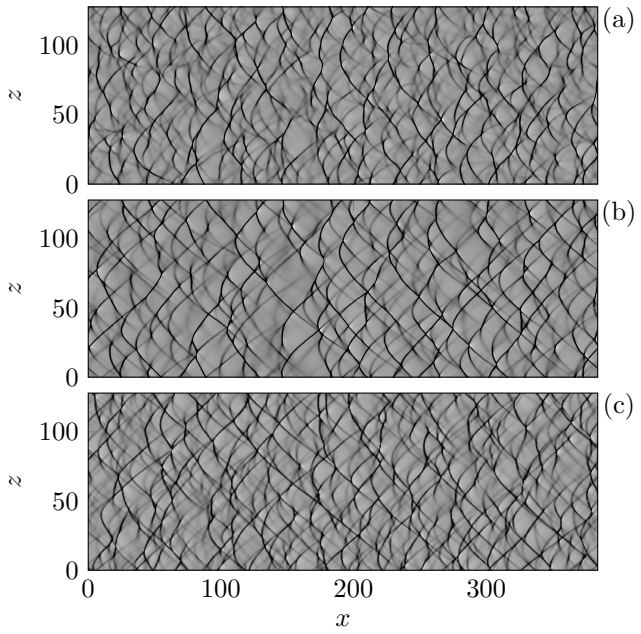

Figure 6.19: Dilatation at $y/\delta_m^o = 25$ for different modifications to the normal velocities: (a) unaltered (b) filtered high-wavenumber components (6.25) and (c) randomized phases of all modes (6.26).

Figure 6.20 compares the pressure statistics for the different adjustments to the structure. Skewness appears relatively constant for $y > 0$ just as in the DNS. The skewness variations are only weakly affected by the structural changes.. The average from (6.23) are (a) $\langle S_k \rangle_{y>0} = 0.41$, (b) 0.39, and (c) 0.35. With respect to the strong spatial filtering of small scales, the average skewness decreased by only 5%. This result is consistent with the relative insensitivity of S_k in flow turbulence to changes in the small-scale structures shown in figure 4.11 and 4.12. The pressure intensity in figure 6.20 (b) show very good collapse at $y \gtrsim 10$ between the different structures. The filtered-v plane is quieter because energy in the highest modes was set to zero; the input velocity is less intense on average. So, to first order, with $v' \propto p'$, the filtering effect results in a quieter sound field.

The spatially-decorrelated v'-plane reduces $\langle S_k \rangle_{y>0}$, but only by 12.5% with respect to the original flow. It can be expected from these results that strictly altering the turbulence source structure in high-speed flows will not entirely mitigate skewness. We find some support in these observations from experiment data, though both the turbulence structure and intensity were modified by the control. Microjet injection into the near-nozzle jet turbulence reduces skewness in the peak noise direction (Greska, 2005). The corresponding turbulence statistics with this control reveals a simultaneous decrease in the spatial correlation of the turbulence along with a decrease in turbulence intensity within the shear layers (Krothapalli *et al.*, 2003*b*). Based on these two compounding factors in the experiments, it is unclear which of these effects played the larger role in the skewness reduction. The results of our comparative model flow suggest that decorrelation plays

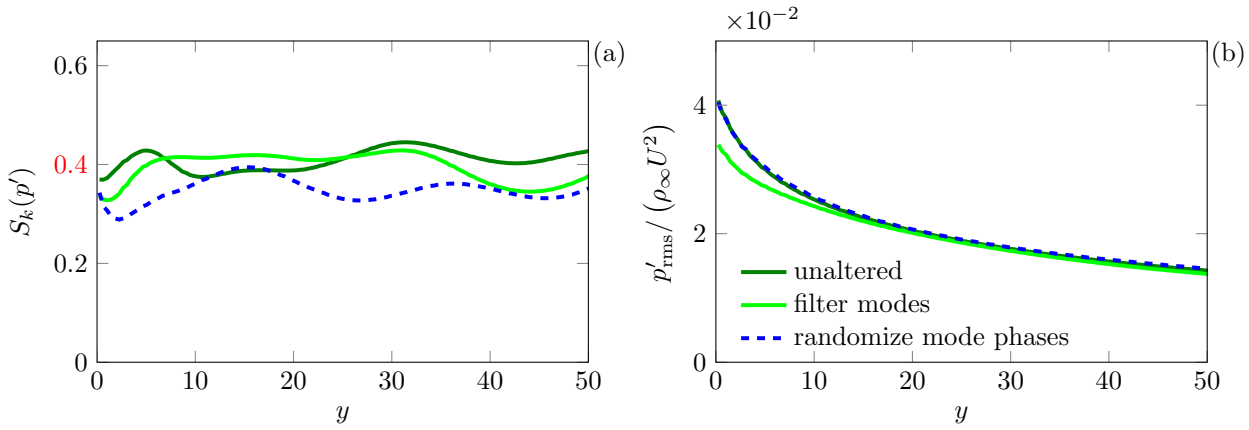

Figure 6.20: Effect of structural adjustments to $v(x,z)_{y=0}$ on the (a) pressure skewness and (b) pressure with distance from the wall-like boundary.

a minor role, but it can reduce the skewness slightly. In the following section we parse out these individual factors by examining the effect of the normal velocity without altering its spatial structure.

6.3.6 Effect of the M and $v'_{\mathbf{rms}}$

The previous section indicated that the pressure statistics are relatively insensitive to the structural changes to the normal velocities at the boundary. We now consider the effects of M and amplitude of v' without changing its structure. To adjust the velocity amplitude, we normalize the $v(x,z)$ in figure 6.18 (a) by

$$\tilde{v}(x,z) = Av(x,z), \tag{6.27}$$

and consider the range of amplitudes $10^{-4} \leq A \leq 1.25$. Figure 6.21 shows that the pressure skewness and intensity decrease with the amplitude of the fluctuations. Even for supersonic speeds, $M = 1.75$, $\langle S_k \rangle$ falls below $\langle S_k \rangle_{y>0} < 0.4$ for $v'_{\mathrm{rms}} < 0.2$ in figure (6.22). This indicates that nonlinearity is essential to the development of finite S_k.

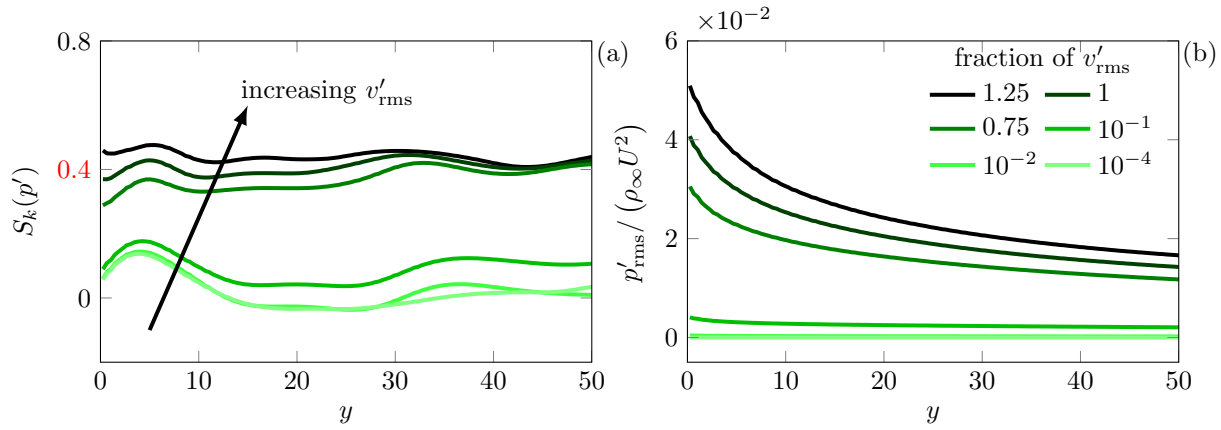

Figure 6.21: Effect of velocity amplitude on the variation of (a) pressure skewness and (b) pressure intensity with distance from the wall-like boundary for $M = 1.75$.

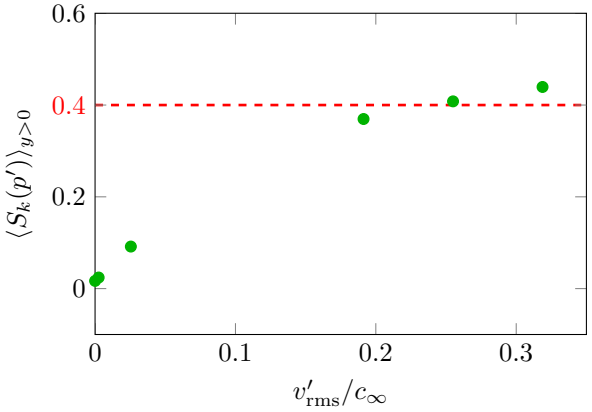

Figure 6.22: Effect of velocity amplitude on the average skewness (6.23) for $M = 1.75$.

Figure 6.23 (a) shows that skewness increases with M and exceeds $S_k \gtrsim 0.4$ for $M \gtrsim 1.5$. The average skewness in figure 6.24 shows that S_k increases rapidly in the range $1 \lesssim M \lesssim 1.5$ and slower for $M \gtrsim 1.5$, which is similar to the behavior seen in the DNS in figure 4.8. Given the insensitivity of the intensity to the structure, a logical control strategy would limit the turbulence level or the relatively supersonic free-stream velocity 'seen' by the eddies, or a mixture of both.

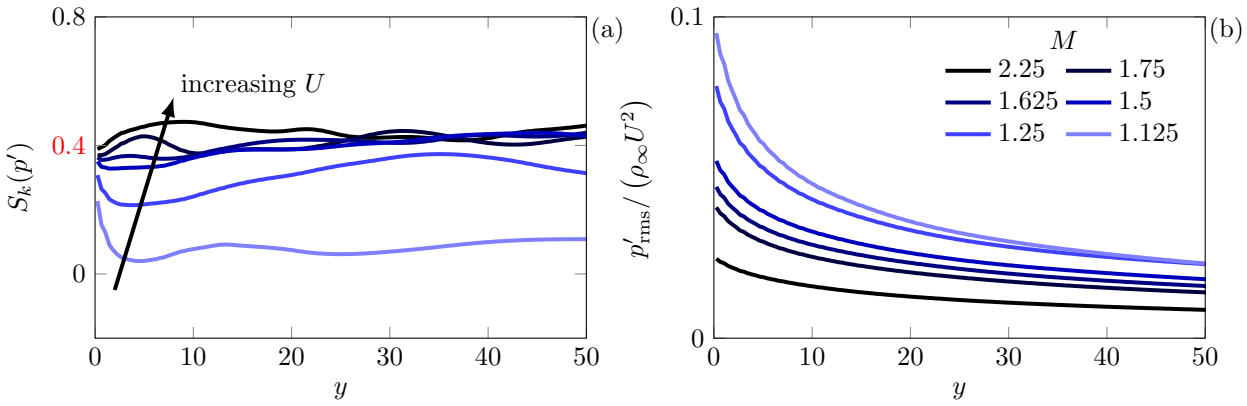

Figure 6.23: Effect of Mach number on the (a) pressure skewness and (b) pressure intensity from the wall-like boundary for $v'_{\mathrm{rms}}/c_\infty = 0.255$.

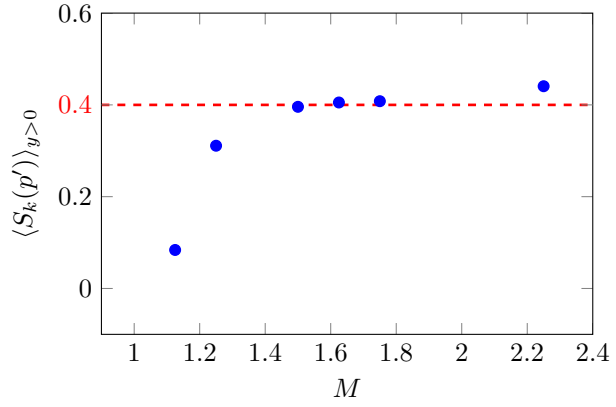

Figure 6.24: Effect of Mach number on $\langle S_k \rangle$ for $v'_{\mathrm{rms}}/c_\infty = 0.255$.

Chapter 7

The role of large-scale structures on crackle noise

This chapter addresses whether or not the crackle sound patterns are intrinsically linked to their three-dimensional turbulent structure at high speed. This is assessed by imposing a novel modification of it, motivated by the known instabilities of high- versus low-speed free-shear flows. We show that the structure of the $M = 2.5$ turbulence has little affect on S_k. In fact, forcing the high-speed flow to more closely mimic the relatively two-dimensionally correlated structure of the lower speed flow leads to louder noise and moderately higher values of S_k, supporting our analysis of the previous chapters that S_k is linked to the compressibility of the flow rather than to its particular structure. This offers additional support that the basic robustness of S_k to its source structure is also seen in the simpler model flow discussed in section 6.3.5.

7.1 The three-dimensional structure in high-speed free-shear flows

Figure 7.1 visually compares the spatial structure of the pressure disturbances at different Mach numbers. The pressure disturbances in the subsonic flow in figure 7.1 (a) has larger and more spanwise correlated pressure fluctuations compared to supersonic flow in (c). Their corresponding two-point correlations of pressure

$$C_{pp}(\Delta x, \Delta z) = \frac{\langle p'(x,z)p'(x+\Delta x, z+\Delta z)\rangle}{\langle p'(x,z)p'(x,z)\rangle} \tag{7.1}$$

in figures 7.1 (b) and (d) shows the larger spanwise correlation for $M = 0.9$. Similarly, simulations of turbulent annular shear layers have azimuthally correlated pressure structures at low Mach numbers compared to more spanwise elongated structures with increasing Mach number (Freund *et al.*, 2000*a*). Experimental observations of planar shear layers (Clemens & Mungal, 1992; Rossmann *et al.*, 2002) and round jets (Fourguette *et al.*, 1991) indicate the same trend with Mach number. It is this structural change at high speed that we evaluate as potentially important to the acoustic field structure and its distinct pressure skewness.

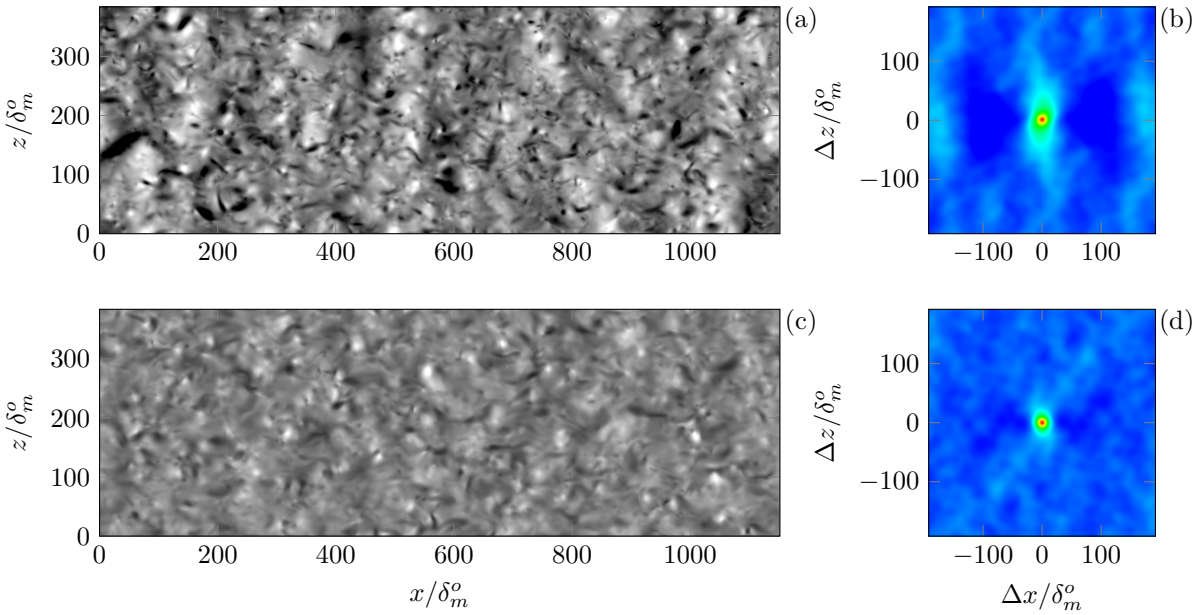

Figure 7.1: x-z plane of pressure fluctuations with gray-scale levels $-0.075 \leq p'/(\rho_\infty \Delta U^2) \leq 0.075$ at $y/\delta_m(t) = 10$ for (a) $M = 0.9$ and (c) 2.5. Normalized space-space correlation of pressure of (7.1) for (b) $M = 0.9$ and (d) 2.5. Correlation colormap range from -0.1 to 0.9.

We find support in figure 7.2 that suggest a connection between the turbulence structure and the sound structure beyond the turbulence at high speed. In figure 7.2 (a), the low-speed gas penetrates the high-speed, acetone-rich gas which led Rossmann *et al.* (2002) to consider that the lower-speed features 'jutting' into the high-speed stream act as a bluff body which compress the oncoming supersonic fluid in a bowed shock-like-wave structure. Visualization from the DNS in figure 7.2 (b) also show a similar curved wave pattern around 'lumps' of vorticity penetrating the $y/\delta_m = 3$ plane. The curved waves are also seen to persist above the mixing layers in figure 7.2 (c) and (d).

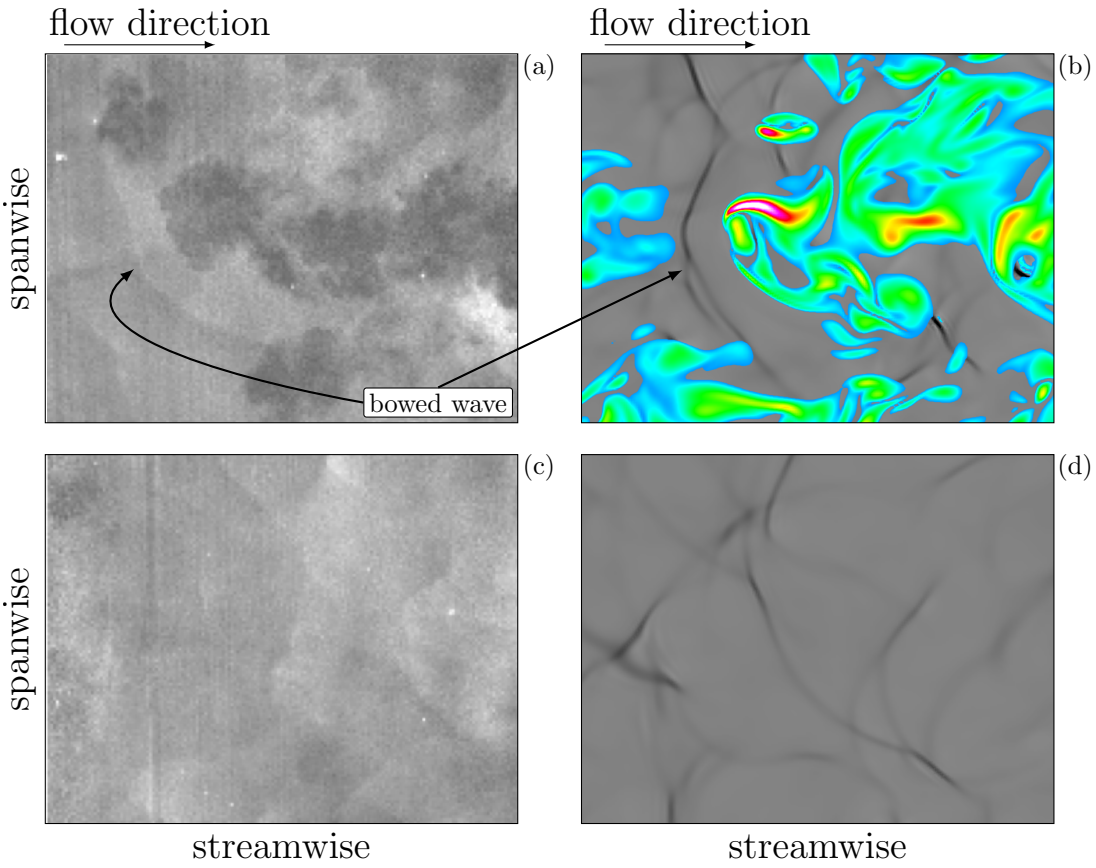

Figure 7.2: Flow visualizations above turbulent mixing layers. The PLIF images are taken above a spatially-developing mixing layer at (a) $y/\delta = 2.5$ and (c) 5.0 for $M_c = 1.7$ (Rossmann *et al.*, 2002). The colormap is acetone concentration where dark gray is acetone lean. The DNS is visualized with vorticity magnitude (color) and $\nabla \cdot \mathbf{u}$ (gray) at (b) $y/\delta_m = 3$ and (d) 5 for $M_c = 1.75$.

In a view even farther above the turbulence in figure 7.3 (c) the DNS has an array of curved pressure waves. In contrast, the field above the subsonic mixing layer in figure 7.2 (b) is absent this distinct curved wave pattern. It is in the three-dimensional wave pattern in figure 7.3 (c) where $S_k \gtrsim 0.4$. The $S_k \approx 0$, subsonic counterparts, on the other hand, have a spanwise correlated turbulence with a similar spanwise coherence in the acoustic field. We therefore consider the possibility that S_k is linked to the streamwise elongated turbulence which appear to be linked to the generation of curved waves as in figure 7.2 (b).

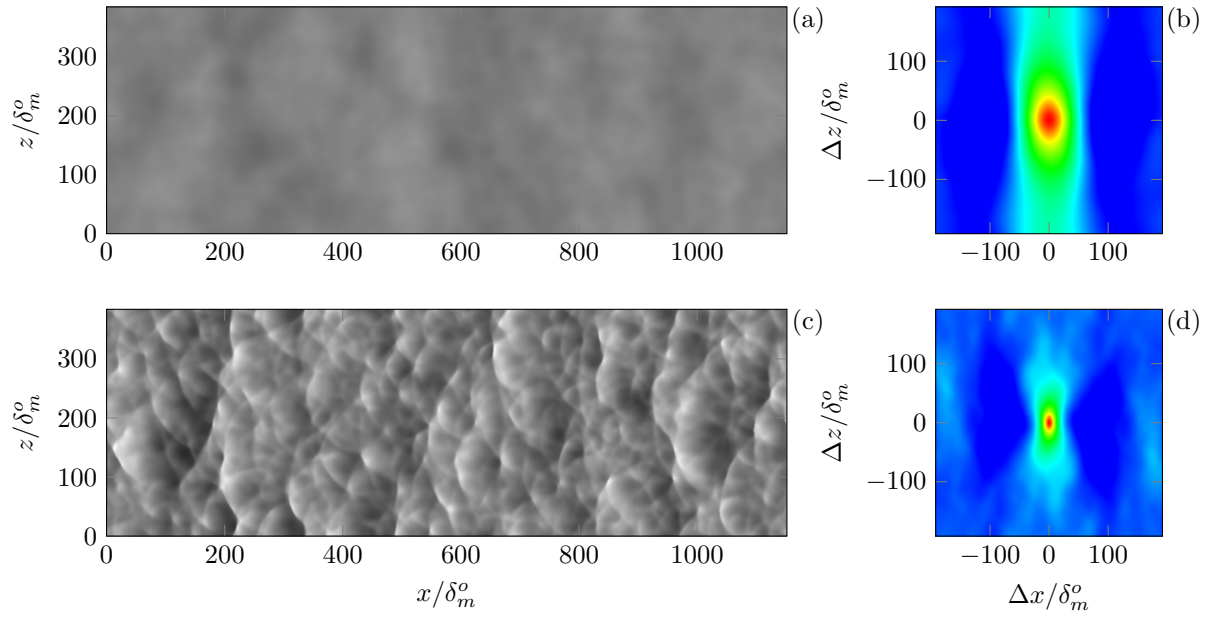

Figure 7.3: x-z plane of pressure fluctuations with gray-scale levels $-0.025 \leq p'/(\rho_\infty \Delta U^2) \leq 0.025$ at $y/\delta_m(t) = 10$ for (a) $M = 0.9$ and (c) 2.5. Normalized two-point correlation of pressure of (7.1) for (b) $M = 0.9$ and (d) 2.5. The correlation colormap ranges from -0.1 to 0.9.

Linear theory is understood to provide a phenomenological model of turbulent free-shear flows to describe some of their basic behaviors. To quantify the linear stability of our particular flows, we use the usual approach to linearize for ϵ-sized fluctuations of density, velocity, and pressure as

$$[\rho', u', v', w', p'] = \epsilon \mathrm{Re}\left\{[\hat{\rho}, \hat{u}, \hat{v}, \hat{w}, \hat{p}](y) \exp\left[\mathrm{i}(\alpha x + \beta z - \omega t)\right]\right\}, \tag{7.2}$$

superposed on a parallel base-flow, $[\bar{\rho}, \bar{u}, \bar{v}, \bar{w}, \bar{p}] = [\rho(y), u(y), 0, 0, p_\infty]$. The base-flow is assumed to have a tanh velocity profile with density set by the Crocco–Busemann relation (Sandham & Reynolds, 1990). This leads to an eigenvalue problem, which is solved numerically. An unstable (α,β) mode in (7.2) corresponds to exponential growth ($\mathrm{Im}(\omega) < 0$). The details of the equations and its method of solution are provided in detail in appendix C, and verified to be correct. Here we give an important result to support our use of linear theory and to emphasize the change in structural character of instability modes from low- to high-speed shear flows. Figure 7.4 shows the angle

$$\theta_m = \tan^{-1}\left(\frac{\beta}{\alpha}\right). \tag{7.3}$$

(The agreement with curve from Sandham & Reynolds (1990) in figure 7.4 verifies the accuracy of our eigenvalue solver). For $M \lesssim 1.2$ the most unstable mode is two-dimensional, $\theta_m = 0$, and the corresponding disturbance in (7.2) varies only in the streamwise direction. This behavior is similar to the predominately

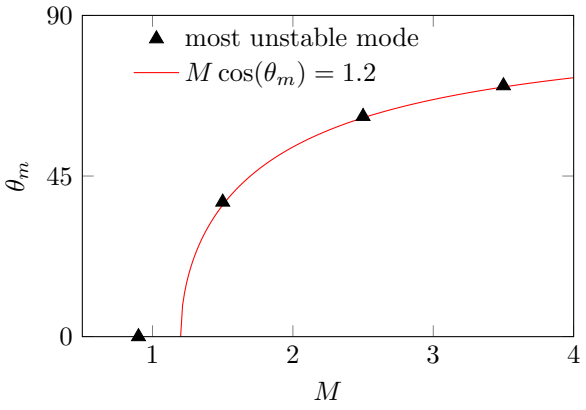

Figure 7.4: Angle of the most unstable three-dimensional mode with Mach number. The line is an empirical relation from Sandham & Reynolds (1990).

spanwise correlated structures in figure 7.1 (a), except the turbulence there has a broad range of scales most of which are three-dimensional. For $M \gtrsim 1.2$, the shear layer instability is most unstable to oblique modes (Lessen *et al.*, 1965; Jackson & Grosch, 1989; Sandham & Reynolds, 1990). Direct simulation of these modes support that remnants of these three-dimensional structures hold into the early nonlinear regime (Sandham & Reynolds, 1991).

We use the characteristics of these instabilities to examine whether or not the specific dynamics of large-scale oblique modes are at the core of the onset of the particular features of crackle noise, which initiate at about the same Mach number. In the next section, we add source terms to the governing equations for the $M = 2.5$ case to guide it toward a corresponding two-dimensional ($\theta_m = 0$) behavior, resembling the $M \lesssim 1.2$ cases, which are known to radiate crackle-free noise. This instability-wave based approach also has potential consequences for possibly mitigating crackle through control-induced structural modifications in the turbulence. The last section of this chapter shows how this adjusted turbulence structure affects the acoustics.

7.2 Altering the large-scale turbulence structure

Our intent is to adjust the geometric structure, in particular its spanwise correlation, without strongly disrupting the flow dynamics far from its natural turbulent state (i.e. a laminarization of the turbulence). Similar approaches that modify the flow equations have been used to understand flow phenomenology, for example, in the maintenance of turbulence near walls (Jimenez & Pinelli, 1999).

To alter the turbulence, we craft a source term that extracts energy from the unstable oblique Fourier

components, as predicted by linear theory, between $|y|/\delta_m(t) \leq \delta_{99}$:

$$N(\mathbf{q}) = -A \cdot \omega_i \cdot W(y) \begin{bmatrix} \rho(u-u_t) + u(\rho-\rho_t) \\ \rho(v-v_t) + v(\rho-\rho_t) \\ \rho(w-w_t) + w(\rho-\rho_t) \\ (\rho-\rho_t) \\ \frac{(p-p_t)}{(\gamma-1)} + \rho u_i(u_i-u_{i,t}) + \frac{1}{2}u_i u_i(\rho-\rho_t) \end{bmatrix} \tag{7.4}$$

where A the source strength, ω_i the growth rate of the most unstable mode, and $W(y)$ smoothly varies the source strength to zero outside of $|y|/\delta_m(t) < \delta_{99}$ by

$$W(y) = \frac{1}{2}\left\{\tanh\left[\frac{5}{\delta_m(t)}(y+\delta_{99})\right] - \tanh\left[\frac{5}{\delta_m(t)}(y-\delta_{99})\right]\right\}. \tag{7.5}$$

The terms $()_t$ in (7.4) are the target field. The solution vector of conservative variables in (7.4) is $\mathbf{q} = [\rho u, \rho v, \rho w, \rho, \rho e]^{\mathrm{T}}$. Each of the components of $\mathbf{q}$, which we designate generically as q, is Fourier transformed

$$\hat{q}_{k_x,k_z}(y) = \frac{1}{N_x N_z}\sum_{j=0}^{N_z-1}\sum_{k=0}^{N_x-1} q_{k,j}(y)\exp(-2\pi \mathrm{i} k_x k/N_x)\exp(-2\pi \mathrm{i} k_z j/N_z), \tag{7.6}$$

and its target is taken to be

$$\hat{q}_{\mathrm{t}}(k_x,k_z) = \begin{cases} 0, & k_x = k_1, k_z = |k_2| \quad \text{(damps targeted oblique)} \\ \hat{q}(k_x,k_z)\sqrt{\frac{E_{1,0}+E_{1,2}+E_{1,-2}}{E_{1,0}}}, & k_x = k_1, k_z = 0 \quad \text{(forces targeted 2-D mode)} \\ \hat{q}(k_x,k_z), & \text{otherwise} \quad \text{(leave other modes unchanged).} \end{cases} \tag{7.7}$$

The mode energy is $E_{i,j} = \hat{q}(k_i,k_j)\cdot\hat{q}^{\star}(k_i,k_j)$ where $()^{\star}$ indicates complex conjugate. The wavenumber pair $(k_1, \pm k_2)$ is the most unstable oblique mode-pair (supported by the discretization), predicted by linear theory, which for $M = 2.5$ is $(k1, \pm k2) = (0.289, \pm 0.537)\,\delta_m(t)$, which has a corresponding growth rate $\omega_i = (0.096)\,\Delta U/\delta_m(t)$. The coefficients in (7.7) are designed to conserve energy.

This evaluation can be made with more modest-scale simulations than the larger simulations discussed in chapter 2. The domain size is $(L_x \times L_y \times L_x) = (1536 \times 800 \times 192)\,\delta_m^o$, and it is discretized with uniformly $(N_x \times N_y \times N_z) = (1536 \times 801 \times 192)$ spaced grid points. Aside from the forcing (7.4), the numerical methods are the same as discussed in section 2.2. The turbulence is allowed to develop naturally until $\delta_m(t)/\delta_m^o = 5$. By design, forcing the solution to the two-dimensional target state yields two-dimensionally correlated structures as seen in figure 7.5.

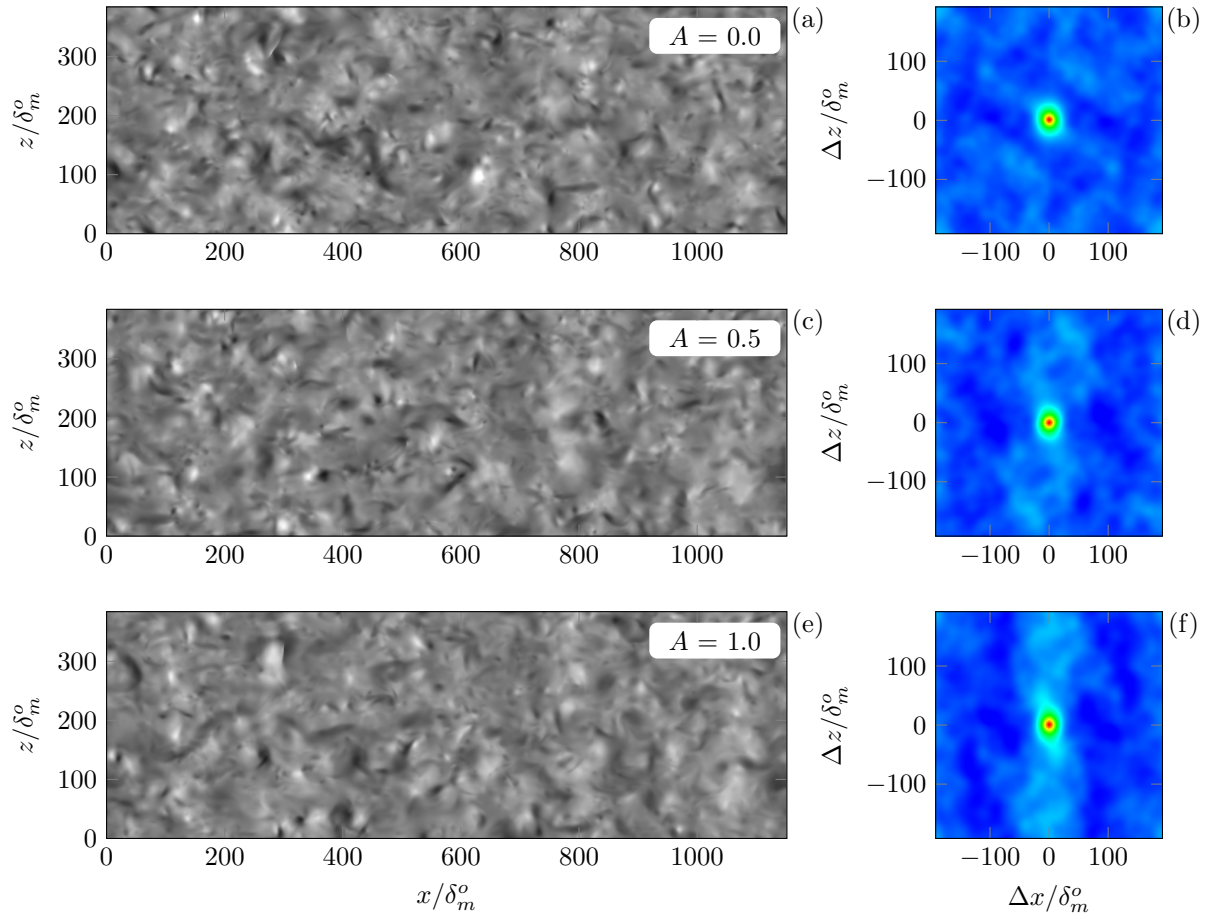

Figure 7.5: x-z plane of pressure fluctuations with gray-scale levels $-0.025 \leq p'/(\rho_\infty \Delta U^2) \leq 0.025$ at $y/\delta_m(t) = 10$ for (a) $A = 0.0$, (c) 0.5 and (e) 1.0. Normalized two-point correlation of pressure of (7.1) for (a) $A = 0.0$, (c) 0.5 and (e) 1.0. The correlation colormap ranges from -0.1 to 0.9.

The streamwise and spanwise integral length scales of pressure,

$$\frac{l_x(t)}{\delta_m^o} = \int_0^{L_x} C_{pp}(\Delta x, 0, t)\, d\Delta x, \tag{7.8}$$

$$\frac{l_z(t)}{\delta_m^o} = \int_0^{L_z} C_{pp}(0, \Delta z, t)\, d\Delta z, \tag{7.9}$$

are shown in figure 7.6. The spanwise integral lengths increase with the source amplitude throughout the simulation.

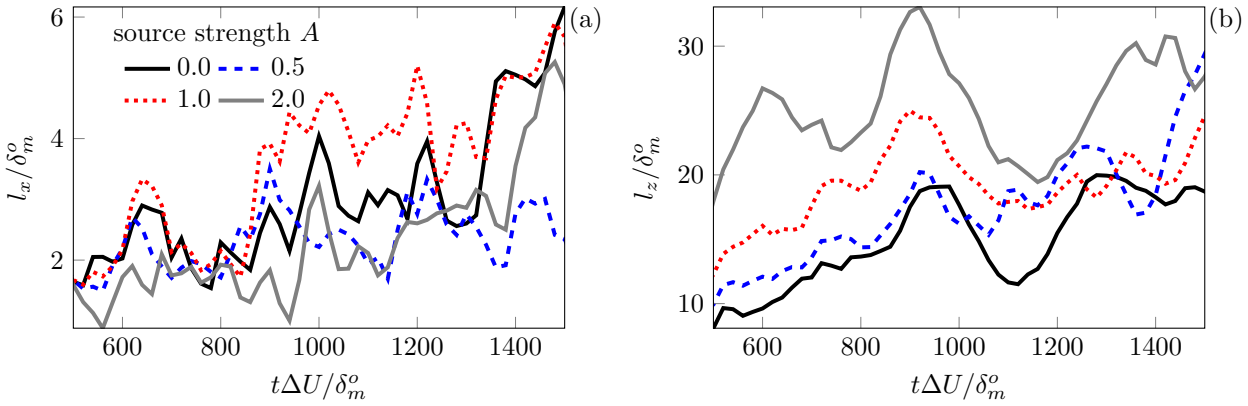

Figure 7.6: Effect of the source strength A on the integral lengths of pressure in the (a) streamwise and (b) spanwise directions.

We emphasize that the forcing is relatively weak: the pressure spectra in figure 7.7 are virtually unchanged by the forcing, though there is a slight but notable depletion in energy near $k = k_1$ due to (7.7). Overall, the development of the turbulence embodied in the modified equations in (7.4) has a similar broad range of scales compared to natural turbulence.

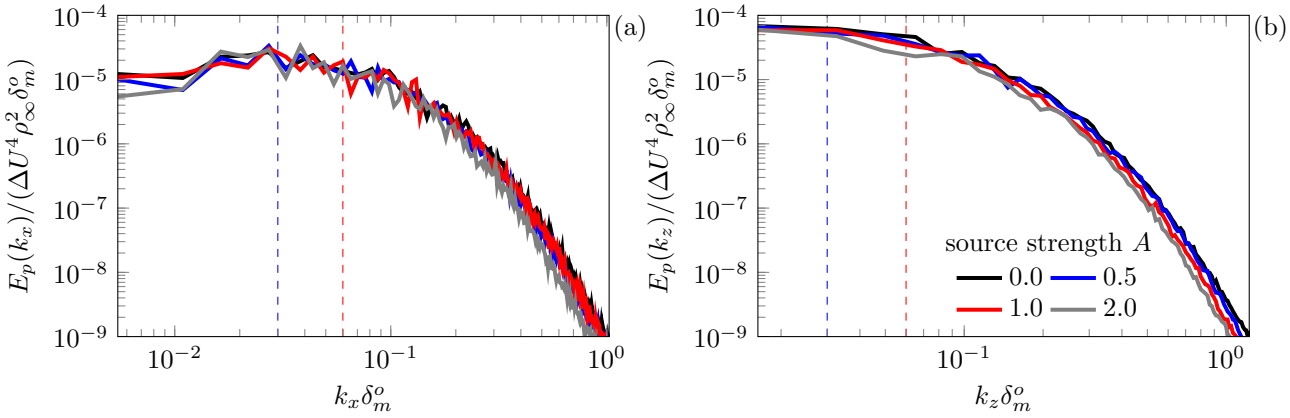

Figure 7.7: Effect of source strength A on the pressure spectra when $\delta_m(t)/\delta_m^o = 10$ at $y/\delta_m = 0$ in the (a) streamwise and (b) spanwise directions. The dashed curves correspond to the wavenumber that were modulated at the beginning and end of the forcing period.

Since the energy is suppressed from the most unstable oblique mode, it is anticipated that the shear layer growth rate will be affected. The growth rate has a modest decrease from $\dot{\delta_m} = 0.0066$ for strength $A = 0$ in (7.4) to 0.0042 at $A = 2$ between $\delta_m/\delta_m^o = 5$ to 10.

Despite these changes in the growth of the mixing layers, figure 7.8 shows the mean profiles remain indistinguishable, which plotted in similarity coordinates, means that the forcing will not significantly alter

the stability, aside from the direct effect of (7.4) on the amplification rates.

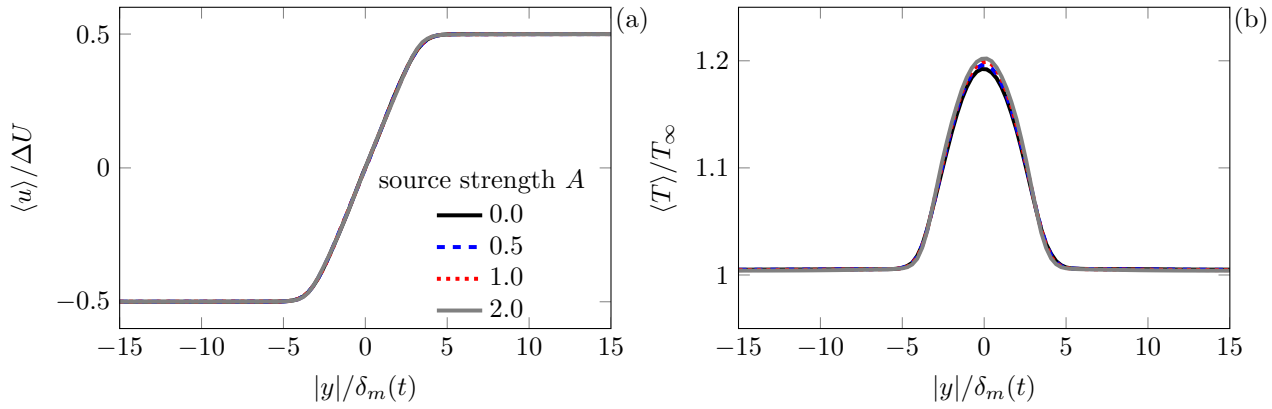

Figure 7.8: Effect of the source strength A on the mean flow profiles.

Figure 7.9 shows the Reynolds stresses are relatively insensitive to A for $A \lesssim 1$, though there is an modest increase in the intensity levels with A. Higher velocity intensities may have a potentially important effect on the pressure skewness.

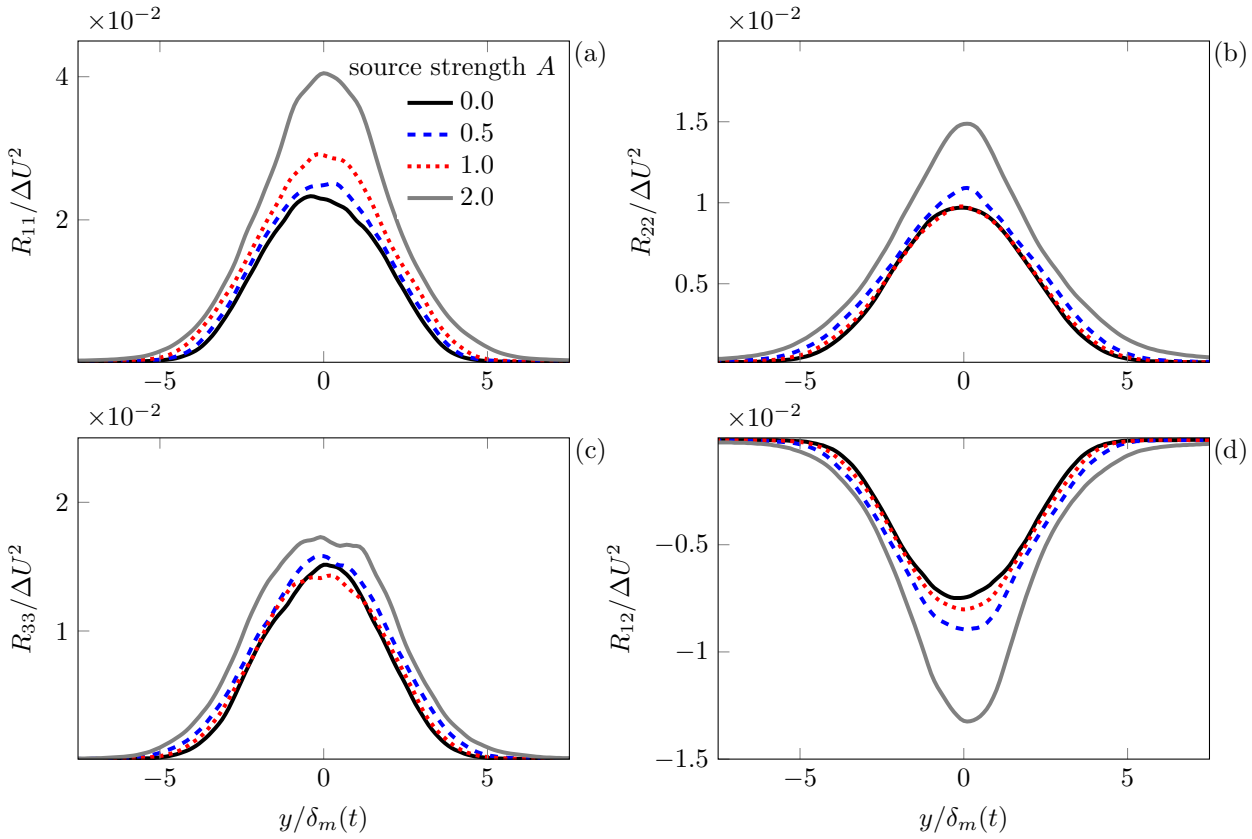

Figure 7.9: Effect of the source strength A on the Reynolds stresses.

We conclude that the turbulence structure has changed, especially its spanwise correlations, coming to more resemble a corresponding lower-Mach-number shear layer. This was quantified in figure 7.6. However, the overall flow dynamics were not strongly sensitive to the forcing. There are relatively mild changes observed in the spectra (figure 7.7), except for the wavenumbers specifically forced, and the mean flow development was essentially unchanged (figure 7.8). There is a small increase in the Reynolds stresses (figure 7.9). However, these quantitative changes are also anticipated to have a small effect relative to the qualitative changes to the turbulence structures. We shall see that the visualizations of the sound field show perhaps the greatest change in structure. We note that the amplitude $A = 2$ seemed to be measurably more disruptive than the $A = 1$ source strength, though both increased the two-dimensional character of the turbulence, so we will focus particularly on $A = 1$ in the subsequent analysis of the corresponding sound field.

7.3 Effect on the pressure statistics

Figure 7.10 shows that the sound fundamentally changes its structures for $A = 1$. Spanwise dominated pressure waves are obviously more intense, and even these waves are still curved and have local patterns that cross each other in a similar pattern to those in the unmodified turbulence.

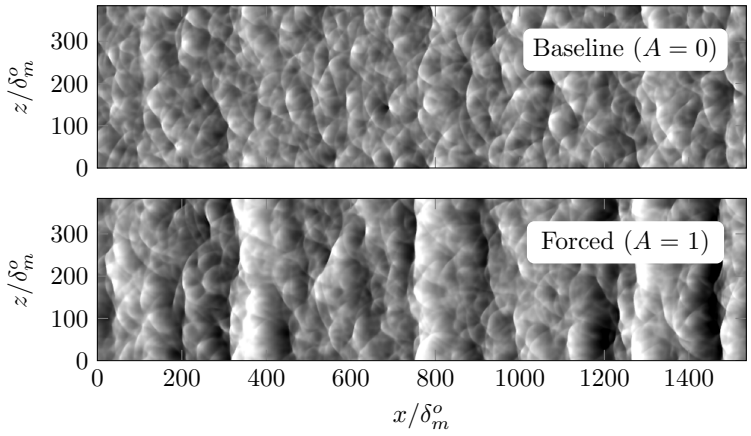

Figure 7.10: Effect of the source strength on the x-z plane of pressure $-0.025 < p'/(\Delta U^2 \rho_\infty) < 0.025$ for $M = 2.5$ at $y/\delta_m(t) = 10$ when $\delta_m(t)/\delta_m^o = 10$.

Figure 7.11 (a) shows the increase in sound intensity with source strength. At $y/\delta_m = 10$, for example, the noise level for the $A = 2$ amplitude is nearly two times louder than the unmodified flow. That this correlation might lead to greater acoustic efficiency is not unexpected, and has been anticipated in regard to the noise of high-speed shear flows by Ffowcs Williams & Maidanik (1965) who showed that the eddy correlation volume is proportional to its radiated acoustic intensity. This factor contributes to the increase in acoustic intensity due to the eddy elongation from Mach number effects (Ffowcs Williams & Maidanik, 1965).

However, there is a far more modest effect on S_k, as shown in figure 7.11 (b). There is an increase of 7% for $A > 0$, but appears to be insensitive to A for $A > 0$ beyond $y/\delta_m > \delta_{99}$. The average skewness above the mixing layer, $y > \delta_{99}$, for $A = 0$, 0.5, 1, and 2 is $\langle S_k \rangle_{y>\delta_{99}} = 0.456$, 0.466, 0.483, and 0.485, respectively. Despite the strong increase in the velocity intensities especially for $A = 2$ as shown in figure 7.9, where conventional wisdom would suggest that higher intensities would enhance compressive nonlinearity and drive up S_k, skewness is relatively insensitive to the source amplitude. The primary result is that the adjustments to the turbulence geometry by the (7.4) forcing does not significantly affect S_k despite the obvious structural

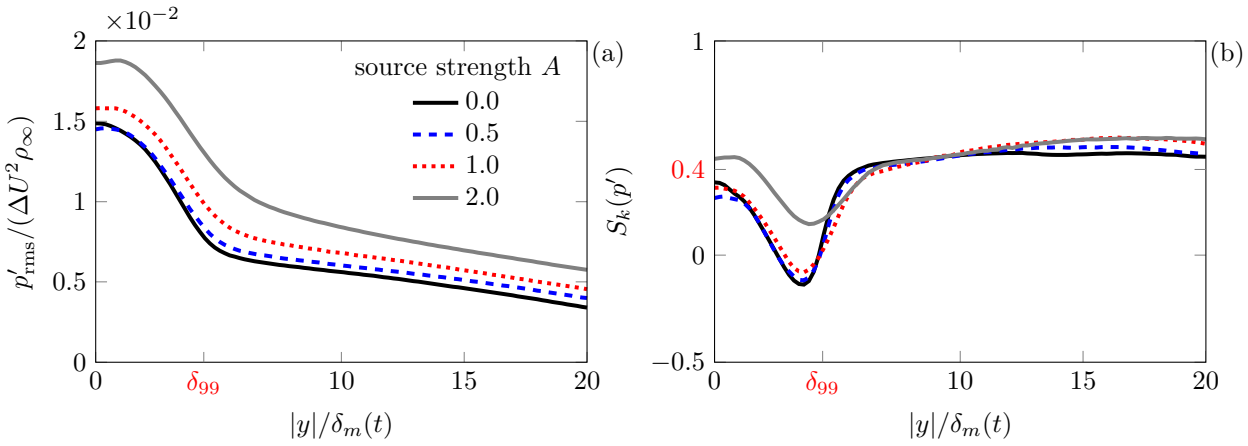

Figure 7.11: Effect of source strength A on the (a) pressure intensity and (b) pressure skewness.

changes. This suggest that the more oblique structure of the turbulence is not a prerequisite to radiation with $S_k > 0$. Rather, finite S_k in high-speed flows is likely a nonlinear compressibility effect from the supersonic flow adjacent to finite-amplitude disturbances of these large scales. Such a mechanism was described in chapter 6.

Chapter 8

Concluding remarks

8.1 Research summary

The DNS of temporally-developing shear layers were primarily used to study the turbulent interactions and acoustics leading to pressure skewness,

$$S_k(p') \equiv \frac{\overline{(p')^3}}{\overline{(p')^2}^{3/2}} \gtrsim 0.4, \tag{8.1}$$

and thus nominally jet crackle. This was notable for $M \gtrsim 2.5$, in which case, the pressure beyond the mixing layer has the hallmark of crackle: sharp compressions followed by weaker, rounded expansions. Thus, the simulations reproduce the key aspects of crackle observed near jet turbulence.

Consistent with experiments, crackle depends on the flow Mach number. S_k increases rapidly between $1 \lesssim M \lesssim 2.5$, and it is less sensitive M for $M \gtrsim 2.5$. The current simulations, however, show smaller S_k from those observed in experiments on jets at the same Mach number. We showed that this in not just a function of the planar, temporally-developing configuration we consider, but instead is due to the spatial structure of the sound near the jets, which depends on the downstream position, angle, and distance from the source.

Crackle is insensitive over the propagation distances simulated in the DNS. However, nonlinear wave–wave interactions above the turbulence are evident. In particular, wave merging reduces the number of distinct waves by 50% over 20 momentum thicknesses (δ_m). A detailed budget accounting for the factors that transport S_k showed that this S_k insensitivity with distance represents a balance of nonlinear interactions, which increase S_k, and the molecular effects, which decrease the pressure amplitude asymmetry and thus S_k. This suggests that origin of skewness is best viewed as a source effect rather than propagation effect.

Simulations at different $Re_{\delta_m^o}$ show that S_k is robust to Reynolds number. S_k observations were also robust to the structure of the large-scale turbulence, which were modified by a novel forcing designed to excite low-speed-like large-scale turbulence in the higher-speed flows. The S_k was essentially unchanged,

even when the structures themselves where significantly adjusted. This supports that S_k is linked to the compressibility of the flow at the source, rather than to any particular features of its three-dimensional structure.

Weakly nonlinear gas dynamics models provide a fundamental explanation of the source mechanism of S_k: the pressure asymmetry is formed from a nonlinear compressive effect. In particular, the supersonic flow adjacent to a wavy-wall-like surface leads to positive S_k, immediately at the source. In this model, S_k propagates from the source unchanged, with the three-dimensional wave pattern and pressure traces remarkably similar to those above the turbulent mixing layers. Even without the turbulence dynamics, this model embodies the essential elements of crackle and supports that S_k is a source effect which depends primarily on the flow Mach number.

Modifications to the turbulence source and the wavy-wall model also showed that skewness is insensitive to stronger structures in its source. Though weaker structures tended to reduce S_k, its sensitivity to source strength suggest that the gas dynamic nonlinearity is not a perpetual effect.

8.2 Future work

8.2.1 Temperature effects on S_k

Experimental observations indicate that crackle depends on the ratio of jet temperature (T_j) to the ambient temperature (T_∞) (Krothapalli *et al.*, 2000), which introduces another nondimensional group potentially affecting S_k,

$$\kappa_T = \frac{T_j}{T_\infty}. \tag{8.2}$$

An increase in κ_T broadens the spectrum of unstable modes (Tam & Hu, 1989; Samanta, 2016) of free-shear layers. This effect has implications for the dynamically important modes within the turbulence which potentially affect S_k. The current simulation approach can be extended to enforce a temperature ratio across the shear layers to assess its affect. We note that the combined effect of jet heating with flow speed can be grouped in a generalized Mach number

$$M_{co} = \frac{U_j + 1}{1 + \sqrt{\frac{1}{\kappa_T}}}, \tag{8.3}$$

which has been shown to be a useful grouping to collapse experimental data with different temperature ratios (Oertel, 1979). If the heating effect is captured by (8.3), then the range of M and thus M_{co} simulated in the DNS has already provided the anticipated trend of S_k over a significant range of M-κ_T as shown in figure 8.1. The near-field LES data for a range of temperature ratios ($\kappa_T = 1.25$ to 1.32) appear to follow

the trend in the current, unheated DNS with the parameters nondimensionalized by (8.3). Future DNS with different κ_T can confirm this trend and assess its sensitivity to κ_T.

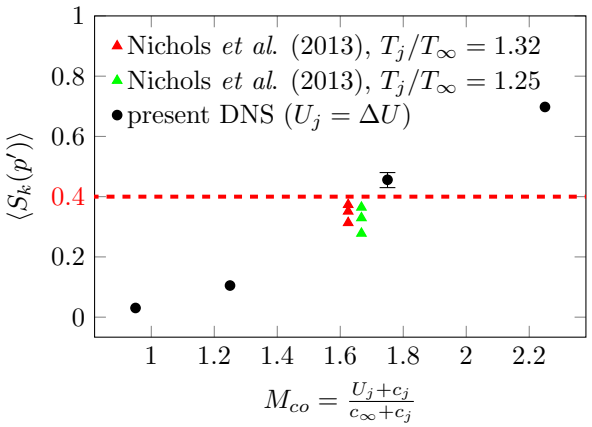

Figure 8.1: Pressure skewness with M_{co}.

8.2.2 Exploration of control strategies through simulation

In some sense, there is little do to: S_k is insensitive to the changes in the turbulence structures and to its strong levels. S_k is primarily linked to its M. Though control strategies (*e.g.* jet nozzle modification, water-droplet injection, co-flow) lower crackle and noise levels radiated from high-speed jets (Papamoschou & Debiasi, 2001; Krothapalli *et al.*, 2003*b*; Greska, 2005), a clear understanding of the leading physical factors and their combined effects is lacking. Experiments demonstrate the viability to lower S_k, yet only provide modest diagnostics to indicate the mechanisms. This limits the possibility of harnessing their mixed effects to reduce crackle below expected levels.

Beyond the baseline flow turbulence, multiphysics effects, like water-droplet injection, provide additional source mechanisms that can reduce noise and crackle (Krothapalli *et al.*, 2003*b*; Greska, 2005). Simulations and computer hardware have enabled realistic-scale predictions of this kind, and they provide the entire space-time database to understand the leading effects. We have shown that the temporally-developing turbulence generates S_k like those observed near jet turbulence. We can use these configurations, including the two-way coupled effects of particles, as a model of water droplets in the near-nozzle shear layers to examine the physical mechanisms leading to S_k reduction.

8.2.3 Minimum crackle levels in turbulent flows

Adjoint-based methods provide a route to inform optimal control strategies for crackle. Similar techniques have been used to optimize airfoil shapes (Jameson *et al.*, 1998). They have also been used to control

turbulent boundary layers (Bewley *et al.*, 2001). They have likewise been demonstrated for aeroacoustic reductions in model (Wei & Freund, 2006) and turbulent (Kim *et al.*, 2014) shear flows (Freund, 2011). Adjoint-based methods provide a gradient of a cost functional, which for crackle reduction we would take as $S_k(p')$. For an arbitrarily large number of control and input parameters, the gradient provides the direction to reduce S_k. The sensitivity in the gradient also points to the leading factors for its reduction.

Appendix A

Numerics

This chapter provides additional details regarding the methods of numerical simulations. This family of numerics, with slight modifications in places, has been successful in aeroacoustic simulations of this kind (Kleinman & Freund, 2008; Kim *et al.*, 2014).

A.1 Finite-difference first derivative

The approximation of the first derivative at x_o can be written as

$$\frac{\partial}{\partial x} f(x_o) \approx \sum_{i=-M}^{M} b_i f'(x_o + i\Delta x) = \frac{1}{\Delta x} \sum_{j=-N}^{N} a_j f(x_o + j\Delta x), \tag{A.1}$$

where the coefficients are assumed to have symmetry $b_i = b_{-i}$ and $a_i = -a_{-i}$. The coefficients are determined by matching terms in the Taylor series substituted in (A.1). Others (Tam & Webb, 1993; Bogey & Bailly, 2004) have used a combined approach to determine the coefficients; the truncated Taylor series approximation is used to enforce a desired order of accuracy, and the remaining coefficients are determined by minimizing some measure of the error between the exact and approximate dispersion relation. The properties of the scheme then preserve aspects of the dispersion properties of the derivative. For an explicit ($m = 0$) 7-point stencil ($n = 3$) each of the terms in finite difference expression is written as a Taylor series expansion up to $O(\Delta x^6)$ by

$$
\begin{aligned}
f_{j+1} &\sim f_j + f'_j\Delta x + \frac{f''_j}{2!}(\Delta x)^2 + \frac{f'''_j}{3!}(\Delta x)^3 + \frac{f''''_j}{4!}(\Delta x)^4 + \frac{f'''''_j}{5!}(\Delta x)^5 + \dots \\
f_{j-1} &\sim f_j - f'_j\Delta x + \frac{f''_j}{2!}(\Delta x)^2 - \frac{f'''_j}{3!}(\Delta x)^3 + \frac{f''''_j}{4!}(\Delta x)^4 - \frac{f'''''_j}{5!}(\Delta x)^5 + \dots \\
f_{j+2} &\sim f_j + f'_j 2\Delta x + \frac{f''_j}{2!}(2\Delta x)^2 + \frac{f'''_j}{3!}(2\Delta x)^3 + \frac{f''''_j}{4!}(2\Delta x)^4 + \frac{f'''''_j}{5!}(2\Delta x)^5 + \dots \\
f_{j-2} &\sim f_j - f'_j 2\Delta x + \frac{f''_j}{2!}(2\Delta x)^2 - \frac{f'''_j}{3!}(2\Delta x)^3 + \frac{f''''_j}{4!}(2\Delta x)^4 - \frac{f'''''_j}{5!}(2\Delta x)^5 + \dots \\
f_{j+3} &\sim f_j + f'_j 3\Delta x + \frac{f''_j}{2!}(3\Delta x)^2 + \frac{f'''_j}{3!}(3\Delta x)^3 + \frac{f''''_j}{4!}(3\Delta x)^4 + \frac{f'''''_j}{5!}(3\Delta x)^5 + \dots \\
f_{j-3} &\sim f_j - f'_j 3\Delta x + \frac{f''_j}{2!}(3\Delta x)^2 - \frac{f'''_j}{3!}(3\Delta x)^3 + \frac{f''''_j}{4!}(3\Delta x)^4 - \frac{f'''''_j}{5!}(3\Delta x)^5 + \dots
\end{aligned}
$$

Substituting these relations into the differencing equation (A.1) and matching like terms, the constraint equations that enforce the convergence rate to sixth order are

$$
\begin{aligned}
a_0 &= 0 && \text{(A.2)} \\
2a_1 + 4a_2 + 6a_3 &= 1 \text{ (second order)} && \text{(A.3)} \\
\frac{2}{3!}a_1 + \frac{2\cdot 2^3}{3!}a_2 + \frac{2\cdot 3^3}{3!}a_3 &= 0 \text{ (fourth order)} && \text{(A.4)} \\
\frac{2}{5!}a_1 + \frac{2\cdot 2^5}{5!}a_2 + \frac{2\cdot 3^5}{5!}a_3 &= 0 \text{ (sixth order).} && \text{(A.5)}
\end{aligned}
$$

Directly solving of equations (A.3)-(A.5) results the standard sixth-order approximation with coefficients

$$
\begin{aligned}
a_0 &= 0 \\
a_1 &= -a_{-1} = \tfrac{3}{4} \\
a_2 &= -a_{-2} = -\tfrac{3}{20} \\
a_3 &= -a_{-3} = \tfrac{1}{60}.
\end{aligned}
$$

To this point, there is nothing constraining the method, except in the limit of $\Delta x \to 0$. Resolution is a means of measuring accuracy at finite resolution, and it can be quantified by the adherence to the exact dispersion relation of the method. To obtain a resolution-optimized fourth-order method for example, relations (A.3)

and (A.4) are enforced leaving one free-parameter. A useful scheme involves an optimization in Fourier space. The scheme can be written in Fourier space by substituting the inverse discrete Fourier transform.

$$\sum_{i=-m}^{m} b_i \mathrm{i}k\hat{f}(k)\exp\left[\mathrm{i}k(x+i\Delta x)\right] = \frac{1}{\Delta x}\sum_{j=-n}^{n} a_j \hat{f}(k)\exp\left[\mathrm{i}k(x+j\Delta x)\right], \tag{A.6}$$

and cancelling $\hat{f}(k)\exp\left[\mathrm{i}k(x)\right]$ from both sides we have

$$\sum_{i=-m}^{m} b_i \mathrm{i}k\exp\left[\mathrm{i}k(i\Delta x)\right] = \frac{1}{\Delta x}\sum_{j=-n}^{n} a_j \exp\left[\mathrm{i}k(j\Delta x)\right]. \tag{A.7}$$

Isolating $k\Delta x$ on the left-hand-side

$$k\Delta x = \frac{-\mathrm{i}\sum\limits_{j=-n}^{n} a_j \exp\left[\mathrm{i}k(j\Delta x)\right]}{\sum\limits_{i=-m}^{m} b_i \exp\left[\mathrm{i}k(i\Delta x)\right]} \tag{A.8}$$

and recalling Euler's formula

$$\cos(x) = \frac{\exp(\mathrm{i}x)+\exp(-\mathrm{i}x)}{2}$$
$$\sin(x) = \frac{\exp(\mathrm{i}x)-\exp(-\mathrm{i}x)}{2\mathrm{i}},$$

the effective wavenumber equation is

$$(k\Delta x)' = \frac{2\sum\limits_{j=1}^{n} a_j \sin(jk\Delta x)}{b_o + 2\sum\limits_{i=1}^{m} b_i \cos(ik\Delta x)}. \tag{A.9}$$

The explicit finite-difference ($m = 0$) equation approximates the first derivative as a truncated sine series in Fourier space. A real-valued expression for (A.9) is a consequence that the coefficients were symmetric; otherwise the dispersion relation would be complex. The $(k\Delta x)'$ notation in equation A.9 denotes an approximation to the exact wavenumber relation $(k\Delta x)$.

To better represent the exact dispersion relation, the integral error,

$$E = \int_{\ln(a)}^{\ln(b)} \left[(k\Delta x) - (k\Delta x)'\right]^2 d\ln(k\Delta x), \tag{A.10}$$

between the exact and effective wavenumber will be minimized. The limits of integration for a seven-point

$n = 3$ scheme is $a = \pi/16$ and $b = \pi/2$. The thirteen-point schemes uses $a = \pi/16$ and $b = 3\pi/5$. For the fourth-order $n = 3$ scheme, the final constraint that optimizes the integral error is

$$\frac{\partial E}{\partial a_3} = 0. \tag{A.11}$$

Figure A.2 shows the effective wavenumber and associated error with respect to the exact relation. By sacrificing order of accuracy for resolution, the optimized formulas (abbreviated opt.) have more error in the low-wavenumber range. The standard schemes (abbreviated std.) have coefficients that maximize formal order of accuracy. For the seven-point $n = 3$, fourth-order resolution optimized scheme the coefficients are

$$\begin{aligned} a_0 &= 0 \\ a_1 &= -a_{-1} = 0.824639848382100 \\ a_2 &= -a_{-2} = -0.209711878705680 \\ a_3 &= -a_{-3} = 0.0315946363430865. \end{aligned}$$

The coefficients for the $n = 6$ (13-pt), fourth-order, resolution optimized scheme are

$$\begin{aligned} a_0 &= 0 \\ a_1 &= -a_{-1} = 0.9108405208695360 \\ a_2 &= -a_{-2} = -0.3419538377082619 \\ a_3 &= -a_{-3} = 0.1380399894807369 \\ a_4 &= -a_{-4} = -0.04827039810294327 \\ a_5 &= -a_{-5} = 0.008624243759248696 \\ a_6 &= -a_{-6} = -0.0006681390707308727. \end{aligned}$$

Near-boundary points use reduced-order central differences as described in Freund (1997*a*). On the boundaries a third-order one-sided approximation is used.

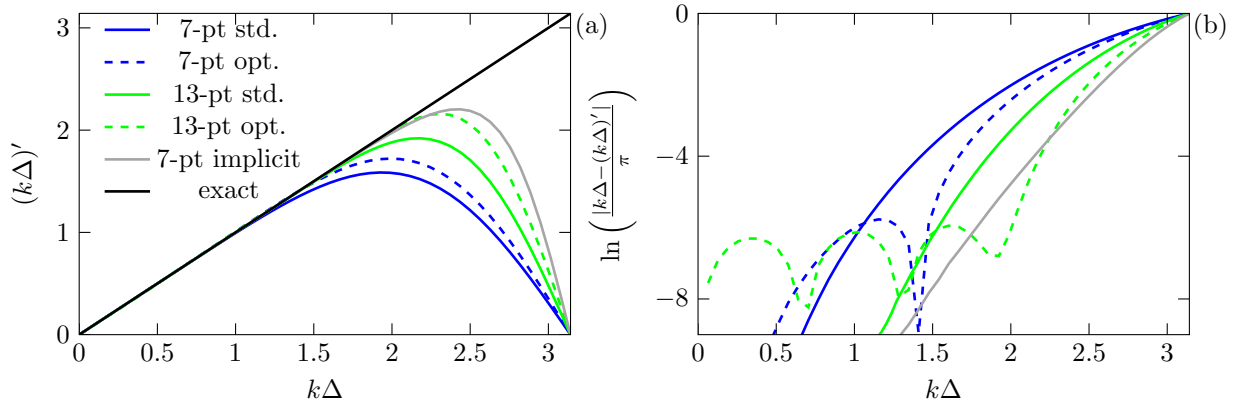

Figure A.1: (a) Effective wavenumber of the interior first derivative and (b) the difference from the exact.

A.2 Finite-difference second derivative

The explicit finite difference approximation of the second derivative is given by

$$\frac{\partial^2}{\partial x^2} f(x_o) \approx f''(x_o) = \frac{1}{(\Delta x)^2} \sum_{j=-N}^{N} c_j f(x_o + j\Delta x), \tag{A.12}$$

with constraint equations for $n = 3$ on coefficients enforcing formal order of accuracy up to sixth-order by

$$\begin{aligned}
c_0 + 2c_1 + 2c_2 + 2c_3 &= 0 && \text{(A.13)}\\
\frac{2}{2!}c_1 + \frac{2\cdot 2^2}{2!}c_2 + \frac{2\cdot 3^2}{2!}c_3 &= 1 \text{ (second order)} && \text{(A.14)}\\
\frac{2}{4!}c_1 + \frac{2\cdot 2^4}{4!}c_2 + \frac{2\cdot 3^4}{4!}c_3 &= 0 \text{ (fourth order)} && \text{(A.15)}\\
\frac{2}{6!}c_1 + \frac{2\cdot 2^6}{6!}c_2 + \frac{2\cdot 3^6}{6!}c_3 &= 0 \text{ (sixth order).} && \text{(A.16)}\\
& && \text{(A.17)}
\end{aligned}$$

Directly solving equations (A.13)-(A.16) results in the standard sixth-order scheme with coefficients

$$\begin{aligned}
c_0 &= -\tfrac{49}{18}\\
c_1 &= c_{-1} = \tfrac{3}{2}\\
c_2 &= c_{-2} = -\tfrac{3}{20}\\
c_3 &= c_{-3} = \tfrac{1}{90}.
\end{aligned}$$

Substituting the discrete Fourier representation of the function in (A.20), a modified wavenumber expression for the explicit finite-difference approximation of the second derivative is

$$(k\Delta x)'' = c_o + 2\sum_{j=1}^{N} c_j \cos(j\Delta x). \tag{A.18}$$

The modified wave number approximates the exact dispersion relation by a truncated cosine series. The square error between the exact and effective wavenumber on a scaled periodic domain $[0, \pi)$ is given by

$$E = \int_{\ln(a)}^{\ln(b)} \left[(k\Delta x)^2 - (k\Delta x)''\right]^2 d\ln(k\Delta x), \tag{A.19}$$

where the bounds of integration for the seven-point scheme here are $a = \pi/16$ and $b = \pi/2$. For a thirteen-point scheme $a = \pi/16$ and $b = 3\pi/5$. Figure A.2 gives the modified wave number and error associated with seven-point and thirteen-point schemes of the second derivative. Like the first derivative, the optimized methods, by sacrificing maximum accuracy for resolution, lower wavenumbers error is increased. The

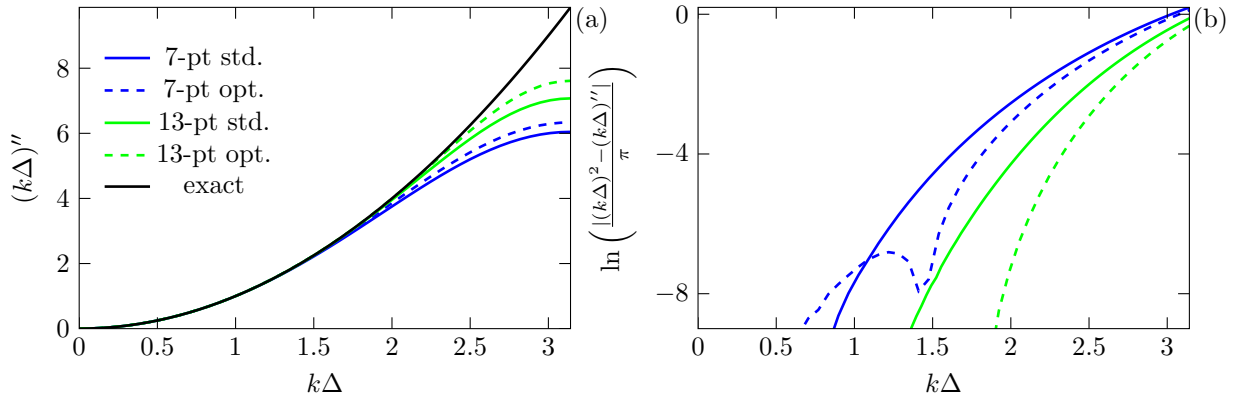

Figure A.2: (a) Effective wavenumber of the interior second derivative and (b) the difference from the exact.

coefficients for the resolution optimized $n = 3$ and $n = 6$ schemes are

$$\begin{aligned} c_0 &= -2.81321312844389 \\ c_1 &= c_{-1} = 1.56824317966625 \\ c_2 &= c_2 = -.177297271866500 \\ c_3 &= c_3 = 0.0156606564221945 \end{aligned}$$

and

$$\begin{aligned} c_0 &= -3.093268941798102 \\ c_1 &= c_{-1} = 1.811759211319885 \\ c_2 &= c_2 = -.3343827021872651 \\ c_3 &= c_3 = 0.08734940331848545 \\ c_4 &= c_4 = -0.02186933368500581 \\ c_5 &= c_5 = 0.004224346387577600 \\ c_6 &= c_6 = -0.0004464542546261400, \end{aligned}$$

respectively. Near-boundary points use reduced-order central differences. For $i = 2$, $i = N - 2$, a standard fourth-order method is used with coefficients

$$\begin{aligned} c_0 &= -2 \\ c_1 &= a_{-1} = 1. \end{aligned}$$

For $i = 1$, $i = N_i - 1$, second-order scheme is used with coefficients

$$\begin{aligned} c_0 &= \tfrac{-5}{2} \\ c_1 &= c_{-1} = \tfrac{4}{3} \\ c_2 &= c_{-2} = -\tfrac{1}{12}. \end{aligned}$$

On the boundaries, a one-sided, third-order method is used where the coefficients at $i = 1$ are given by

$$\begin{aligned} c_0 &= 2 \\ c_1 &= -5 \\ c_2 &= 4 \\ c_2 &= -1. \end{aligned}$$

A.3 Selective high-wave number filtering

It may be necessary to apply a selective high-wave number filtering to the solution so that parasitic, short-wavelength waves do not grow and deteriorate the solution. The differencing equation is similar to Bogey & Bailly (2004) given here as

$$\tilde{f}(x_o) = f(x_o) - \sum_{j=-N}^{N} h_j f(x_o + j\Delta x). \tag{A.20}$$

For a thirteen-point ($n = 6$) scheme and assuming $h_i = h_{-1}$, the constraint equations of formal order of accuracy are written

$$\begin{aligned}
1 - (h_o + 2h_1 + 2h_2 + 2h_3 + 2h_4 + 2h_5 + 2h_6) &= 1 && \text{(A.21)}\\
-\left(\frac{2}{2!}h_1 + \frac{2\cdot 2^2}{2!}h_2 + \frac{2\cdot 3^2}{2!}h_3 + \frac{2\cdot 4^2}{2!}h_4 + \frac{2\cdot 5^2}{2!}h_5 + \frac{2\cdot 6^2}{2!}h_6\right) &= 0 \text{ (second order)} && \text{(A.22)}\\
-\left(\frac{2}{4!}h_1 + \frac{2\cdot 2^4}{4!}h_2 + \frac{2\cdot 3^4}{4!}h_3 + \frac{2\cdot 4^4}{4!}h_4 + \frac{2\cdot 5^4}{4!}h_5 + \frac{2\cdot 6^4}{4!}h_6\right) &= 0 \text{ (fourth order)} && \text{(A.23)}\\
-\left(\frac{2}{6!}h_1 + \frac{2\cdot 2^6}{6!}h_2 + \frac{2\cdot 3^6}{6!}h_3 + \frac{2\cdot 4^6}{6!}h_4 + \frac{2\cdot 5^6}{6!}h_5 + \frac{2\cdot 6^6}{6!}h_6\right) &= 0 \text{ (sixth order)} && \text{(A.24)}\\
-\left(\frac{2}{8!}h_1 + \frac{2\cdot 2^8}{8!}h_2 + \frac{2\cdot 3^8}{8!}h_3 + \frac{2\cdot 4^6}{6!}h_4 + \frac{2\cdot 5^6}{6!}h_5 + \frac{2\cdot 6^6}{6!}h_6\right) &= 0 \text{ (eigthth order)} && \text{(A.25)}\\
-\left(\frac{2}{10!}h_1 + \frac{2\cdot 2^{10}}{10!}h_2 + \frac{2\cdot 3^{10}}{10!}h_3 + \frac{2\cdot 4^{10}}{10!}h_4 + \frac{2\cdot 5^{10}}{10!}h_5 + \frac{2\cdot 6^{10}}{10!}h_6\right) &= 0 \text{ (tenth order)} && \text{(A.26)}\\
-\left(\frac{2}{12!}h_1 + \frac{2\cdot 2^{12}}{12!}h_2 + \frac{2\cdot 3^{12}}{12!}h_3 + \frac{2\cdot 4^{12}}{12!}h_4 + \frac{2\cdot 5^{12}}{12!}h_5 + \frac{2\cdot 6^{12}}{12!}h_6\right) &= 0 \text{ (twelfth order).} && \text{(A.27)}
\end{aligned}$$

A transfer function in wavenumber space can be found, much like the modified wavenumbers of the derivative approximations. For the explicit formulas used here, the transfer function is

$$T(k\Delta) = 1 - \left(h_o + 2\sum_{j=1}^{N} h_j \cos(j\Delta x)\right), \tag{A.28}$$

and the square integral error between the filtered and un-filtered solutions is

$$E = \int_{\ln(a)}^{\ln(b)} \left[1 - T(k\Delta x)\right]^2 d\ln(k\Delta x), \tag{A.29}$$

where the limits of integration for the seven-point are $a = \pi/16$ and $b = 3\pi/32$. For the thirteen-point formulas the limits are $a = \pi/16$ and $b = \pi/2$. The coefficients for the seven- and thirteen-point formulas

by minimizing (A.29) are given as

$$\begin{aligned} h_0 &= 0.288090709024785 \\ h_1 &= h_{-1} = -.228272677256196 \\ h_2 &= h_{-2} = 0.105954645487608 \\ h_3 &= h_{-3} = -0.02172732274380381 \end{aligned}$$

and

$$\begin{aligned} h_0 &= 0.1913963126291382 \\ h_1 &= h_{-1} = -0.1719104977994496 \\ h_2 &= h_{-2} = 0.1237396648728178 \\ h_3 &= h_{-3} = -0.06976715092480617 \\ h_4 &= h_{-4} = 0.02936617293645158 \\ h_5 &= h_{-5} = -0.008322351275744250 \\ h_6 &= h_{-6} = 0.001196005876161525, \end{aligned}$$

respectively.

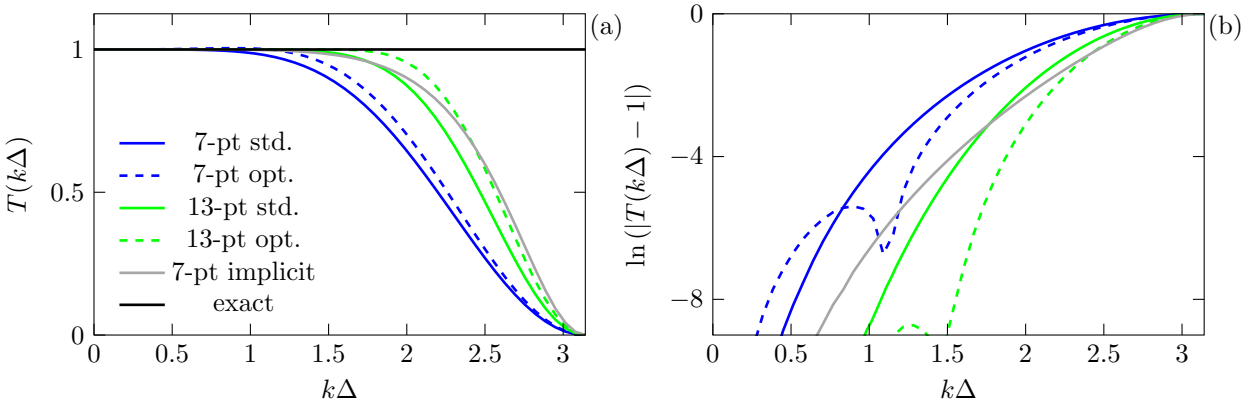

Figure A.3: (a) Transfer function of the interior high-wavenumber filter and (b) the difference from the exact.

When an implicit filtering scheme is desired, the finite difference equation can be written as

$$\sum_{i=-M}^{M} g_i \tilde{f}(x_o + i\Delta x) = \sum_{j=-N}^{N} h_j f(x_o + j\Delta x), \tag{A.30}$$

and the same process as described above for selecting the stencil width, formal order of accuracy, and enforcing an effective wavenumber behavior is carried out. Following Lele (1992), the resolution behavior in wavenumber space is set differently than Tam & Webb (1993); Bogey & Bailly (2004). Values of $T(k\Delta)$ at a particular $k\Delta$ to find the remaining degrees of freedom of the stencil formula. The behavior at $k\Delta = \pi$ is also set to

$$\frac{d^2T(k\Delta)}{d^2k\Delta}(\pi) = 0. \tag{A.31}$$

Though this approach does not minimize the integral square difference between the actual and effective wave number resolution, the resolution properties are well-known and have not shown any negative effects on the solution. The trends for the seven-point implicit scheme (C.2.10.b) designed by Lele (1992) are given in figure A.3. The coefficients reported by Lele (1992) are

$$\begin{aligned} g_0 &= 1 \\ g_1 &= 0.451403074913670 \\ g_2 &= 0.0326996130846655 \\ h_0 &= 0.949189663643128 \\ h_1 &= h_{-1} = 0.489510827181324 \\ h_2 &= h_{-2} = 0.0174565121776038 \\ h_3 &= h_{-3} = 0.00254051681784360, \end{aligned} \tag{A.32}$$

though they have been scaled to be consistent with the form in (A.30).

Appendix B

Asymptotic potential flow above a wavy wall

This section derives the unsteady, nonlinear potential forced by a normal velocity field which forms the basis of the asymptotic approach by Van Dyke (1951). We begin with the inviscid momentum equation

$$\frac{\partial}{\partial t}\mathbf{u} + \mathbf{u}\cdot\nabla\mathbf{u} = -\frac{1}{\rho}\nabla p. \tag{B.1}$$

Applying

$$(\mathbf{u}\cdot\nabla)\mathbf{u} = \frac{1}{2}\nabla(\mathbf{u}\cdot\mathbf{u}) - (\mathbf{u}\times\nabla\times\mathbf{u}), \tag{B.2}$$

with the assumption the flow is irrotational with $\mathbf{u} = \nabla\phi$ leads to

$$\nabla\left\{\frac{\partial\phi}{\partial t} + \frac{1}{2}\nabla\phi\cdot\nabla\phi + f(p)\right\} = 0 \tag{B.3}$$

where

$$f = \int\frac{dp}{\rho}. \tag{B.4}$$

Since the flows we are interested contain at most weak shocks, the entropy jumps are of third order with respect to pressure jumps (Whitham, 1974), an isentropic assumption leads to

$$f \equiv \int\frac{dp}{\rho} = \frac{c^2}{\gamma-1}, \tag{B.5}$$

where c is the speed of sound. With (B.5), the argument of (B.3) is equal to a function that can depend only on time,

$$\frac{\partial\phi}{\partial t} + \frac{1}{2}\nabla\phi\cdot\nabla\phi + \frac{c^2}{\gamma-1} = h(t). \tag{B.6}$$

Introducing a velocity perturbation potential φ

$$\phi = U_\infty(x+\varphi), \tag{B.7}$$

and assuming the φ-disturbances to decay sufficiently far away, $h(t)$ is

$$h = \frac{U_\infty^2}{2} + \frac{c_\infty^2}{\gamma - 1}, \tag{B.8}$$

and the speed of sound

$$c^2 = c_\infty^2 - (\gamma - 1)\left\{ \frac{\partial \phi}{\partial t} + \frac{1}{2}\left[\nabla\phi \cdot \nabla\phi - U_\infty^2 \right] \right\}. \tag{B.9}$$

The first two terms in the conservation of mass

$$\frac{1}{\rho}\frac{\partial \rho}{\partial t} + \frac{u_i}{\rho}\frac{\partial \rho}{\partial x_i} + \frac{\partial u_i}{\partial x_i} = 0. \tag{B.10}$$

are replaced using (B.3) and the isentropic speed of sound relation $c^2 d\rho = dp$

$$\frac{\partial}{\partial t}\left\{ \frac{\partial \phi}{\partial t} + \frac{1}{2}\nabla\phi \cdot \nabla\phi + f(p) \right\} = \frac{\partial^2 \phi}{\partial t^2} + \frac{1}{2}\frac{\partial}{\partial t}(\nabla\phi \cdot \nabla\phi) + \frac{c^2}{\rho}\frac{\partial \rho}{\partial t} \tag{B.11}$$

$$u_i \frac{\partial}{\partial x_i}\left\{ \frac{\partial \phi}{\partial t} + \frac{1}{2}\nabla\phi \cdot \nabla\phi + f(p) \right\} = u_i \frac{\partial^2 \phi}{\partial x_i \partial t} + \frac{u_i}{2}\frac{\partial}{\partial x_i}(\nabla\phi \cdot \nabla\phi) + u_i \frac{c^2}{\rho}\frac{\partial \rho}{\partial x_i}, \tag{B.12}$$

leaving the nonlinear potential

$$-\frac{\partial^2 \phi}{\partial t^2} - \frac{1}{2}\frac{\partial}{\partial t}(\nabla\phi \cdot \nabla\phi) - \frac{\partial \phi}{\partial x_i}\frac{\partial^2 \phi}{\partial x_i \partial t} - \frac{1}{2}\frac{\partial \phi}{\partial x_i}\frac{\partial}{\partial x_i}(\nabla\phi \cdot \nabla\phi) + c^2 \frac{\partial^2 \phi}{\partial x_i \partial x_i}. \tag{B.13}$$

With (B.7) the perturbation potential is

$$\begin{aligned}
\nabla^2 \varphi c_\infty^2 - \left(\frac{\partial}{\partial t} + U_\infty \frac{\partial}{\partial x} \right)^2 \varphi = {} & U_\infty^2 \left\{ (2\varphi_x + \varphi_x^2)\varphi_{xx} + \varphi_y^2 \varphi_{yy} + \varphi_z^2 \varphi_{zz} \right\} \\
& + 2U_\infty^2 \left\{ (1 + \varphi_x)\varphi_y \varphi_{xy} + (1 + \varphi_x)\varphi_z \varphi_{xz} + \varphi_y \varphi_z \varphi_{yz} \right\} \\
& + 2U_\infty \left\{ \varphi_x \varphi_{xt} + \varphi_y \varphi_{yt} + \varphi_z \varphi_{zt} \right\} \\
& + U_\infty \nabla^2 \varphi (\gamma - 1)\left\{ \varphi_t + U_\infty \varphi_x + \frac{1}{2} U_\infty (\varphi_x^2 + \varphi_y^2 + \varphi_z^2) \right\},
\end{aligned} \tag{B.14}$$

which is that reported in Morino (1974). The left side of (B.14) is the linear convected wave equation with an inhomogeneous right side containing the nonlinear interactions in φ. Neglecting third-order interactions,

assuming their combined affect is of higher order, the perturbation potential simplifies to

$$\begin{aligned}\nabla^2\varphi c_\infty^2 - \left(\frac{\partial}{\partial t} + U_\infty\frac{\partial}{\partial x}\right)^2\varphi = 2U_\infty^2\left\{\varphi_x\varphi_{xx}\right\} \\ + 2U_\infty^2\left\{\varphi_y\varphi_{xy} + \varphi_z\varphi_{xz}\right\} \\ + 2U_\infty\left\{\varphi_x\varphi_{xt} + \varphi_y\varphi_{yt} + \varphi_z\varphi_{zt}\right\} \\ + U_\infty\nabla^2\varphi(\gamma-1)\left\{\varphi_t + U_\infty\varphi_x\right\}.\end{aligned} \tag{B.15}$$

We consider the potential field forced by a moving surface with position

$$S(x,z,t) = y - \varepsilon g(x,z,\eta t). \tag{B.16}$$

A corresponding kinematic boundary condition is

$$\left(\frac{\partial}{\partial t} + \nabla\phi\cdot\nabla\right)S(\mathbf{x},t) = 0, \tag{B.17}$$

which provide a specific condition on the normal velocity

$$\phi_y = \varepsilon\eta g_t + \varepsilon\phi_x g_x + \varepsilon\phi_z g_z, \tag{B.18}$$

for $y = \varepsilon g$. The corresponding condition on the disturbance potential φ is

$$\varphi_y = \frac{\varepsilon\eta}{U_\infty}g_t + \varepsilon g_x(1+\varphi_x) + \varepsilon g_z\varphi_z, \tag{B.19}$$

which can be expanded $y = 0$

$$\varphi = \varphi|_{y=0} + \varphi_y|_{y=0}\varepsilon g + \frac{1}{2}\varphi_{yy}|_{y=0}(\varepsilon g)^2 + O(\varepsilon^3). \tag{B.20}$$

We assume the following asymptotic expansion of the perturbation potential

$$\varphi = \varepsilon\varphi^{(1)}(\eta t) + \varepsilon^2\varphi^{(2)}(\eta t) + \ldots, \tag{B.21}$$

in (B.20) with (B.19) leads to the no-penetration condition as

$$O(\varepsilon): \qquad \varphi_y^{(1)} = g_x \tag{B.22}$$

$$O(\varepsilon^2): \qquad \varphi_y^{(2)} = -g\varphi_{yy}^{(1)} + \frac{1}{U_\infty} g_t + g_x \varphi_x^{(1)} + g_z \varphi_z^{(1)} \tag{B.23}$$

in successive orders of ε with $\eta = O(\varepsilon)$. To order ε, the normal velocity (B.22) depends on the local slope of the wall, with a positive slope inducing a velocity that compresses the fluid above it. The evolution equation using (B.21) for φ in successive order of ε is

$$O(\varepsilon): \qquad \nabla^2 \varphi^{(1)} c_\infty^2 - U_\infty^2 \frac{\partial^2}{\partial x^2} \varphi^{(1)} = 0 \tag{B.24}$$

and

$$\begin{aligned} O(\varepsilon^2): \qquad \nabla^2 \varphi^{(2)} c_\infty^2 - U_\infty^2 \frac{\partial^2}{\partial x^2} \varphi^{(2)} & \\ = 2U_\infty \frac{\partial^2}{\partial x \partial t} \varphi^{(1)} & \\ + 2U_\infty^2 \left\{ \varphi_x^{(1)} \varphi_{xx}^{(1)} \right\} & \\ + 2U_\infty^2 \left\{ \varphi_y^{(1)} \varphi_{xy}^{(1)} + \varphi_z^{(1)} \varphi_{xz}^{(1)} \right\} & \\ + U_\infty \nabla^2 \varphi^{(1)} (\gamma - 1) \left\{ U_\infty \varphi_x^{(1)} \right\}, & \end{aligned} \tag{B.25}$$

for $\eta = O(\varepsilon)$. In the case $\eta \ll O(\varepsilon)$, the time-dependent effects in (B.25) are of higher order.

After solving for $\varphi^{(1)}$ and $\varphi^{(2)}$, the pressure can be calculated using the sound speed (B.9) and isentropic relation between c and p by

$$\left(\frac{p}{p_\infty} \right) = \left(\frac{c}{c_\infty} \right)^{\frac{2\gamma}{(\gamma-1)}} \tag{B.26}$$

The potential equations (B.24)–(B.25) with boundary conditions (B.22)-(B.23) was solved by Van Dyke (1951) for a steady ($\eta = 0$) two-dimensional ($g_z = 0$) wall. The weakly nonlinear pressure from Van Dyke (1951) along the wavy-wall boundary as

$$(p - p_\infty)_{y=0} = \left[\frac{\varepsilon g_x}{\beta} + \frac{M^2 \xi - 2}{2\beta^2} (\varepsilon g_x)^2 \right] U^2 \rho_\infty, \tag{B.27}$$

with $\beta = \sqrt{M^2 - 1}$ and $\xi = (\gamma + 1) M^2 / (2\beta^2)$. The quadratic dependence on the slope of the wall g_x in (B.27) leads to pressure-amplitude asymmetry and positive pressure skewness immediately at the wall with $Sk \propto \varepsilon (g_x)_{\mathrm{rms}}$. Of course, as with many wave asymptotic results, this approximation is not uniformly valid

for $y > \varepsilon^{-1}$. Weakly nonlinear propagation techniques of Whitham (1974) can be used to incorporate these nonlinear steepening effects with subsequent shock-fitting, though this is not necessary for our goals. We have shown that the asymmetric nonlinear compression which propagates changes slowly with distance.

Appendix C

Stability of temporally-developing free-shear flows

For moderate Reynolds numbers, the growth rates of the linear modes have been shown to approach those from inviscid theory (Ragab & Wu, 1989). Thus, we consider the inviscid stability characteristics of a temporally developing flow, and we proceed following a similar approach that has been described elsewhere (Sandham, 1989).

The primitive flow variables Reynolds decomposed are

$$[u, v, w, \rho, T] = \left[\bar{u}, \bar{v}, \bar{w}, \bar{\rho}, \bar{T}\right](y) + [u', v', w', \rho', T'], \tag{C.1}$$

where $\bar{()}$ are the average quantities that depend on the y-direction, and $(')$ are the perturbations. The mean flow quantities are

$$\left[\bar{u}, \bar{v}, \bar{w}, \bar{\rho}, \bar{T}\right](y) = [u(y), 0, 0, 1, T(u)]. \tag{C.2}$$

The mean velocity profile as set as

$$\bar{u} = \frac{\Delta U}{2} \tanh\left(\frac{y}{2\delta_m^o}\right), \tag{C.3}$$

and the temperature relation is specified from the Crocco-Busemann relation assuming unity Prandtl number (Sandham & Reynolds, 1990). The perturbations, with small-amplitude (ϵ), are in the form of travelling waves

$$[u', v', w', \rho', T'] = \epsilon \mathrm{Re}\left\{\left[\hat{u}, \hat{v}, \hat{w}, \hat{\rho}, \hat{T}\right](y) \exp\left[\mathrm{i}(\alpha x + \beta z - \omega t)\right]\right\}: \tag{C.4}$$

α and β are the streamwise and spanwise wavenumber and ω is the growth rate. Substituting the mean and perturbation quantities into the inviscid, compressible flow equations and neglecting quadratic interactions

of perturbation quantities yields a set of ordinary differential equations

$$\hat{\rho}\mathrm{i}(\alpha\bar{u}-\omega)+\hat{v}\frac{d\bar{\rho}}{dy}+\bar{\rho}\left[\mathrm{i}(\alpha\hat{u}+\beta\hat{w})+\frac{d\hat{v}}{dy}\right]=0 \tag{C.5}$$

$$\bar{\rho}\left[\mathrm{i}(\alpha\bar{u}-\omega)\hat{u}+\hat{v}\frac{d\bar{u}}{dy}\right]=\frac{-\mathrm{i}\alpha\hat{p}}{\gamma M_1^2} \tag{C.6}$$

$$\bar{\rho}\left[\mathrm{i}(\alpha\bar{u}-\omega)\hat{v}\right]=-\frac{d\hat{p}}{dy}\frac{1}{\gamma M_1^2} \tag{C.7}$$

$$\bar{\rho}\left[\mathrm{i}(\alpha\bar{u}-\omega)\hat{w}\right]=\frac{-\mathrm{i}\beta\hat{p}}{\gamma M_1^2} \tag{C.8}$$

$$\bar{\rho}\left[\mathrm{i}(\alpha\bar{u}-\omega)\hat{T}+\hat{v}\frac{d\hat{T}}{dy}\right]=-(\gamma-1)\left[\mathrm{i}(\alpha\hat{u}+\beta\hat{w})+\frac{d\hat{v}}{dy}\right] \tag{C.9}$$

The linearized equation of state

$$\hat{p}=\bar{\rho}\hat{T}+\hat{\rho}\bar{T}. \tag{C.10}$$

As done in Gropengiesser (1970) and Sandham (1989), the equations (C.5)–(C.9) with (C.10) are combined to form two equations for $\hat{v}$ and $\hat{p}$ and with

$$\hat{\chi}=\frac{\mathrm{i}\alpha\hat{p}}{\gamma M_1^2\hat{v}}, \tag{C.11}$$

yields a single nonlinear evolution equation in $\hat{\chi}$

$$\frac{d\hat{\chi}}{dy}=\frac{\alpha^2(\bar{u}-\omega/\alpha)}{\bar{T}}-\frac{\hat{\chi}(\hat{\chi}g+\frac{d\bar{u}}{dy})}{(\bar{u}-\omega/\alpha)}, \tag{C.12}$$

with

$$g=\frac{\alpha^2+\beta^2}{\bar{\rho}\alpha^2}-\frac{M_1^2(\alpha\bar{u}-\omega)^2}{\alpha^2}. \tag{C.13}$$

We use the asymptotic behavior of $\hat{v}$ and $\hat{p}$ as $y\to\infty$ in (C.12), which leads to the constant value of $\hat{\chi}$ (Sandham, 1989),

$$\hat{\chi}(y=\pm\infty)=\frac{\alpha(\bar{u}-\omega/\alpha)}{\sqrt{g\bar{T}}}. \tag{C.14}$$

The condition (C.14) provides the starting condition to integrate (C.12). For temporally developing shear layers, the real-valued spanwise and streamwise wavenumbers, (α,β), are specified along with an initial guess of the complex-valued growth rate ω. The evolution equation for $\hat{\chi}$ in equation (C.12) is integrated in y from the free-stream boundary conditions in equation (C.14) to the midplane of the shear layer at $y=0$, using a fifth-order adaptive-step-refinement Runge–Kutta scheme (Press *et al.*, 1986). Since this is an iterative approach, two solutions are marched independently from $y=-L$ and $y=L$ to $y=0$. The corresponding

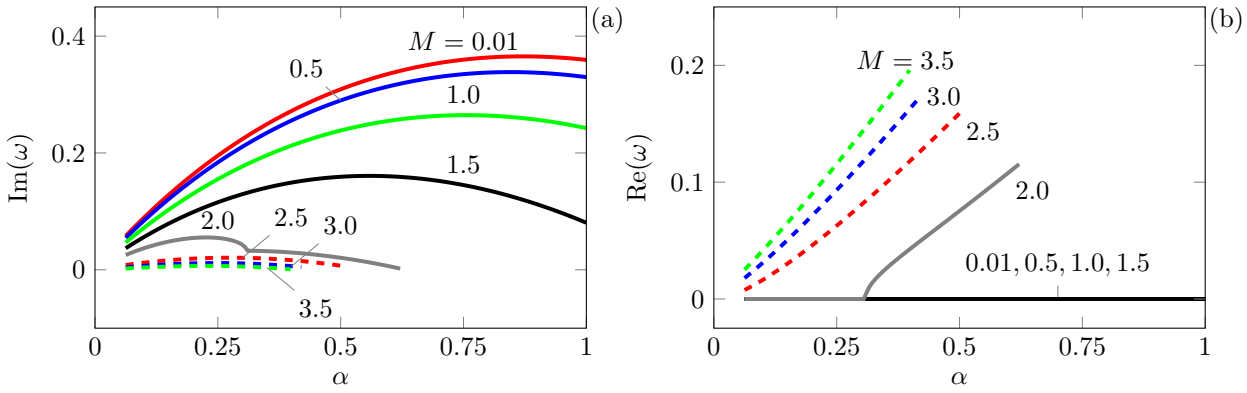

Figure C.1: Variation of two-dimensional unstable modes ($\beta = 0$) with streamwise wavenumber, α: (a) temporal amplification rate and (b) rate of phase change.

values of $\hat{\chi}_{y_+}(0)$ and $\hat{\chi}_{y_-}(0)$ are used to update the ω guess with a complex-valued Newton-Raphson method as done in Sandham (1989). Once the two values, $\hat{\chi}_{y_+}(0)$ and $\hat{\chi}_{y_-}(0)$, match to within a specified tolerance, $\epsilon \leq 10^{-14}$, the root-finding procedure is stopped.

Figure C.1 (a) shows the growth rate for two-dimensional, spanwise oriented modes $(\alpha, 0)$. As the Mach number increases, the growth rate decreases. As shown in figure C.1 (b), for $M_1 \gtrsim 2$, the unstable modes convect with finite phase speed $\alpha Re(\omega) > 0$. These two-dimensional modes are known as the supersonic modes (Sandham, 1989). They advect supersonically with respect to either the upper or lower free-stream velocities depending on their direction to the right or left. These supersonic modes radiate Mach waves away from the shear layer as shown by the oscillatory behavior of the eigenfunction solutions in (b) and (c) in figure C.3–C.6.

For $M \gtrsim 1.5$, the most unstable modes are three-dimensional ($\beta \neq 0$) as shown in figure C.2. Increasing the Mach number has a dampening effect on the growth rate of the three-dimensional modes.

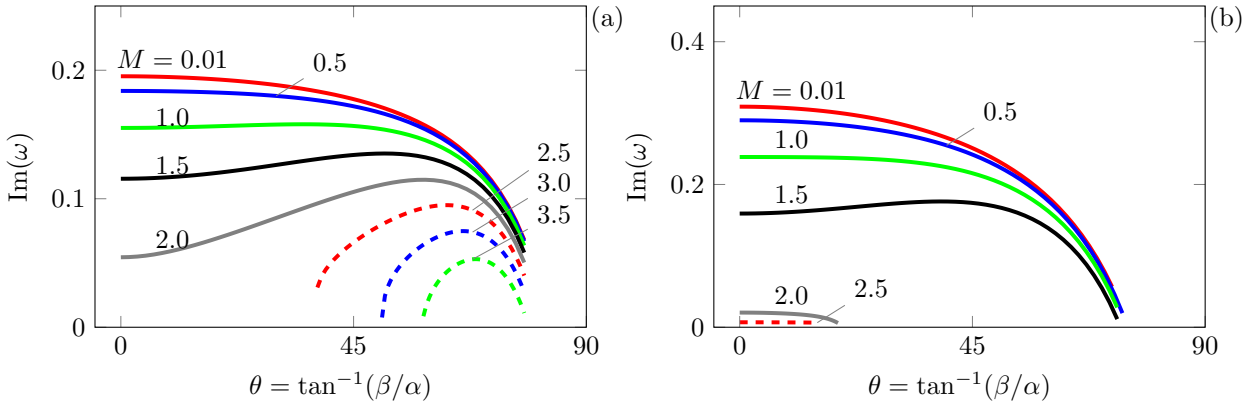

Figure C.2: Variation of three-dimensional growth rates with angle between the streamwise and spanwise wavenumbers: (a) $\alpha = 0.25$ and (b) 0.5.

For $M = 2.5$ eigenfunctions of the unstable stationary, slow- and fast-supersonic modes are shown in figure C.3–C.6 (a), (b) and (c), respectively. The trend of the eigenfunctions agree with those reported in Sandham (1989).

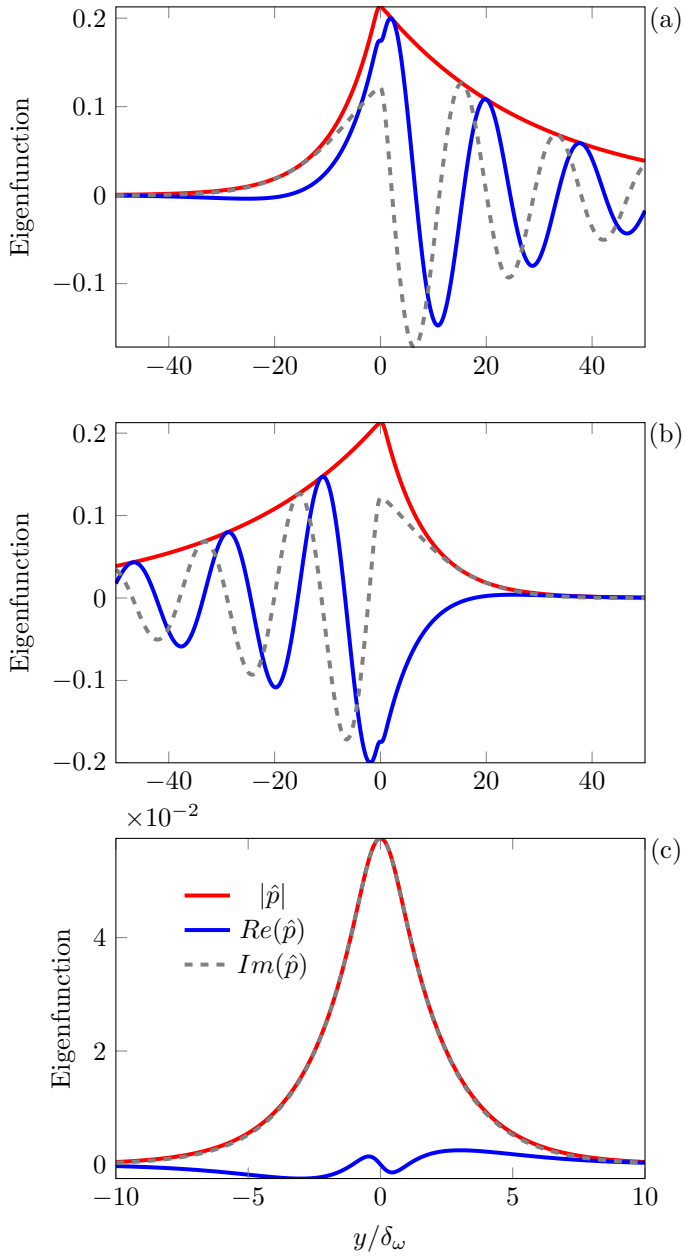

Figure C.3: Pressure eigenfunction for $M = 2.5$ for (a)-(b) the supersonic radiating modes and (c) the most-unstable three-dimensional mode (c).

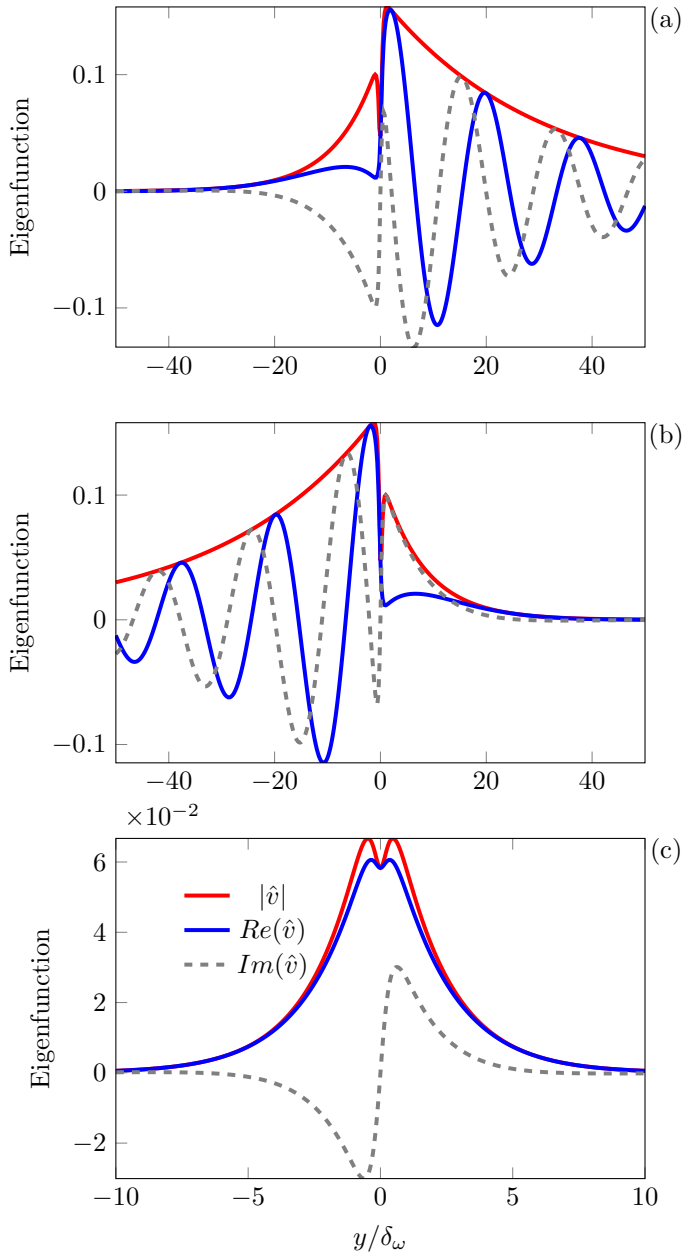

Figure C.4: v-velocity eigenfunction for $M = 2.5$ for $M = 2.5$ for (a)-(b) the supersonic radiating modes and (c) the most-unstable three-dimensional mode (c).

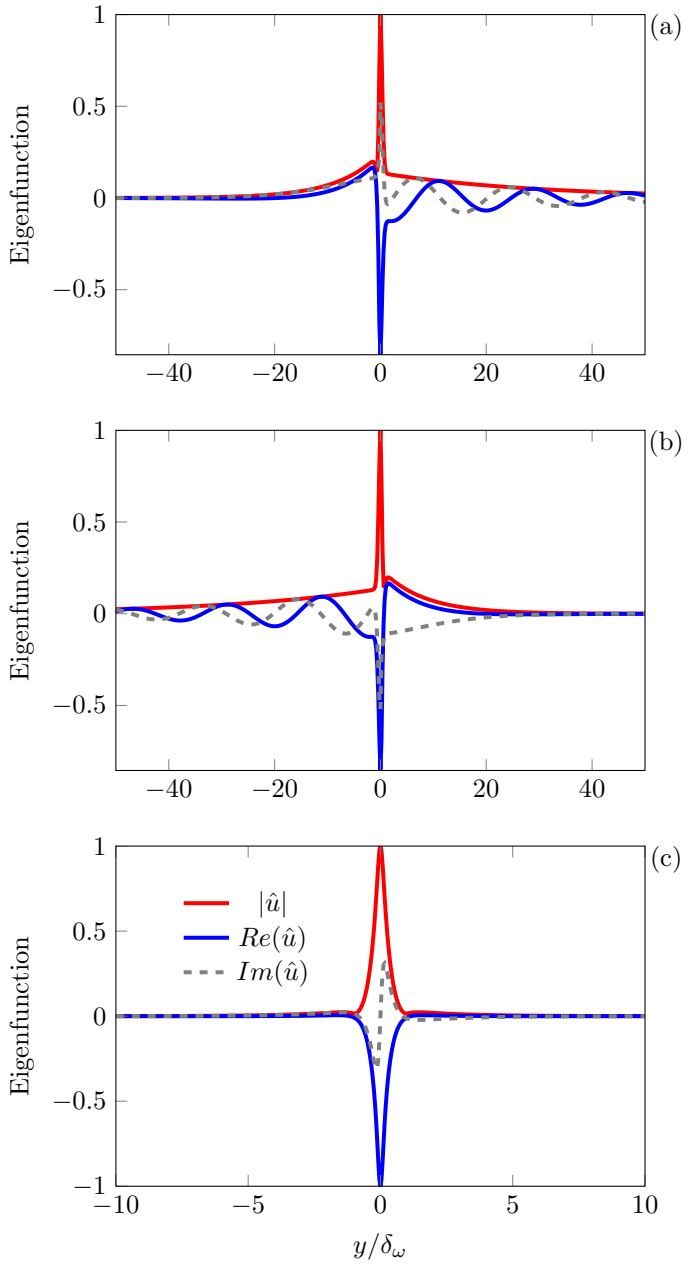

Figure C.5: u-velocity eigenfunction for $M = 2.5$ for (a)-(b) the supersonic radiating modes and (c) the most-unstable three-dimensional mode (c).

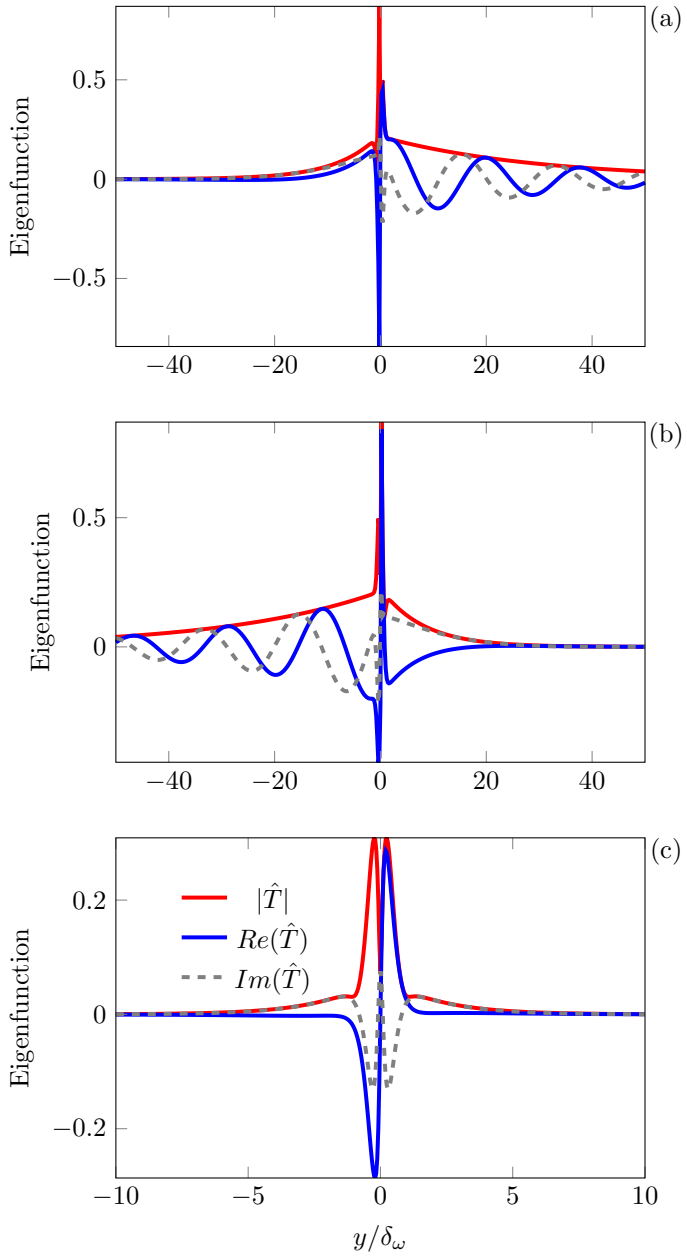

Figure C.6: Temperature eigenfunction for $M = 2.5$ for (a)-(b) the supersonic radiating modes and (c) the most-unstable three-dimensional mode (c).

References

Anderson, A.T. & Freund, J.B. 2012 Source mechanisms of jet crackle. In *18th AIAA/CEAS Aeroacoustics Conference*.

Avital, E.J., Musafir, R.E. & Korakianitis, T. 2013 Nonlinear propagation of sound emitted by high speed wave packets. *Journal of Computational Acoustics* **21** (2).

Avital, E.J. & Sandham, N.D. 1997 A note on the structure of the acoustic field emitted by a wave packet. *Journal of Sound and Vibration* **204** (3), 533 – 539.

Baars, W. J. & Tinney, C. E. 2014 Shock-structures in the acoustic field of a Mach 3 jet with crackle. *Journal of Sound and Vibration* **333** (12), 2539 – 2553.

Baars, W. J., Tinney, C. E., Wochner, M. S. & Hamilton, M. F. 2014 On cumulative nonlinear acoustic waveform distortions from high-speed jets. *Journal of Fluid Mechanics* **749**, 331–366.

Bewley, T.R., Moin, P. & Temam, R. 2001 DNS-based predictive control of turbulence: An optimal benchmark for feedback algorithms. *Journal of Fluid Mechanics* **447**, 179–225.

Bodony, Daniel J. 2010 Accuracy of the simultaneous-approximation-term boundary condition for time-dependent problems. *Journal of Scientific Computing* **43** (1), 118–133.

Bogey, C. & Bailly, C. 2004 A family of low dispersive and low dissipative explicit schemes for flow and noise computations. *Journal of Computational Physics* **194** (1), 194–214.

Buchta, D. A., Anderson, A. T. & Freund, J. B. 2014 Near-field shocks radiated by high-speed free-shear-flow turbulence. In *20th AIAA/CEAS Aeroacoustics Conference*.

Chobotov, V. & Powell, A. 1957 On the prediction of acoustic environments from rockets. *Technical Report* E.M.-7-7. Ramo-Wooldridge Corporation.

Clemens, N. T. & Mungal, M. G. 1992 Two- and three-dimensional effects in the supersonic mixing layer. *AIAA Journal* **30** (4), 973–981.

Crighton, D. G. 1975 Basic principles of aerodynamic noise generation. *Progress in Aerospace Sciences* **16** (1), 31–96.

Crighton, D. G. 1986 Nonlinear acoustic propagation of broadband noise. In *Recent Advances in Aeroacoustics* (ed. Anjaneyulu Krothapalli & Charles A. Smith), pp. 411–454. Springer New York.

Crighton, D. G. & Huerre, P. 1990 Shear-layer pressure fluctuations and superdirective acoustic sources. *Journal of Fluid Mechanics* **220**, 355–368.

Darke, R. & Freund, J. B. 2001 Mach wave radiation from a jet at Mach 1.92. *Physics of Fluids* **13** (9), S3.

De Cacqueray, N. & Bogey, C. 2014 Noise of an overexpanded Mach 3.3 jet: Non-linear propagation effects and correlations with flow. *International Journal of Aeroacoustics* **13** (7), 607 – 632.

Debisschop, J. R., Chambres, O. & Bonnet, J. P. 1994 Velocity field characteristics in supersonic mixing layers. *Experimental Thermal and Fluid Science* **9** (2), 147–155.

Dosanjh, D. S. & Yu, J. C. 1968 Noise from underexpanded axisymmetric jet flows using radial jet flow impingement. In *Proceedings of AFOSR-UTIAS Symposium on Aerodynamic Noise*, pp. 169–188. Toronto.

Duan, Lian, Choudhari, Meelan M. & Wu, Minwei 2014 Numerical study of acoustic radiation due to a supersonic turbulent boundary layer. *Journal of Fluid Mechanics* **746**, 165–192.

Eggers, J. M. 1966 *Velocity profiles and eddy viscosity distributions downstream of a Mach 2.22 nozzle exhausting to quiescent air*. National Aeronautics and Space Administration.

Elliott, G. S. & Samimy, M. 1990 Compressibility effects in free shear layers. *Physics of Fluids A: Fluid Dynamics (1989-1993)* **2** (7), 1231–1240.

Ffowcs Williams, J. E. 1963 The noise from turbulence convected at high speed. *Philosophical Transactions of the Royal Society of London* **255**, 469–503.

Ffowcs Williams, J. E. & Maidanik, G. 1965 The Mach wave field radiated by supersonic turbulent shear flows. *Journal of Fluid Mechanics* **21**, 641–657.

Ffowcs Williams, J. E., Simson, J. & Virchis, V. J. 1975 'Crackle': An annoying component of jet noise. *Journal of Fluid Mechanics* **71**, 251–271.

Fiévet, Romain, Tinney, Charles E., Baars, Woutijn J. & Hamilton, Mark F. 2015 Coalescence in the sound field of a laboratory-scale supersonic jet. *AIAA Journal* pp. 1–12.

Fourguette, D. C., Mungal, M. G. & Dibble, R. W. 1991 Time evolution of the shear layer of a supersonic axisymmetric jet. *AIAA Journal* **29** (7), 1123–1130.

Foysi, H. & Sarkar, S. 2010 The compressible mixing layer: an LES study. *Theoretical and Computational Fluid Dynamics* **24** (6), 565–588.

Freund, J.B. 2011 Adjoint-based optimization for understanding and suppressing jet noise. *Journal of Sound and Vibration* **330** (17), 4114–4122.

Freund, J. B. 1997*a* Compressibility effects in a turbulent annular mixing layer. PhD thesis, Stanford University.

Freund, J. B. 1997*b* Proposed inflow/outflow boundary condition for direct computation of aerodynamic sound. *AIAA Journal* **35** (4), 740–742.

Freund, J. B., Lele, S. K. & Moin, P. 2000*a* Compressibility effects in a turbulent annular mixing layer. Part 1. turbulence and growth rate. *Journal of Fluid Mechanics* **421**, 229–267.

Freund, J. B., Lele, S. K. & Moin, P. 2000*b* Numerical simulation of a Mach 1.92 turbulent jet and its sound field. *AIAA Journal* **38** (11), 2023–2031.

Gee, K. L., Neilsen, T. B. & Atchley, A. A. 2013*a* Skewness and shock formation in laboratory-scale supersonic jet data. *Journal of the Acoustical Society of America* **133** (6), 491–497.

Gee, K. L., Neilsen, T. B., Downing, J. M., James, M. M., McKinley, R. L., McKinley, R. C. & Wall, A. T. 2013*b* Near-field shock formation in noise propagation from a high-power jet aircraft. *Journal of the Acoustical Society of America* **133** (2), 88–93.

Gee, K. L., Neilsen, T. B., Wall, A. T., Downing, J. M., James, M. M. & McKinley, R. L. 2016 Propagation of crackle-containing jet noise from high-performance engines. *Noise Control Engineering Journal* **64** (1), 1–12.

Gee, K. L., Sparrow, V. W., Atchley, A. & Gabrielson, T. B. 2007 On the perception of crackle in high-amplitude jet noise. *AIAA Journal* **45** (3), 593–598.

Goebel, S. G. & Dutton, J. C. 1991 Experimental study of compressible turbulent mixing layers. *AIAA journal* **29** (4), 538–546.

Greska, Brenton J. 2005 Supersonic jet noise and its reduction supersonic jet noise and its reduction using microjet injection. PhD thesis, Florida State University.

Gropengiesser, H. 1970 Study on the stability of boundary layers and compressible fluids. *Technical Report*. NASA TT F-12, 786.

Heeb, N., Mora, P., Gutmark, E. & Kailasanath, K. 2013 Investigation of the noise from a rectangular supersonic jet. *19th AIAA/CEAS Aeroacoustics Conference* p. 226.

Howe, M. S. 1981 The role of displacement thickness fluctuations in hydroacoustics, and the jet-drive mechanism of the flue organ pipe. *Proceedings of the Royal Society of London A: Mathematical, Physical and Engineering Sciences* **374** (1759), 543–568.

Jackson, T. L. & Grosch, C. E. 1989 Inviscid spatial stability of a compressible mixing layer. *Journal of Fluid Mechanics* **208**, 609–637.

Jameson, A., Martinelli, L. & Pierce, N.A. 1998 Optimum aerodynamic design using the Navier–Stokes equations. *Theoretical and Computational Fluid Dynamics* **10** (1), 213–237.

Jimenez, Javier & Pinelli, Alfredo 1999 The autonomous cycle of near-wall turbulence. *Journal of Fluid Mechanics* **389**, 335–359.

Jordan, Peter & Colonius, Tim 2013 Wave packets and turbulent jet noise. *Annual Review of Fluid Mechanics* **45** (1), 173–195.

Kim, Jeonglae, Bodony, Daniel J. & Freund, Jonathan B. 2014 Adjoint-based control of loud events in a turbulent jet. *Journal of Fluid Mechanics* **741**, 28–59.

Kleinman, R. & Freund, J. B. 2008 The sound from mixing layers simulated with different ranges of turbulence scales. *Physics of Fluids* **20** (10).

Krothapalli, A., Arakeri, V. & Greska, B. 2003*a* Mach wave radiation: A review and an extension. In *41st Aerospace Sciences Meeting and Exhibit*.

Krothapalli, A., Greska, B. & Arakeri, V. 2002 High speed jet noise reduction using microjets.

Krothapalli, A., Greska, B. & Arakeri, V. 2005 High-speed jet noise reduction using microjets. *Combustion Processes in Propulsion* pp. 231–244.

Krothapalli, A., Venkatakrishnan, L. & Lourenco, L. 2000 Crackle: A dominant component of supersonic jet mixing noise. In *6th AIAA/CEAS Aeroacoustics Conference*.

Krothapalli, A., Venkatakrishnan, L., Lourenco, L., Greska, B. & Elavarasan, R. 2003*b* Turbulence and noise suppression of a high-speed jet by water injection. *Journal of Fluid Mechanics* (491), 131–159.

Laufer, J. 1961 Aerodynamic noise in supersonic wind tunnels. *Journal of the Aerospace Sciences* **28** (9), 685–692.

Laufer, J., Ffowcs Williams, J. E. & Childress, S. 1964 Mechanism of noise generation in the turbulent boundary layer. In *AGARD Conference Proceedings*.

Laufer, J., Schlinker, R. & Kaplan, R. E. 1976 Experiments on supersonic jet noise. *AIAA Journal* **14** (4), 489–497.

Lele, S. K. 1992 Compact finite difference schemes with spectral-like resolution. *Journal of Computational Physics* **103** (1), 16–42.

Lessen, M., Fox, J. A. & Zien, H. M. 1965 On the inviscid stability of the laminar mixing of two parallel streams of a compressible fluid. *Journal of Fluid Mechanics* **23**, 355–367.

Liepmann, H. W. 1954 On the acoustic radiation from boundary layers and jets. *Technical Report*. Guggenheim Aeronautical Laboratory, California Institute of Technology.

Lighthill, M. J. 1952 On sound generated aerodynamically. I General theory. *Proceedings of the Royal Society of London. Series A. Mathematical and Physical Sciences* **211** (1107), 564–587.

Lighthill, M. J. 1956 Viscosity effects in sound waves of finite amplitude. In *Surveys in Mechanics* (ed. G. K. Batchelor & R. M. Davies), pp. 250–351. Cambridge University Press.

Lighthill, M. J. 1993 Some aspects of the aeroacoustics of extreme-speed jets. In *Symposium on Aerodynamics & Aeroacoustics* (ed. K. Y. Fung), pp. 39–48.

Lowson, M.V. & Ollerhead, J.B. 1968 Visualization of noise from cold supersonic jets. *Journal of the Acoustical Society of America* **44** (2), 624–630.

Martens, S., Spyropoulos, J.T. & Nagel, Z. 2011 The effect of chevrons on crackle-engine and scale model results. *Proceedings of the ASME Turbo Expo* **1**, 315–326.

McInerny, S. A. 1996 Launch vehicle acoustics. Part II: Statistics of the time domain data. *Journal of Aircraft* **33** (3), 518–523.

Mollo–Christensen, E. 1967 Jet noise and shear flow instability seen from an experimenter's viewpoint. *Journal of Applied Mechanics* **34** (1), 1–7.

Mora, P., Heeb, N., Kastner, J., Gutmark, E.J. & Kailasanath, K. 2013*a* Near-and far-field pressure skewness and kurtosis in heated supersonic jets from round and chevron nozzles. *Proceedings of the ASME Turbo Expo* **2**.

Mora, P., Heeb, N., Kastner, J., Gutmark, E. J. & Kailasanath, K. 2013*b* Effect of scale on the far-field pressure skewness and kurtosis of heated supersonic jets. In *51st AIAA Aerospace Sciences Meeting including the New Horizons Forum and Aerospace Exposition 2013*.

Mora, P., Kastner, J., Gutmark, E.J. & Kailasanath, K. 2015 Investigation of a heated supersonic jet chevrons nozzle. In *53rd AIAA Aerospace Sciences Meeting*.

Mora, P., Kastner, J., Heeb, N., Munday, D., Gutmark, E.J., Liu, J. & Kailasanath, K. 2012 The impact of heat on the near and far-field pressure skewness in supersonic jets. In *50th AIAA Aerospace Sciences Meeting Including the New Horizons Forum and Aerospace Exposition*.

Morino, L. 1974 A general theory of unsteady compressible potential aerodynamics. *Technical Report*. NASA.

Murray, N. E. & Lyons, G. W. 2016 On the convection velocity of source events related to supersonic jet crackle. *Journal of Fluid Mechanics* **793**, 477–503.

Nichols, J. W., Lele, S. K. & Spyropoulos, J. T. 2013 The source of crackle noise in heated supersonic jets. In *19th AIAA/CEAS Aeroacoustics Conference*.

Oertel, H. 1979 Kinematics of Mach waves inside and outside supersonic jets. In *Recent Developments in Theoretical and Experimental Fluid Mechanics* (ed. U. Müller, K.G. Roesner & B. Schmidt), pp. 121–136. Springer Berlin Heidelberg.

Pantano, C. & Sarkar, S. 2002 A study of compressibility effects in the high-speed turbulent shear layer using direct simulation. *Journal of Fluid Mechanics* **451**, 329–371.

Papamoschou, D. 2000 Linear model of mach wave suppression in a dual-stream jet.

Papamoschou, D. & Debiasi, M. 2001 Directional suppression of noise from a high-speed jet. *AIAA Journal* **39** (3), 380–387.

Papamoschou, D., Johnson, A. D. & Phong, V. 2014 Aeroacoustics of three-stream high-speed jets from coaxial and asymmetric nozzles. *Journal of Propulsion and Power* **30** (4), 1055–1069.

Papamoschou, D., Phong, V., Xiong, J. & Liu, F. 2016 Quiet nozzle concepts for three-stream jets. In *54th AIAA Aerospace Sciences Meeting*.

Papamoschou, D. & Roshko, A. 1988 Compressible turbulent shear layer: An experimental study. *Journal of Fluid Mechanics* **197**, 453–477.

Pestorius, F. M. & Blackstock, D. T. 1974 Propagation of finite amplitude noise. In *Proceedings of Copenhagen Symposium on Finite Amplitude Effects in Fluids*.

Petitjean, B. P. & McLaughlin, D. K. 2003 Experiments on the nonlinear propagation of noise from supersonic jets. In *9th AIAA/CEAS Aeroacoustics Conference*.

Petitjean, B. P., Viswanathan, K. & McLaughlin, D. K. 2005 Acoustic pressure waveforms measured in high speed jet noise experiencing nonlinear propagation. *43rd AIAA Aerospace Sciences Meeting and Exhibit* pp. 1371–1382.

Phillips, O. M. 1960 On the generation of sound by supersonic turbulent shear layers. *Journal of Fluid Mechanics* **9**, 1–28.

Press, W. H., Flannery, B. P., Teukolsky, S. A. & Vetterling, W. T. 1986 *Numerical Recipes*. Cambridge: Cambridge University Press.

Ragab, S. A. & Wu, J. L. 1989 Linear instabilities in two-dimensional compressible mixing layers. *Physics of Fluids* **1** (6), 957–966.

Rossmann, T., Mungal, M.G. & Hanson, R.K. 2002 Evolution and growth of large-scale structures in high compressibility mixing layers. *Journal of Turbulence* **3**.

Salant, R. F., Zaic, G. F. & Kolesar, R. R. 1971 Holographic study of the Mach wave field generated by a supersonic turbulent jet. In *Proceedings of the Purdue Noise Control Conference* (ed. Malcolm J. Crocker), pp. 490–495.

Samanta, A. 2016 On the axisymmetric stability of heated supersonic round jets. *Proceedings of the Royal Society of London A: Mathematical, Physical and Engineering Sciences* **472** (2188).

Sandham, N. D. 1989 A numerical investigation of the compressible mixing layer. PhD thesis, Stanford University.

Sandham, N. D. & Reynolds, W. C. 1990 Compressible mixing layer–linear theory and direct simulation. *AIAA Journal* **28** (4), 618–624.

Sandham, N. D. & Reynolds, W. C. 1991 Three-dimensional simulations of large eddies in the compressible mixing layer. *Journal of Fluid Mechanics* **224**, 133–158.

Seiner, J. M., Ponton, M. K., Jansen, B. J. & Lagen., N. T. 1992 The effects of temperature on supersonic jet noise emission. DGLR/AIAA Paper 92-02-046.

Szewczyk, V. M. 1978 The role of flow acoustic interaction in jet noise studies. PhD thesis, University of Southampton.

Tam, C. K. W. & Burton, D. E. 1984*a* Sound generated by instability waves of supersonic flows. Part I. Two-dimensional mixing layers. *Journal of Fluid Mechanics* **138**, 249–271.

Tam, C. K. W. & Burton, D. E. 1984*b* Sound generated by instability waves of supersonic flows. Part II Axisymmetric jets. *Journal of Fluid Mechanics* **138**, 273–295.

Tam, C. K. W. & Hu, F. Q. 1989 On the three families of instability waves of high-speed jets. *Journal of Fluid Mechanics* **201**, 447–483.

Tam, C. K. W. & Webb, J. C. 1993 Dispersion-relation-preserving finite difference schemes for computational acoustics. *Journal of Computational Physics* **107** (2), 262–281.

Tanna, H. K., Dean, P. D. & Burrin, R. H. 1976 Turbulent mixing noise data. *Technical Report* AFAPL-TR-76-65. The Generation and Radiation of Supersonic Jet Noise, U.S. Air Force Aero Propulsion Laboratory Technical Report Laboratory.

Taylor, G. I. 1910 The conditions necessary for discontinuous motion in gases. *Proceedings of the Royal Society of London A: Mathematical, Physical and Engineering Sciences* **84** (571), 371–377.

Thompson, K. W. 1987 Time dependent boundary conditions for hyperbolic systems. *Journal of Computational Physics* **68** (1), 1–24.

Thompson, Phillip A. 1988 *Compressible-Fluid Dynamics*. McGraw-Hill Inc.

Troutt, T. R. & Mclaughlin, D. K. 1982 Experiments on the flow and acoustic properties of a moderate-Reynolds-number supersonic jet. *Journal of Fluid Mechanics* **116**, 123–156.

Van Dyke, M. D. 1951 Study of second-order supersonic-flow theory. *Technical Report*. National Advisory Committee for Aeronautics.

Vishnampet, R. 2015 An exact and consistent adjoint method for high-fidelity discretization of the compressible flow equations. PhD thesis, University of Illinois at Urbana–Champaign.

Vreman, A. W., Sandham, N. D. & Luo, K. H. 1996 Compressible mixing layer growth rate and turbulence characteristics. *Journal of Fluid Mechanics* **320**, 235–258.

Wei, M. & Freund, J.B. 2006 A noise-controlled free shear flow. *Journal of Fluid Mechanics* **546**, 123–152.

Westley, R. & Woolley, J. H. 1968 An investigation of the near noise fields of a choked axi-symmetric air jet. In *Proceedings of the AFOSR-UTIAS Symposium on Aerodynamic Noise*, pp. 147–167. Toronto.

Whitham, G. B. 1974 *Linear and Nonlinear Waves*. New York: John Wiley & Sons, Inc.

Wu, X. 2005 Mach wave radiation of nonlinearly evolving supersonic instability modes in shear layers. *Journal of Fluid Mechanics* **523**, 121–159.